

Full-scale Assessment of Impact of Unfavourable Upstream Conditions on the Performance and Loads of Wind Turbines

A thesis submitted to attain the degree of
DOCTOR OF SCIENCES of ETH ZURICH
(Dr. sc. ETH Zurich)

presented by
Mohsen Zendeabad
M.Sc. Mech. Eng., Sharif Univ. of Tech.
Born 01.05.1987 in Shiraz
Citizen of Iran

Accepted on the recommendation of
Prof. Dr. Reza S. Abhari, examiner
Dr. Ndaona Chokani, co-examiner
Prof. Dr. Thomas Rösigen, co-examiner

2017

*To my parents,
Ebrahim (1952-2015) and Manijeh...*

Abstract

Current fast growth of electricity production from wind, accelerated by the environmental effects of fossil fuels and recent nuclear incidences, results in three major consequences for wind industry: wind energy is produced in the scale of wind farms, rather than single wind turbines; due to scarcity of eligible land, environments of less friendly conditions, such as forested areas are considered for installing wind turbines; and wind turbines of larger size are designed for efficient cost-effective exploitation of available resources. Studies show that unfavorable upstream conditions such as wake from upstream turbines, complex terrain topology and forested fetch can cause detrimental effects on the power generation of a wind turbine. In addition to power generation, unfavorable upstream conditions can result in higher structural loads, which are of higher significance for large-sized wind turbines.

In this study a full-scale experimental database is developed to quantify the impact of upstream conditions on the wake extent, power generation and structural loads of a wind turbine. In this regard, windRoverII, a mobile laboratory equipped with a 3D scanning LiDAR system is developed. WindRoverII also features a portable stand-alone opto-mechanical platform to measure structural deflections of full-scale wind turbines with no necessary modifications on the structure of the turbine.

Using the mobile-based LiDAR successive measurements of the line-of-sight wind speed from multiple positions are made; from these measurements, the time-averaged three-dimensional and two-dimensional wind velocity vectors are reconstructed. The approach of this novel measurement technique is first validated by comparisons to a meteorological mast and SODAR at a meteorological observatory. Subsequently, volumetric measurements of three-dimensional wind velocity in the wake of a single wind turbine and planar measurements of two-dimensional wind velocity in the scale of wind farms are used to characterize the wake flows in two wind farms with $26MW$ and $28MW$ capacities. Measurements show different velocity recovery rates in the near-wake (range of $1D - 3D$ downstream positions) and far-wake (range of $3D - 7D$ downstream positions) of a turbine. As compared to far-wake, the near-wake region is associated with a faster recovery rate

where up to 70% of velocity recovery occurs. When the wake region is laterally exposed to the wake from upstream turbines, the velocity recovery occurs with up to 40% slower rate and the fast recovery in the near-wake is not any more observed.

In a wind farm whose turbines have either a forested or unforested fetch, measurements of the wind speed, wind direction and turbulence intensity are made with the LiDAR, and measurements of the tower head aeroelastic deflections are simultaneously made with the opto-mechanical measurement system. Measurements show that turbulence intensity in the forested fetch is up to 15% higher compared to unforested fetch. Aeroelastic deflections of the tower during normal operation are up to 2.8 times larger for a turbine in forested fetch compared to a turbine in an unforested fetch. It is observed that the turbine with forested fetch has 17% lower annual energy yield compared to a turbine in an unforested fetch. Furthermore, an analysis of the maintenance logs of the turbines shows that a turbine in forested fetch has up to 2.2 times more fault durations per year compared to the similar turbine in unforested fetch.

Simultaneous measurements of the tower deflection and the yaw misalignment of rotor show that tower deflections during normal operation are sensitive to the yaw misalignment of the rotor, and the tower deflections with negative yaw misalignment are seen to be larger than with positive yaw misalignment. The tower deflections during power cut-off and normal operation are, respectively, modeled with free and forced vibration single-degree-of-freedom models to calculate the damping ratio. The damping ratio during power cut-off, 6.8%, is in the lower range of damping ratios that are measured during normal operation, 5.5%-13.2%. During transition to power cut-off, oscillational deflection of tower head is observed. The amplitude of the oscillational deflections decreases to one third in the first oscillation. Power generation and the attendant torque on the tower head accounts for this rapid decrease during the first oscillation.

The findings of this thesis suggest that although installation of wind turbines in packed wind farms and in unfavourable environments is inevitable, the attendant impact on the power generation and structural loads of each turbine needs to be considered in the initial design and output estimation of planned wind farms.

Zusammenfassung

Das derzeitige rapide Wachstum der Stromerzeugung aus Wind, das durch die negativen Umweltauswirkungen fossiler Energieträger und durch die jüngsten nuklearen Unfälle noch beschleunigt wird, hat drei wesentliche Konsequenzen für die Windindustrie: Windenergie wird durch Windparks und nicht durch einzelne Windkraftanlagen erzeugt; Wegen Knappheit an förderfähigen Flächen werden Gebiete von weniger förderlichen Bedingungen, wie beispielsweise bewaldete Gebiete, für die Installation von Windenergieanlagen berücksichtigt; Sowie sind große Windturbinen größeren Umfangs für eine effiziente und kostengünstige Nutzung der verfügbaren Ressourcen ausgelegt. Untersuchungen zeigen, dass ungünstige Anströmbedingungen, wie die sich ergebenden Wirbelströmungen, komplexe Geländetopologie und bewaldeter Windweg, nachteilige Auswirkungen auf die Stromerzeugung einer Windenergieanlage haben können. Neben der Stromerzeugung können solche ungünstig Anströmbedingungen zu höheren statischen Belastungen führen, die vor allem für große Windkraftanlagen von größerer Bedeutung sind.

In dieser Studie wird eine umfangreiche experimentelle Datenbank entwickelt, um die Auswirkungen verschiedener stromaufwärtigen Bedingungen auf die Wirbelströmungen, die Stromerzeugung und auf die statische Belastung einer Windkraftanlage zu quantifizieren. In dieser Hinsicht wird WindRoverII, ein mobiles Labor, welches mit einem 3D-Scanning-LiDAR-System ausgestattet ist, entwickelt. WindRoverII verfügt zudem über eine tragbare Stand-Alone-Opto-Mechanik zur Messung struktureller Verbiegung von Windkraftanlagen ohne notwendige Änderungen an der Turbine.

Mit dem mobilen LiDAR werden sukzessive Messungen der LOS Windgeschwindigkeit aus mehreren Positionen vorgenommen; Aus diesen Messungen werden die zeitlich gemittelten dreidimensionalen und zweidimensionalen Windgeschwindigkeitsvektoren rekonstruiert. Der Ansatz dieser neuartigen Messtechnik wird zunächst durch Vergleiche mit einem meteorologischen Mast und SODAR an einem meteorologischen Observatorium validiert. Anschließend werden volumetrische Messungen der dreidimensionalen Windgeschwindigkeit in der Wirbelzone einer einzigen Windturbine und planare Messungen der zweidimen-

sionalen Windgeschwindigkeit in der Größenordnung von Windparks verwendet, um die Strömungen in der Wirbelzone in zwei Windparks mit 26MW und 28MW zu charakterisieren MW-Kapazitäten. Die Messungen zeigen verschiedene Geschwindigkeitsrückgewinnungsraten im Nahbereich (Bereich von $1D - 3D$ Downstream-Positionen) und in der weiter entfernten Wirbelzone (Bereich von $3D - 7D$ Downstream-Positionen) einer Turbine. Im Vergleich zur distanzierten Wirbelzone ist im Nahbereich eine schnellere Geschwindigkeitserholung mit bis zu 70% messbar. Wenn die Wirbelzone einer Turbine seitwärts einer Wirbelschlepe von stromaufwärtigen Turbinen ausgesetzt ist, ist die Geschwindigkeitserholung mit bis zu 40% langsamer und eine schnelle Erholung im Nahbereich kann nicht mehr beobachtet werden.

In einem Windpark, dessen Turbinen sich entweder durch einen bewaldeten oder unbewaldeten Windweg auszeichnen, werden mit dem LiDAR Messungen der Windgeschwindigkeit, Windrichtung und Turbulenzintensität vorgenommen und gleichzeitig Messungen der aeroelastischen Auslenkungen des Turmes mit dem optomechanischen Messsystem vorgenommen. Messungen zeigen, dass die Turbulenzintensität im bewaldeten Windweg bis zu 15% höher ist als bei dem unbewaldeten Windweg. Aeroelastische Auslenkungen des Turms im Normalbetrieb sind bis zu 2,8 mal größer für eine Turbine bei bewaldetem Windweg im Vergleich zu einer Turbine im unbewaldeten Windweg. Es wird beobachtet, dass die Turbine mit bewaldetem Windweg 17% niedrigeren jährlichen Energieertrag im Vergleich zu einer Turbine mit unbewaldetem Windweg hat. Darüber hinaus zeigt eine Analyse der Instandhaltungsprotokolle der Turbinen, dass eine Turbine mit bewaldetem Windweg bis zu 2,2 mal mehr Fehlerdauern pro Jahr im Vergleich zu der ähnlichen Turbine mit unbewaldetem Windweg hat.

Gleichzeitige Messungen der Turmauslenkung und der Gierwinkelfehlausrichtung des Rotors zeigen, dass Turmauslenkungen während des Normalbetriebes gegenüber der Gierwinkelfehlausrichtung des Rotors empfindlich sind und dass die Turmauslenkungen mit negativer Gierwinkelfehlausrichtung größer sind als mit positiver Gierwinkelfehlausrichtung. Um das Dämpfungsverhältnis zu berechnen, werden die Turmauslenkungen bei Leistungsabschaltung und Normalbetrieb mit SDOF Vibrationsmodellen mit einem Freiheitsgrad simuliert. Das Dämpfungsverhältnis bei Leistungsabschaltung von 6,8% liegt im unteren Bereich der im Normalbetrieb gemessenen Dämpfungsverhältnisse von 5,5% – 13,2%. Während des Übergangs zur Leistungsabschaltung wird eine oszillierende Auslenkung des Turmkopfes beobachtet. Die Amplitude der Schwingungsablenkungen nimmt bei der ersten Schwingungsperiode auf ein Drittel ab. Die Stromerzeugung und das damit verbundene Drehmoment am Turm sind dabei für die schnelle Abnahme während der ersten Oszillation verantwortlich.

Die Ergebnisse dieser Arbeit deuten darauf hin, dass wenn auch eine Installation von Windkraftanlagen in dicht bebauten Windparks und ungünstigen Gebieten unvermeidlich ist, bereits beim Design und bei der Einschätzung der Produktionsleistung die negativen

resultierenden Einflüsse auf die Stromerzeugung sowie auf die Strukturbelastung jeder Turbine berücksichtigt werden sollten.

Acknowledgments

I would like to acknowledge the help of my advisors, colleagues, friends and family who made the achievements of this thesis possible.

In particular, I would like to sincerely thank my supervisor, Professor Dr. Reza S. Abhari for giving me the chance to work on this challenging project in the unique professional environment of Laboratory for Energy Conversion (LEC), for his close and to-the-point support during the past five years and for pushing me to achieve the best results from the existing potentials.

My special thanks go to Dr. Ndaona Chokani for his valuable comments, for his passionate support of my work, for being readily available round the clock and for all the fruitful discussions and tips about my research. I have learnt and benefited a lot from many of his comments on how to prepare and present the research results to various audiences.

I would like to thank Professor Dr. Thomas Rösger for accepting the role as the co-examiner of this thesis and for his valuable comments to improve this work.

The financial support of BKW FMB Energie AG and EOS Holding SA is gratefully acknowledged.

I thank many of my colleagues at LEC, ETH Zürich for their cooperation and encouragement. I thank Marlene Hegner for taking care of many of the administrative stuff, for her sympathy and for the short talks about the Persian and Swiss culture. I would like to thank Flori Alickaj for always being ready to help out and readily have an answer to all electronic questions. I would like to thank Gülru Koçer, Balaji Subramanian and Anika Aurbach for their support of my measurement campaigns; Samira Jafari and Andrea Mazzetti for their cooperation with all the CFD simulations. I would like to acknowledge Jonas Kazda for his help during my measurement campaigns.

The cooperation of all external organizations and wind farm operators who let me perform measurements at their sites is gratefully acknowledged. In this regard, I would like to acknowledge Juvent SA, EOS Wind Deutschland GmbH, PNE Wind AG, SEIC-TELEDIS SA, SwissWinds Development GmbH and German Meteorological Service (Deutscher Wetterdienst). In particular, I would like to warmly acknowledge the support of Gregor Gloystein of EOS Wind Deutschland GmbH, Dr. Udo Rummel and Dr. Frank Beyrich of German Meteorological Service, Daniel Würsten and Pierre Berger of BKW FMB Energie in performing the measurement campaigns.

My highest acknowledgement goes to my family in Iran for their never-ending support. In particular to my parents for the entire endeavor they made to provide me with the first-level education and for motivating me to achieve my life goals. Their lessons and pieces of advice are always appreciated, respected and remembered. Finally, I would like to thank my wife, *Niloofar*, for her endless love and patience. Pursuing this work would have been definitely not possible without all her emotional support, understanding and encouragement.

Mohsen Zendehbad
Zürich, December 2016

Contents

Abstract	v
Zusammenfassung	vii
Acknowledgments	xi
Contents	xiii
List of Tables	1
List of Figures	2
1 Introduction	7
1.1 Motivation	7
1.2 State of the art	9
1.2.1 Experimental analysis of wake downstream of wind turbines	9
1.2.2 Wind flow field around forests	10
1.2.3 Wind turbine's aeroelastic deflections and load alleviation	11
1.3 Research objectives	12
1.4 Thesis outline	13
2 Methodology	15
2.1 Experimental tools	15
2.1.1 Mobile laboratory, windRoverII	15
2.1.2 Opto-mechanical platform	19
2.2 Measurement sites	19
2.2.1 Juvent wind farm, complex forested terrain	19
2.2.2 EOSH wind farm, flat forested terrain	19

2.2.3	AltenbruchII wind farm, flat unforested terrain	20
2.2.4	Collonges and Martigny wind turbines	24
2.2.5	Gries wind turbine	24
2.2.6	Lindenberg meteorological observatory (Falkenberg)	24
2.3	Measurement procedure and data processing	27
2.3.1	Wind turbulence	27
2.3.2	Time-averaged 3D wind vector in wind-turbine scale	29
2.3.3	Time-averaged 2D wind vector in wind-farm scale	31
2.3.4	Tower deflection and calculation of damping ratio	33
2.4	Uncertainty analysis	33
2.5	Other tools	37
2.5.1	RANS CFD tool, MULTI3	38
2.5.2	ETH sub-scale wind turbine facility	38
3	Validation experiments	39
3.1	LiDAR versus Meteorological mast and SODAR	39
3.2	Volumetric time-averaged 3D wind vector	40
3.3	LiDAR versus drone system	42
3.4	Opto-mechanical platform versus strain gauge	43
4	Wind turbine operation in non-uniform flow	45
4.1	Wind flow field in scale of wind farm	45
4.2	Wind flow field on the scale of a wind turbine	47
4.3	Power generation in wake	47
4.4	Impact of operating conditions on wake propagation	50
4.4.1	Wake recovery in double-wake	50
4.4.2	Wake flow in non-uniform inflow	51
4.5	Full-scale experiments versus CFD and Sub-scale model	53
4.6	Concluding remarks	61
5	Forests and wind energy	63
5.1	Impact of forested fetch on wind turbulence	66
5.1.1	Impact of turbulence on power fluctuations	66
5.2	Impact of forested fetch on structural loads on wind-turbine towers	68
5.3	Generalized model of impact of forest on downstream flow field	70
5.4	Considerations for installing wind farms in forested terrain	76
5.4.1	Annual energy yield	77
5.4.2	Power curve scatter	79
5.4.3	Power deficit due to wake	80
5.4.4	Maintenance requirements	82
5.5	Concluding remarks	84

6	Structural vibration during steady and transient operation	87
6.1	Upstream conditions; terrain topology and wind turbulence	87
6.2	Geometry and structural deflections of a full-scale wind turbine	91
6.3	Damping ratio of tower during transition to cut-off of power	94
6.4	Tower deflections during normal operation	98
6.4.1	Power Spectrum Density (PSD) of tower deflection	98
6.4.2	Impact of yaw misalignment on tower deflection	99
6.4.3	Tower first harmonic of different wind turbines	101
6.5	Concluding remarks	103
7	Conclusions	105
7.1	Concluding remarks	105
7.2	Future work	107
	Bibliography	109
	A. Nomenclature	119
	B. List of publications	121
	C. Curriculum Vitae	123

List of Tables

2.1	Example configurations of LiDAR.	17
2.2	Salient characteristics of turbines at AltenbruchII wind farm.	24
2.3	Uncertainties in the measured quantities.	34
3.1	Comparison of LiDAR line-of-sight wind velocity measurement with meteorological mast and SODAR.	40
4.1	The rms difference of measured and predicted horizontal wind speeds. The rms differences are related to the distribution of horizontal wind speed in the range of $5D - 1D$ upstream and the range of $1D - 7D$ downstream of the turbines of Fig. 4.10.	56
5.1	Summary of fault durations derived from event-logs of turbines in forested and unforested fetch.	84
6.1	Comparison of turbine characteristics in the high-wind and low-wind cases. . .	98
6.2	The turbines whose tower's first harmonic are shown in Fig. 6.11. Hybrid material is steel and concrete.	103

List of Figures

1.1	Historical evolution of diameters of modern wind turbines.	9
2.1	Measurements of wind speed with LiDAR is based on Doppler frequency shift.	16
2.2	WindRoverII, mobile laboratory equipped with 3D scanning LiDAR system. .	18
2.3	WindRoverII, mobile laboratory equipped with 3D scanning LiDAR system. .	18
2.4	Optomechanical platform.	20
2.5	Layout of Juvent wind farm; a 29MW Wind farm located in complex terrain in western Switzerland. Map of (a) surface elevation, and (b) land cover. . . .	21
2.6	Layout of EOSH wind farm; a 28MW wind farm located in flat terrain in eastern Germany. Map of (a) surface elevation, and (b) land cover. Close-up view of Turbine 10 and 14 is shown in Fig. 5.1	22
2.7	Layout of AltenbruchII wind farm; a 26MW wind farm located in flat terrain in northern Germany. Map of (a) surface elevation, and (b) land cover.	23
2.8	Collonges and Martingy wind turbines located in complex terrain in southern Switzerland. Map of (a) surface elevation, and (b) land cover.	25
2.9	Gries wind turbine located in highly complex terrain in southern Switzerland. Map of (a) land elevation, and (b) land cover.	26
2.10	Lindenberg meteorological observatory (Falkenberg), located in eastern Germany.	27
2.11	The volumetric, time-averaged measurements of the three-dimensional wind velocity are made in the volume whose planform is shown with the blue dashed line. The bottom and top heights of the measurement volume are 50m AGL and 170m AGL, respectively. The reference undisturbed vertical profile of wind speed is measured at the location of the filled triangle symbol.	29
2.12	Reference wind condition at the three measurement points that are used for the volumetric time-averaged measurements of the three-dimensional wind velocity vector.	30

2.13	The layout of optimum positions determined to scan upstream and downstream of 9 wind turbines of the wind farm. Wind direction is 150° , shown with the yellow line.	32
2.14	Flowchart diagram of uncertainty propagation considering all sources of uncertainty in the measured Cartesian velocity vector.	35
2.15	Effect of number of PPI scans on the RMS error in the LOS component of wind speed.	36
2.16	The budget of uncertainty in measurements of the 2D wind vector. Turbine numbers are shown in Fig. 2.7.	37
3.1	Comparison of the line-of-sight wind velocity measured with the mobile LiDAR to simultaneous measurements by SODAR and an instrumented meteorological mast.	40
3.2	Validation measurements are performed at Lindenberg Meteorological Observatory (Falkenberg).	41
3.3	Comparison of (a) wind speed, and (b) wind direction from LiDAR 3D wind measurement to simultaneous SODAR measurement. The RMS differences are 0.3m/s and 3.4° , respectively.	42
3.4	Comparison of the line-of-sight wind velocity measured with the 3D scanning LiDAR to simultaneous measurements using ETH's instrumented drone. . . .	43
3.5	Comparison of the PSD of sideways tower deflections measured with the optomechanical platform and with strain gauges. The PSDs are normalised with the respective maximum amplitudes. The close-up inset compares the PSDs over the range 0.23Hz - 0.30Hz	44
4.1	The horizontal wind speed measured in the hub-height plane of wind turbines at AltenbruchII wind farm (Section 2.2.3). Wind direction is shown with the blue line. Number of each turbine within the wind farm is shown next to the turbine symbols. Dash-dot line shows the wake centerline downstream of Turbine 4 and Turbine 9. Velocity distribution over dashed line is shown in Fig. 4.5.	46
4.2	Vertical profile of wind direction during measurements of Fig. 4.1. The hub height of various turbines of the wind farm are shown with the dashed lines. .	47
4.3	Horizontal wind speed measured in the hub-height plane of wind turbines at EOSH wind farm (Section 2.2.2). Wind direction is shown with the black line. Turbines of the wind farm are shown with black circles. The turbines shown with black triangles are from another wind farm. The number of each turbine within the wind farm is shown next to the turbine symbols. Streamwise wake recovery over dash-dot lines are shown in Fig. 4.6. Spanwise distribution of wake deficit over dashed lines is shown in Fig. 4.7.	48

4.4	Plan view of the measurement volume within which measurements of time-averaged wind vector are made. Measurements of the LOS wind speed component are made from position 1, position 2 and position 3. Turbines are shown with white squares.	49
4.5	(a) power generation of wind turbines during measurements shown in Fig. 4.1. Power generation levels are extracted from SCADA of the turbines, and (b) spanwise distribution of velocity deficit downstream of Turbine 2 in Fig. 4.1. .	50
4.6	Velocity recovery in the wake of Turbine 3 (single-wake) and Turbine 2 (double-wake) of Fig. 4.3. Dash-dot line shows the model resulted from full-scale measurements [1] with drone.	51
4.7	Spanwise distribution of velocity deficit downstream of Turbine 14 of Fig. 4.3.	52
4.8	Time-averaged measurements of the wind vector in the volume shown in Fig. 4.4. Results are shown in three vertical planes at $Y/D = -1.8$ (downstream of Turbine 1), $Y/D = 0$ (upstream and downstream of Turbine 4) and $Y/D = 1.8$ (downstream of Turbine 2), (a) axial wind speed, (b) lateral wind speed and (c) vertical wind speed.	55
4.9	Vertical profiles of wind speed at $1D$ upstream and downstream of Turbine 4.	56
4.10	Horizontal wind speed at AltenbruchII wind farm (Section 2.2.3). Wind direction is shown with the blue line. (a) measurements, and (b) simulations with CFD tool MULTI3.	57
4.11	Streamwise distribution of horizontal wind speed. (a) Turbine 1, and (b) Turbine 5. The turbines are shown in Fig. 4.10.	58
4.12	Spanwise distribution of velocity deficit in the wake of Turbine 2 of Fig. 4.1. .	59
4.13	Comparison of time-averaged measurements and CFD prediction of axial wind speed. The results are shown in three vertical planes at $Y/D = -1.8$ (downstream of Turbine 1), $Y/D = 0$ (upstream and downstream of Turbine 4) and $Y/D = 1.8$ (downstream of Turbine 2), (a) Measurements, and (b) CFD predictions. CFD and measurements are compared along the black dashed lines in Fig. 4.14.	60
4.14	(a) Streamwise evolution of the hub height wind speed in the wake of Turbine 1 and (b) Spanwise (lateral) distribution of the axial wind speed at hub height at a distance of $1D$ downstream of Turbine 4.	61
5.1	Close-up view of the positions of Turbines 10 and 14 relative to the forest edge. The layout of the complete wind farm is shown in Fig. 2.6. The range of wind directions over which the direction-wise AEY are evaluated are shown with the dashed and solid lines.	64
5.2	Westward landscape at the tower of turbine with forested fetch. The vertical dash-dot red lines correspond to the wind directions shown in Fig. 5.1. The forest of interest is comprised of Tsuga trees.	65

5.3	Vertical profiles of undisturbed wind speed and direction, (a) wind speed, (b) wind speed on semi-log scale and (c) wind direction.	65
5.4	TI upstream of turbines along LiDAR beams with elevation angles 0° , 7.5° , 15° , 22.5° and 30° ; the wind direction is from left to right, and the wind turbines are located at a distance of $X = 45H_{forest}$. a) TI upstream of the turbine with flat fetch (Turbine 10 in Fig. 5.1) b) TI upstream of the turbine with forested fetch (Turbine 14 in Fig. 5.1); the forest edge is at $X = 0H_{forest}$. The red dashed lines show the vertical extent swept by the rotor of the turbine.	67
5.5	Vertical profiles of TI at (a) $X = 10H_{forest}$, (b) $X = 20H_{forest}$ and (c) $X = 30H_{forest}$	68
5.6	Power fluctuations measured at Martigny wind turbine, section 2.2.4. The dashed lines are linear fits at each wind speed bin. The fitted line equation in each wind speed bin is shown next to the line.	69
5.7	Deflection of the tower head of the turbine with flat fetch (Turbine 10 in Fig. 5.1) during three phases of (i) feathered-blade (highlighted in green), (ii) transition to operation (highlighted in yellow) and (iii) operation (highlighted in red).	70
5.8	PSD diagram of tower tip vibrations, (a) during feathered-blade mode of the turbines, (b) during operation of the turbines.	71
5.9	Schematic of the analytical solution provided in [2].	72
5.10	Map of land cover at measurement site. The vertical profile in undisturbed flow is measured at Position 1. Vertical profiles at $5H_{forest}$, $25H_{forest}$ and $45H_{forest}$ downstream of the forest edge are respectively measured at Position 2, 3 and 4. Wind directions during measurements are shown with red and yellow lines.	73
5.11	Vertical profile of wind speed for undisturbed flow (a) horizontal wind speed, and (b) velocity deficit calculated with the same convention as Equ. 5.1.	73
5.12	Vertical profile of velocity deficit at $5H_{forest}$ downstream of forest edge.	74
5.13	Streamwise velocity recovery downstream of a forest edge.	75
5.14	Vertical profile of the velocity deficit downstream of a forest. The predictions from the model are shown with the blue lines. Measurements at Position 3 and 4 in Fig. 5.10 are shown with black stars. Red circle shows the equivalent velocity deficit of power loss for a turbine operating at $45H_{forest}$ downstream of forest.	76
5.15	(a) Deficit in direction-wise AEY of a turbine with forested fetch relative to turbine with flat fetch (Turbine 14 and 10 in Fig. 5.1, respectively); the deficit is normalised relative to the direction-wise AEY of turbine with flat fetch, (b) direction-wise AEYs of turbines with flat and forested fetch.	78
5.16	Wind rose at the location of EOSH wind farm, detailed in 2.2.2.	79
5.17	The power deficit of wind turbine versus the streamwise extent of forested fetch.	80
5.18	Normalized power curve scatter for six wind turbines in three wind farms.	81

5.19	Impact of turbine separation distance on the power deficit due to the wake from upstream turbines. The symbols show the deficit in the direction-wise AEY measured on the turbines' SCADA. The solid and dashed lines show the deficit predicted using the in-house CFD tool, MULTI3.	82
5.20	Component-wise maintenance of turbines averaged over 7 years; the scheduled annual and bi-annual maintenance of turbines is excluded.	83
6.1	Surface elevation and extent of forested fetch upstream of Turbines 10 and 11 along the wind direction. The thicker line indicates the extent of the forest. The measurements of turbulence are made at the location shown by the blue triangle. The location of Turbines 10 and 11 is shown in Fig. 2.5.	88
6.2	Vertical profiles of (a) wind speed and (b) wind direction measured in undisturbed wind.	89
6.3	(a) Time-series of TI, and (b) PSD of turbulence, measured upstream of Turbines 10 and 11 in Juvent wind farm, section 2.2.1. The black dashed line in Fig. 6.3b shows the slope in the inertial sub-range.	90
6.4	Measured geometries of tower, nacelle and blades of turbine 1 (3.0MW Vestas V90). Note that for the sake of clarity, the scale of the x-axis is expanded relative to the y-axis.	92
6.5	Simultaneous measurements of a) wind speed and b) blade deflections of the same turbine as in Fig. 6.4.	93
6.6	Measured deflections of the tower of the same turbine as in Fig. 6.4, in the wind conditions shown in Fig. 6.5a.	94
6.7	Time histories of: (a) hub height wind speed; (b) blade pitch angle (the blue dash-dot line is a quadratic fit); (c) generator torque (the blue dash-dot line is a linear fit); (d) rotor speed; and (e) tower tip deflection. The time histories are shown during transient power cut-off. Case 1, high-wind case, is shown with dashed lines. Case 2, low-wind case, is shown with solid lines. The red dash-dot line in Fig. 6.7e shows the predicted tower deflection from a free oscillation SDOF model.	97
6.8	PSD of sideways tower deflections of tower head during normal operation. The black dashed line shows $-5/3$ slope corresponding to the inertial range of turbulence that is shown in Fig. 6.3. The red dash-dot line shows the response of a forced vibration SDOF model. The green highlighted area shows the range of rotor speeds.	99
6.9	Time histories of nacelle direction, wind direction and yaw misalignment. . . .	100
6.10	(a) Amplitude of tower deflections at the first natural frequency, and (b) damping ratio, as a function of yaw misalignment. The red dashed line in Fig. 6.10b shows the damping ratio during power cut-off.	102
6.11	Tower's first harmonic for the turbines detailed in Table 6.2. Tower hub height is shown with the black dashed line. The right y-axis is shown in reverse direction.	104

Chapter 1

Introduction

1.1 Motivation

Over the past decade the global installed wind capacity has increased eight fold from 48GW in 2004 to 370GW in 2014. In 2014, there was a 44% growth of installed wind capacity compared to the previous year with 51.5GW of new installed capacity, 97% of which was installed onshore [3]. Such staggering growth of wind energy has three practical consequences:

- a) Wind energy is produced in larger scale, that is wind-farm scale, rather than the scale of single isolated wind turbines.
- b) Due to scarcity of available land, wind energy production is driven to less benign environments, previously considered unsuitable, such as complex terrains and forested areas.
- c) Wind turbines of larger size are constructed for more efficient and cost effective exploitation of available resources.

a) Operation of wind turbines in wind farms: Reducing the cost of wind-generated electricity in wind-farm scale requires the improved operation of existing wind farms and the optimised micrositing of wind turbines in future wind farms. Wakes are reported to result in 10-20% lower energy yields of wind farms [4]; these lower yields translate into lower revenue and profitability for the wind farms' owners. There are also up to 80% higher fatigue loads on wind turbines that operate in wakes [5]. These higher loads result in higher maintenance costs. An improved knowledge of the characteristics of wakes is thus important in the design and operation of wind farms. There are ongoing efforts to develop better simulation tools to model the atmospheric flow and wakes in wind farms [6–8] and to optimise the micrositing of wind turbines [9–12]. While wind tunnels may be used to

support these efforts, the Reynolds numbers in wind tunnels are two to three orders of magnitude smaller than in the full-scale of a utility-size wind farm. As physical processes such as the turbulent mixing and entrainment of the wakes, amongst other processes are dependent on the scale of the Reynolds number, detailed measurements in utility-scale wind farms are required.

b) Operation of wind turbines in less benign environments; forests: Efficient use of available land is required in order to keep up with the rapid development of onshore wind energy. Given the regulatory restrictions on siting of wind farms in urban areas [13], onshore wind farms are mostly installed in rural areas. As the rapid growth of the onshore wind sector continues, it is increasingly the case that wind farms will be in close proximity to forested areas. Nevertheless, the impact of forest-elevated turbulence levels on wind turbine operation is not completely understood. Since elevated turbulence levels can increase fatigue loads on turbines [5], an improved understanding of the impact of a forested fetch on the power generation and maintenance cost of wind turbines is required. In spite of the commercial sensitivity, there are reports of up to 15 tower collapses and 30 structural failures of blades per year [14]. Hence an improved knowledge of the impact of a forested fetch on the wind flow field and the operation and maintenance of turbines can contribute towards improving the reliability of wind turbines that are sited close to forested areas.

c) Construction of wind turbines of larger size: In order to better exploit sites of limited area for onshore wind farms and to leverage the fixed cost elements of the support structures and undersea cable installations for offshore wind farms, the diameters of wind turbines have continually increased over the past 25 years, Fig. 1.1; [15]. Wind turbines with hub heights of 135m and blade lengths of 80m are now being developed [16]. As these larger wind turbines are structurally more flexible than earlier designs, an improved knowledge of their modal damping characteristics is required for an accurate estimation of the fatigue life. The damping of wind turbines arises from two sources: (i) material damping within the structural components of the turbine and its foundation, and (ii) aerodynamic damping that results from the aero-mechanical interactions between the wind turbine's rotor and wind. While the former, material damping, is present during both the operation and idling of the turbine, the latter is absent during idling; hence for an accurate estimate of aeroelastic damping, it is required that measurements be made on rotating wind turbines.

In addition to the characterization of modal parameters, a recent study has shown that turbines with larger tower deflections have up to 2.2 times longer downtimes, due the more intense vibrations of components in the nacelle [17]. Studies of the structural flexibility of wind turbines can provide guidelines for the alleviation of loads on turbines. Although these studies are largely derived from onshore turbines, such guidelines can support approaches to alleviate loads on offshore turbines, where the foundation, which is

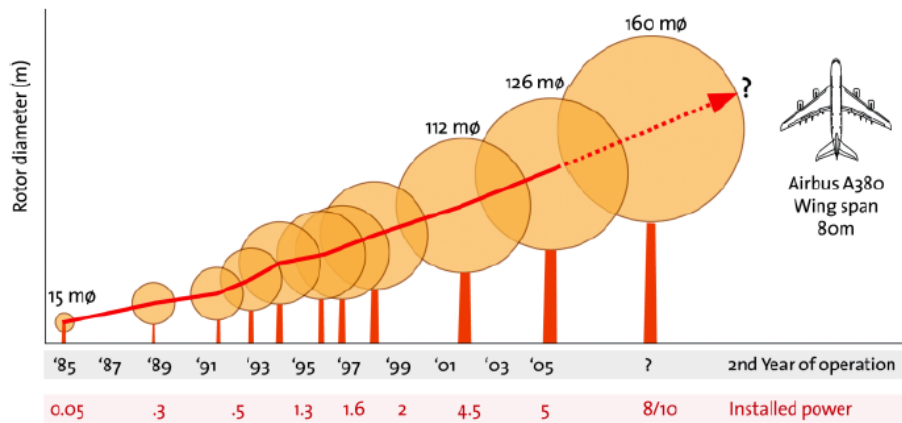


Figure 1.1: Historical evolution of diameters of modern wind turbines.

subject to the loads, comprises up to 25% of the total cost [18]. In addition to optimising the tower mass and reducing the cost of the turbine [19], an improved understanding of the sources of loads on wind turbine can help to reduce incidences of structural failure, which, as earlier discussed, currently number 15 tower collapse incidences per year [14].

1.2 State of the art

1.2.1 Experimental analysis of wake downstream of wind turbines

Wind tunnels have been used to examine details of wake evolution [20, 21]. However, the wake is characterised by physical processes such as turbulent mixing, large scale entrainment of high and low kinetic energy fluid, etc., all of which are Reynolds number dependent. As the Reynolds numbers on sub-scale models in wind tunnels are one to two orders of magnitude smaller than on full-scale turbines, measurements in wakes of full-scale wind turbines are imperative. Meteorological masts equipped with anemometers have been used to measure the detailed wind vector in the field [22]. However spatial changes, such as the velocity recovery in the wake, cannot be assessed from a meteorological mast since from the perspective of the land area of coverage, the meteorological mast provides only a point measurement. Furthermore, the installation of meteorological masts is cumbersome. Although a series of meteorological masts can be used to measure the wake recovery, the series is only suitable for specific wind directions. On the other hand, characteristics of the wind field over an area can be measured with remote sensing devices. Although only a line-of-sight component of the wind velocity is measured, remote sensing devices such as LiDARs, SODARs [23] and Radars [24] are well suited for measurements in wind farms. Dual-LiDAR and multiple LiDAR systems [23, 25–27] and radar [28] have been used to measure the two-dimensional and three-dimensional wind speed components in wakes.

However remote sensing techniques have relatively high costs within the context of the development and/or operating costs of wind farms. Therefore there is a strong interest to accomplish accurate measurements of the three-dimensional velocity field in wind farms using a single LiDAR, if these techniques are to gain more widespread usage in the wind energy sector. In the fields of environmental monitoring [29–31] and urban mapping [32], LiDAR systems have been installed onto a vehicle in order to make measurements over large areas/volumes. The present work demonstrates the application of a single mobile-LiDAR to make measurements of the three-dimensional time-averaged velocity field in the atmospheric flow and wakes of utility scale wind farms.

1.2.2 Wind flow field around forests

Computational fluid dynamic simulations [33–36] have been used to investigate turbulence generation above and downstream of forests. Large eddy simulations [34] show the presence of a complex vortical structure above the canopy that is initiated from $9H_{forest}$ downstream of the forest edge. Reynolds-averaged Navier-Stokes simulations of the flow over forests were performed in [35], where TKE as high as twice the upstream TKE was predicted downstream of the forest. Modelling of the forest as a porous medium was suggested in [36]. In addition to computational fluid dynamic simulations, sub-scale models [37, 38] and full-scale experiments have also investigated the turbulence generation above and downstream of forests. Full-scale measurements have mainly been made with meteorological masts [39–42]. Field measurements show that the effect of forests extends above the forest canopy up to a height of 5 times the height of the forest, as well as downstream of the forest [39]. Measurements above the forest canopy show there is a negligible difference in turbulence anisotropy upstream and downstream of forest edges [40, 41]. Shear generation above the forest canopy is suggested to be the principal source of turbulence generation above and below the forest canopy, as TKE in the sub-canopy layer is observed to be one-tenth of TKE above the canopy [42]. Since meteorological masts yield only point measurements, limited information about the spatial distribution of flow field around forests are obtained. However due to abrupt geometric changes at forest edges, flow around forests is expected to have considerable spatial gradients. Remote sensing devices such as LiDAR provide wind flow field measurements over the spatial extent of an area or a volume. [43, 44] used a continuous-wave laser LiDAR in a vertical VAD profiler mode for measurements of wind speed and flow tilt angle at the forest edge. [45, 46] used a 3D scanning LiDAR system for flow field measurement at the forest edge. Although several studies have addressed the impact of forests on the wind flow above and downstream of forests, only a few studies have assessed the impact of elevated turbulence levels on wind turbine’s operation and power generation. The impact of elevated turbulence on turbine performance has been investigated in [37] using a sub-scale wind tunnel model. However, as turbulence generation is dependent on Reynolds number, there is a concern with wind tunnel experiments since the full-scale Reynolds numbers are three to four orders of magnitude larger than in the

wind tunnel. In addition to a Reynolds number mismatch, the use of stiff forest tree models in wind tunnels is a concern since, the top of the forest canopy may oscillate due to the flexibility of trees; the attendant vorticity generation mechanisms are absent in sub-scale experiments. [47] used meteorological mast measurements to assess the impact of turbulence at the forest edge on wind turbine loads. These measurements showed that turbulence dissipation rate is 9 times higher over forest, compared to undisturbed flow and turbulence anisotropy is the same in forested and unforested terrain.

1.2.3 Wind turbine's aeroelastic deflections and load alleviation

Previously, modal analysis of the stresses or deflections in the structure of a manually excited turbine has been used to estimate the damping. The step relaxation technique has been applied on parked wind turbines [48, 49]. Osgood et al. [50] used cable shakers to excite the structure of a parked wind turbine. Although the excitation of a parked turbine is practically easier than the excitation of a rotating turbine, as discussed above, the modal parameters of a parked turbine are related only to the material damping if there is no aerodynamics loading. Hansen et al. [51] used variations in the pitch control system and generator torque to excite an operational wind turbine. Moreover modal analysis of an operating wind turbine, on which there is no induced change to the turbine's operational characteristics, has been reported. James et al. [52] extracted the modal parameters from correlation functions that were calculated from measured time histories. Ozbeck et al. [53] and Hansen et al. [51] used operational modal analysis tools to estimate the modal parameters of rotating wind turbines.

While a broad range of approaches has been used to excite turbines, different methods have also been applied to measure the strains and/or deflections. Strain gauges embedded in the tower and blades have been used [51, 53]. However, strain gauges are sensitive to lightning and to the presence of electro-magnetic fields. Moreover, the attachment of strain gauges to the structure of the turbine requires a transmission path along which the signals may be transmitted; this is not always feasible for today's large wind turbines. On the other hand, optical methods are non-intrusive and do not suffer from the aforementioned limitations of strain gauges. Thus, photogrammetric and interferometric techniques have been used to measure deflections on wind turbines [53–55]. Nevertheless, even the use of these optical techniques requires that the structure of the turbine be covered with reflective spots in order to increase the amount of backscattered light. Achieving this coverage can be a burdensome task for large wind turbines, and invariably limits the acquisition of modal damping data to very few test cases.

In addition to modal analysis, one goal of an experimental study of wind turbine's aeroelastic deflection is to alleviate loads on the turbine's structure during normal operation and transient conditions. Different strategies for load reduction are discussed in [56, 57]. The concept of individual pitch control [58] was introduced to reduce blade

stresses in sheared inflow. Blades with variable geometries, such as trailing edge flaps [59], micro tabs [60], blade morphing and active twist [61] have been developed to manage the larger load fluctuations of long-bladed wind turbines. Nacelle-mounted LiDARs [62] have been used to pitch the blades based on a feed-forward control loop in order to improve turbine fatigue life due to gusts. Although such studies are quite numerous, experimental data to validate and develop these new concepts is still lacking. Unlike sub-scale measurements, in a water channel [63] or wind tunnel [64,65], full-scale experiments do not suffer from a mismatch of Reynolds number.

1.3 Research objectives

The objectives of this research are to experimentally investigate the wind flow field in full-scale wind farms and to assess the impact of environmental conditions on the performance of wind turbines. Such an experimental database can also be used to validate and develop the in-house numerical and semi-empirical models. The required measurements are made using the LEC's mobile laboratory, windRoverII, which is equipped with a 3D scanning LiDAR and a portable opto-mechanical platform. In addition to the hardware, the developed automated software minimizes the required human intervention to enable a single operator to perform field measurements that require simultaneous motion of windRoverII, operation of LiDAR and the opto-mechanical platform. Thus to accomplish the objectives, the following tasks were undertaken:

- Develop a cost-effective experimental technique for measurements of time-averaged wind vectors in the scale of the wake of a single turbine, as well as in the scale of a wind farm.
- Understand and quantify the impact of non-uniform incoming wind flow on the wake flow field downstream of the wind turbine.
- Develop a full-scale experimental database to validate and develop in-house numerical simulation and semi-empirical models of the wake flow field.
- Quantify the impact of forested fetch on the turbulence levels of downstream flow.
- Assess the impact of forested fetch on the power generation, structural loads and maintenance requirements of downstream wind turbines.
- Develop generalized semi-empirical models of impact of forests on the downstream wind flow field.
- Quantify aeroelastic deflection of a wind turbine's tower using a portable opto-mechanical platform, which requires no modification on the turbine.
- Suggest a possible methodology for load alleviation on the structure of a wind turbine during steady operations, as well as transition to power cut-off.

1.4 Thesis outline

Chapter 1 The introduction begins with the motivations of the work. Secondly, the state of the art in incorporating LiDAR systems for full-scale experiments is described. Literature review also includes recent research on measurements of structural deflections and load assessments on full-scale wind turbines. The chapter concludes with the objectives of the present research.

Chapter 2 This chapter elaborates on the research methodology. First, the specifications of the developed and used tools are given. Second, the layout, topography and other specifications of measurements sites are given. The last section of this chapter details the procedure of various measurement schemes that are presented in this work.

Chapter 3 The validation experiments and cross-comparisons between the main measurement systems of this research and the other independent systems are provided in this chapter.

Chapter 4 This chapter includes results of the novel measurement approach to calculate the time-averaged wind vector using a single mobile-based LiDAR. This scheme is first applied to investigate the wind flow field in two wind farms and secondly to detail the flow features in the wake of a wind turbine operating in the disturbed flow. Next, the comparisons of full-scale results with CFD simulations and semi-empirical models are provided.

Chapter 5 This chapter elaborates on the impact of forested fetch on the wind flow field and the performance of downstream turbines. First, the influence of forested fetch on turbulence intensity is quantified. Second, the influence of higher turbulence regime on power generation and structural deflections is assessed. Third, based on the analytical solutions in literature and experimental results, a generalized model of impact of forest on downstream flow is developed. Fourth, based on the experimental observations, long-term data attributed to the performance of wind farms in forested and unforested terrain are analysed.

Chapter 6 In this chapter, time-resolved tower vibrations are used to characterize the modal parameters of wind turbine towers during operation and transient to power cut-off. Second, using a high-frequency measurement of yaw misalignment and tower deflections, correlation between yaw misalignment and tower vibration is investigated. Next, correlation between the material and stiffness of wind turbines' tower is investigated.

Chapter 7 The concluding remarks and key findings of this work are summarised in this chapter.

Chapter 2

Methodology

2.1 Experimental tools

2.1.1 Mobile laboratory, windRoverII

A LiDAR system, Long Range Inland Galion model, is used to measure the line-of-sight component of wind speed. The measurement of the line-of-sight component of wind speed is based on the Doppler shift of backscattered laser from aerosols in the atmosphere. As shown in Fig. 2.1 a laser beam with a known frequency, f_1 , is emitted along scanning direction and is backscattered by the atmospheric aerosols. The frequency of the backscattered laser beam is shifted due to the motion of atmospheric aerosols along the line-of-sight direction of LiDAR. The shift between the frequency of the emitted laser, f_1 , and the mean frequency of the backscattered beam, f_2 , is proportional to the mean speed of aerosols. The standard deviation of the frequencies in the backscattered beam, f_σ , is proportional to the turbulence in the wind at the location of the aerosols. As the emitted laser must be eye-safe, and the backscatter has very low power levels (of the order of 10^{-7} of the emitted laser power) multiple pulses are accumulated to achieve meaningful measurement signals. This is accomplished by using laser pulse rates (of order of 10s kHz) that are of order 10^4 larger than the relevant frequencies to be measured in the atmospheric flow or wakes of wind turbines. The distance to the aerosols from LiDAR is calculated from the time-of-flight; specifically the duration between the emission of a laser pulse and the detection of the backscattered signal is used to calculate the distance to the aerosols. Such methodology allows a LiDAR with pulsed laser to measure the line-of-sight wind speed at measurement gates with different radial distances.

The laser pulse rate is $15kHz$ with an energy per pulse of $5\mu J$. Each measurement of line-of-sight wind speed is based on averaging over several laser pulses emitted at $15kHz$. The accumulation period is the required time for emitting the laser pulses for each mea-

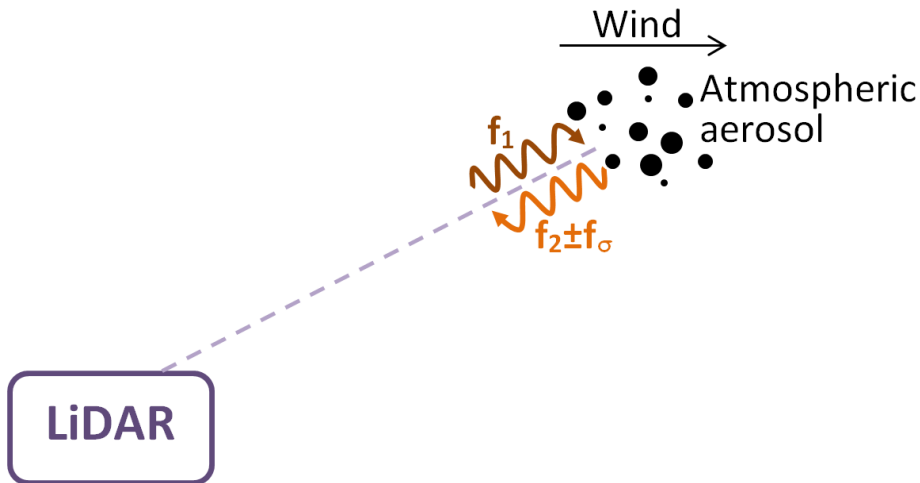


Figure 2.1: Measurements of wind speed with LiDAR is based on Doppler frequency shift.

surement of line-of-sight wind speed. The update period is the total time duration between each measurement, which includes the accumulation period and the data processing period. The accumulation period and the update period depend on the user-defined number of pulses per measurement and the maximum measured distance, which can be respectively set within a range of 2'000 – 10'000 and 500m – 6000m. Table 2.1 shows example configurations of LiDAR and the corresponding accumulation and update period. LiDAR system is used in two different modes of operation. The first mode of operation, detailed in Section 2.3.1, is fast-response low-range scanning for measurements of wind turbulence. In the first mode of operation, the number of pulses per measurements is set to 4'000 pulses per measurements to achieve shorter update period (1.1s). In the second mode of operation, related to measurements of wind vector detailed in Section 2.3.2 and Section 2.3.3, the number of pulses per measurements is set to the maximum limit of 10'000 to increase the maximum available range, which consequently results in increasing the update period to 3.7s.

Although the maximum measured distance is set by the user, the actual measured distance depends on the strength of the backscattered signal from the atmospheric aerosols. Measurements of line-of-sight wind speed are filtered out based on the signal-to-noise ratio given by the ratio of signal power spectrum of accumulated pulses to the noise power spectrum. A signal-to-noise threshold of 1.01 is used for this filtration. Depending on the concentration of the atmospheric aerosols, the maximum available range of LiDAR, with signal-to-noise ratio of higher than 1.01, can vary from 800m to 3000m. The maximum range of 3000m is mostly experienced before and after rain when the atmospheric moisture increases the intensity of the backscattered signal. Clouds, dense fog, rain and snow obstruct the passage of the laser beam and hence limit the operation of LiDAR during

Table 2.1: Example configurations of LiDAR.

Maximum range (km)	Pulses per measurement	Accumulation period (ms)	Update period (ms)
4	2'000	100	1000
	10'000	500	3700
2	2'000	100	700
	10'000	500	2800
0.5	2'000	100	600
	10'000	500	2000

such incidences. The laser's focal point of LiDAR can be set within a range of $250m$ to infinity to improve the signal-to-noise ratio at a certain distance from LiDAR. Setting the focus point of LiDAR to infinity improves LiDAR's maximum range.

The spatial resolution (radial distance between measurement gates along the laser beam) is set by the user and can vary between $12m$, $18m$, $24m$ and $30m$. The measurements at range gates with radial distance less than $60m$ are erroneous and the corresponding data are filtered out in the post-processing stage.

The accuracy in measurements of line-of-sight wind speed is $0.25m/s$ based on the comparative measurements that are presented in section 3.1. The uncertainty in measurements of wind vector depends on up to 9 variables measured from multiple position and ranges from $0.25m/s$ to $1.1m/s$. The derivation of uncertainty in the case of wind vectors is further discussed in Section 2.4. The LiDAR has a 3D scanning head that allows for volumetric scanning with an accuracy of 0.1° over $0^\circ - 360^\circ$ in the azimuth and -17° to 90° in elevation; the angular accuracy has been verified using an electronic spirit level DIGILEVEL Laserliner whose accuracy is 0.1° .

The LiDAR system is installed in a mobile laboratory, windRoverII, Fig. 2.2. During measurements the LiDAR laser head is raised through an opening in the roof of windRoverII by an elevator. A $5kW$ generator and a battery bank provide electric power for the laboratory's on-board systems. WindRoverII can accommodate a two-person crew for off-road measurement campaigns.

The position of windRoverII during measurement campaigns is determined and recorded using the GPS sensor, u-blox LEA 6H GPS module, with an accuracy of $2.5m$. The pitch and roll angle of LiDAR is measured using two redundant sensors, that is IMU sensor ArduIMU v3 and the LiDAR integrated sensor, CXTLA01. The GPS and IMU sensors are installed in a sealed box near the ceiling of windRoverII, Fig. 2.3, and connected to LiDAR via a cable. LiDAR measurements of LOS component, together with measurements position and attitude are used for post-processing of results.



Figure 2.2: WindRoverII, mobile laboratory equipped with 3D scanning LiDAR system.

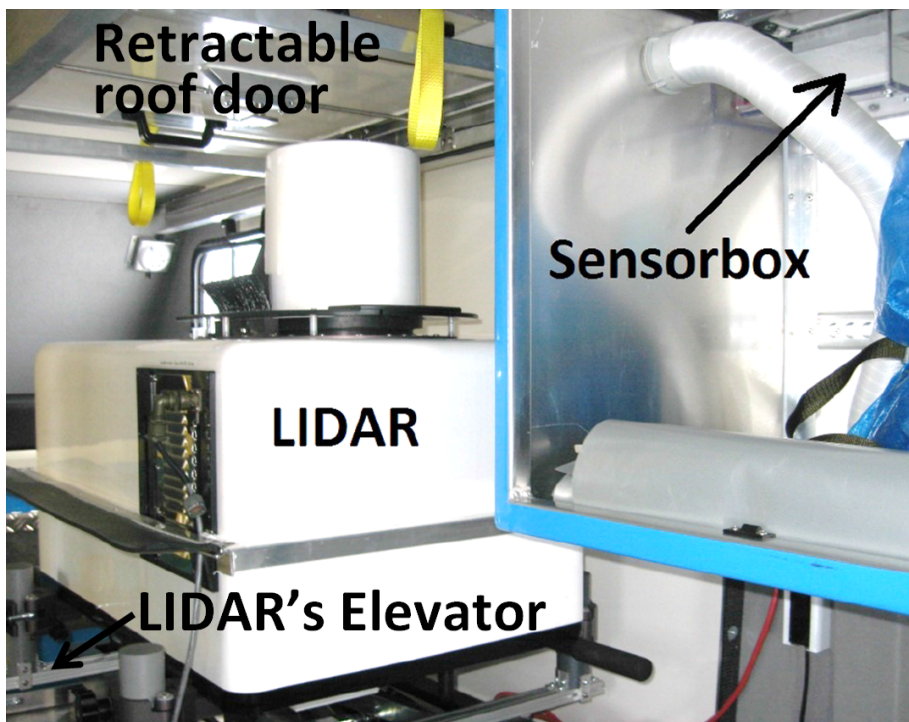


Figure 2.3: WindRoverII, mobile laboratory equipped with 3D scanning LiDAR system.

2.1.2 Opto-mechanical platform

The aeroelastic deflections of wind turbine towers are measured using an opto-mechanical measurement system. Figure 2.4 shows the portable system that has been developed in this work. The primary component of this system is an infrared laser that measures the distance to solid objects based on the time-of-flight principle. The laser has a beam divergence of 1.7mrad and a wavelength of 905nm . The accuracy in the measurement of distance is 1.9cm . The measurement range is up to 300m . The measurement data are acquired at a rate of 200Hz . This system is well suited for measurements on multi-megawatt wind turbines that have tower heights in the range of $60\text{m} - 110\text{m}$ and rotor rotational frequencies in the order of 0.25Hz . The laser head is mounted on a platform with two rotational degrees of freedom, such that azimuthal and elevation scans of the laser beam can be made with angular resolutions of 0.06° ; which corresponds to linear resolution of 30cm at the maximum range. The data acquisition systems and controllers are installed below the platform.

2.2 Measurement sites

2.2.1 Juvent wind farm, complex forested terrain

Juvent wind farm is a 29MW wind farm that is located in the complex terrain of western Switzerland. The elevation map in Fig. 2.5a shows the topography at the wind farm. It can be seen that there is a valley that extends in the west-southwest to east-northeast direction. The wind farm is on the elevated region north of the valley, in a region whose elevation varies from approximately 1100m to 1250m . This wind farm is comprised of 16 Vestas V90 turbines with a rated power of 2MW , rotor diameter of 90m and hub height of 95m AGL. The cut-in and rated wind speeds are 4m/s and 12m/s , respectively. The land cover, shown in Fig. 2.5b, is comprised of patches of coniferous forest and agricultural land.

2.2.2 EOSH wind farm, flat forested terrain

EOSH wind farm is a 28MW wind farm that is located in the flat terrain of eastern Germany. The maps of surface elevation and land cover at the wind farm are shown in Fig. 2.6a and Fig. 2.6b, respectively. There are forests, with an average height of 40m AGL along the southern and eastern sides of the wind farm, and a forest with an average height of 20m AGL along the northern and north-western sides of the wind farm. The land cover along the west side of the wind farm is mostly agricultural land. The wind farm is equipped with 14 Vestas V80 turbines with rated power of 2MW and rotor diameter of 80m . The hub height of turbines 1-9 is 100m AGL and the hub height of turbines 10-14 is 78m AGL. The turbine cut-in and rated wind speeds are 4m/s and 15m/s , respectively.



Figure 2.4: Optomechanical platform.

2.2.3 AltenbruchII wind farm, flat unforested terrain

AltenbruchII wind farm is a 26MW wind farm in northern Germany. The elevation map is shown in Fig. 2.7a, and it can be seen that the wind farm is located in flat terrain near to the coast. The surface cover of the area is shown in Fig. 2.7b; the main vegetative feature is open agricultural fields, but there are some patches of trees on the west side. The wind farm is equipped with 9 turbines whose salient characteristics are summarised in Table 2.2.

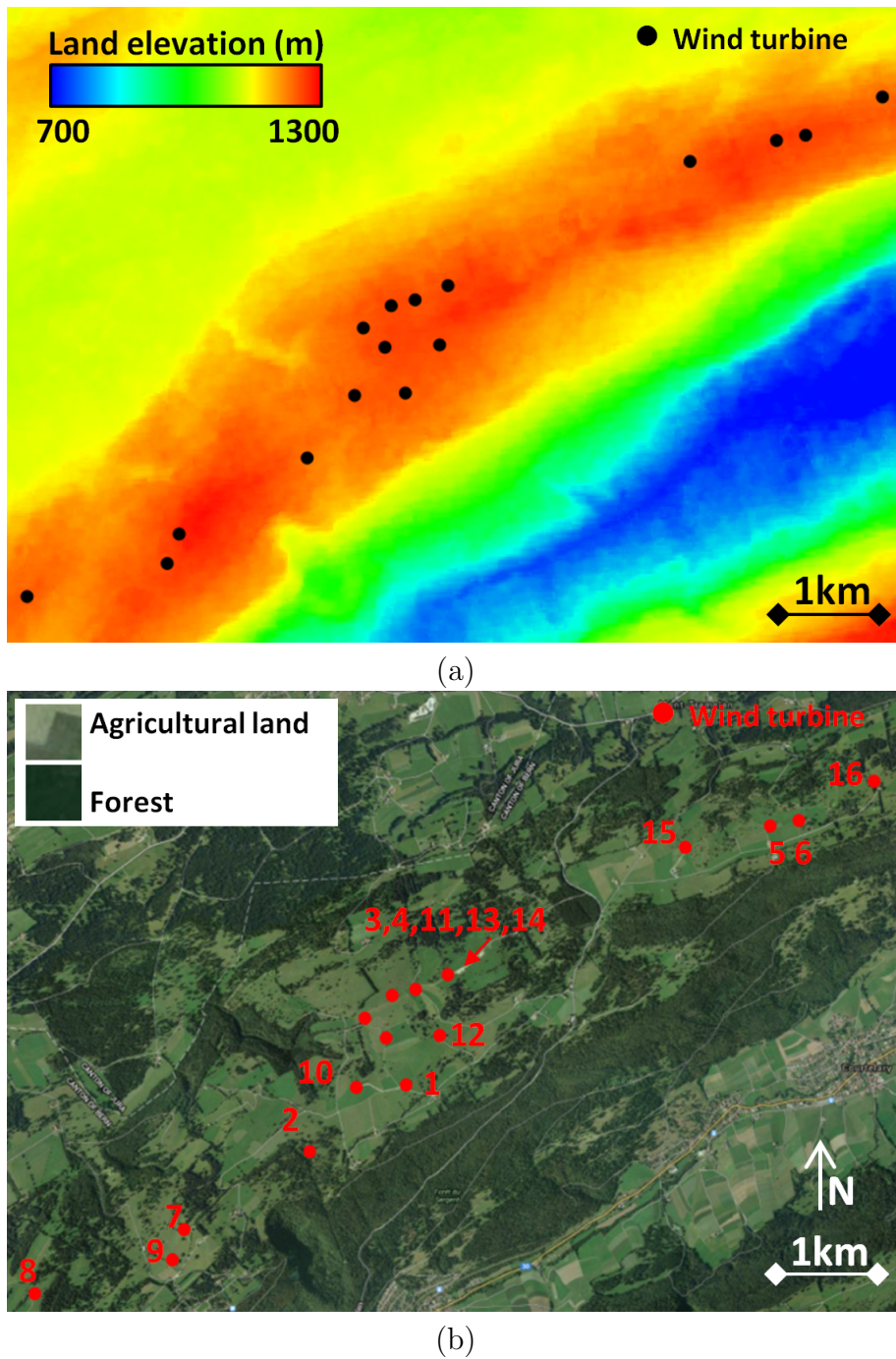
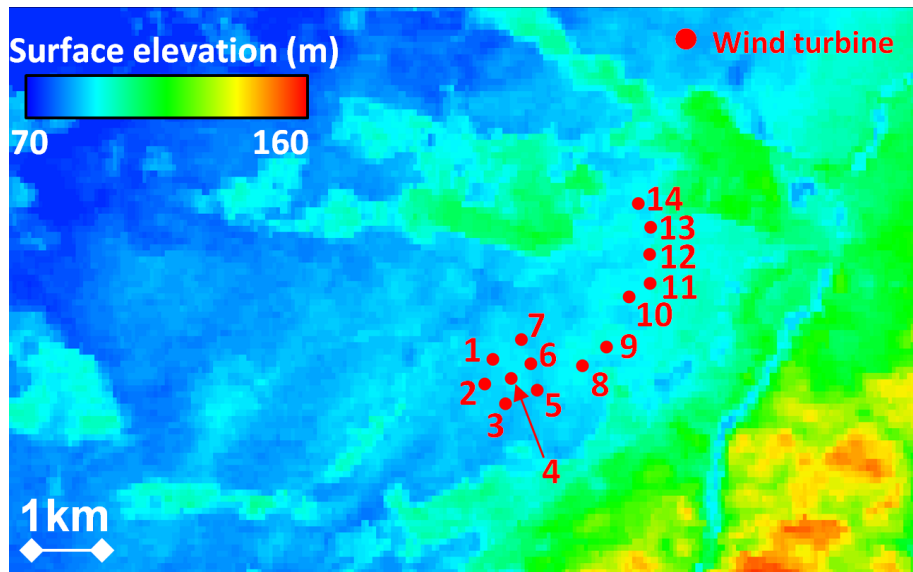


Figure 2.5: Layout of Juvent wind farm; a 29MW Wind farm located in complex terrain in western Switzerland. Map of (a) surface elevation, and (b) land cover.

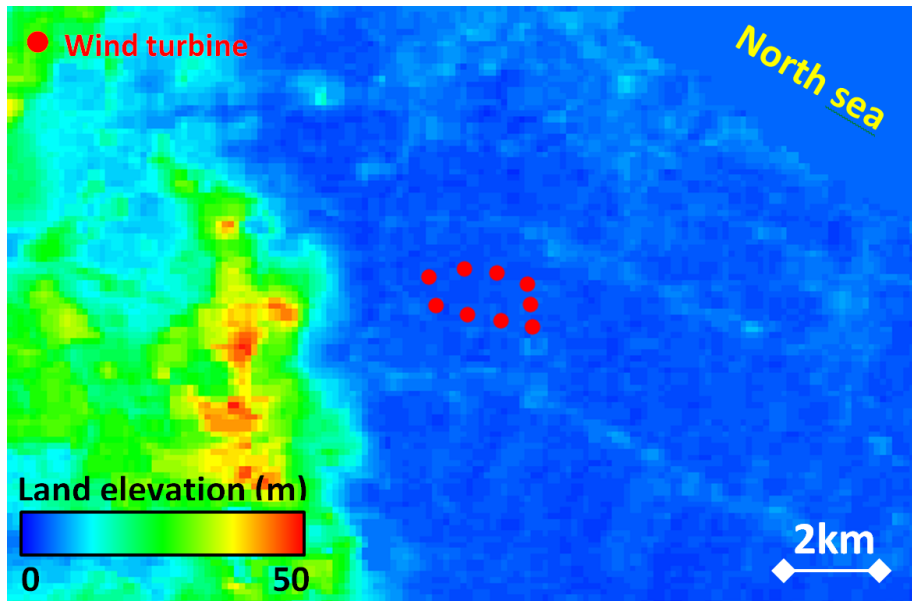


(a)



(b)

Figure 2.6: Layout of EOSH wind farm; a 28MW wind farm located in flat terrain in eastern Germany. Map of (a) surface elevation, and (b) land cover. Close-up view of Turbine 10 and 14 is shown in Fig. 5.1



(a)



(b)

Figure 2.7: Layout of AltenbruchII wind farm; a 26MW wind farm located in flat terrain in northern Germany. Map of (a) surface elevation, and (b) land cover.

Table 2.2: Salient characteristics of turbines at AltenbruchII wind farm.

Turbine No.	Type	Rated power (MW)	Hub height (m)	Rotor diameter (m)
1,3,5	Siemens SWT 3.6	3.6	93	107
2,4,6	Vestas V90	3.0	105	90
7,8,9	Vestas V80	2.0	60	80

2.2.4 Collonges and Martigny wind turbines

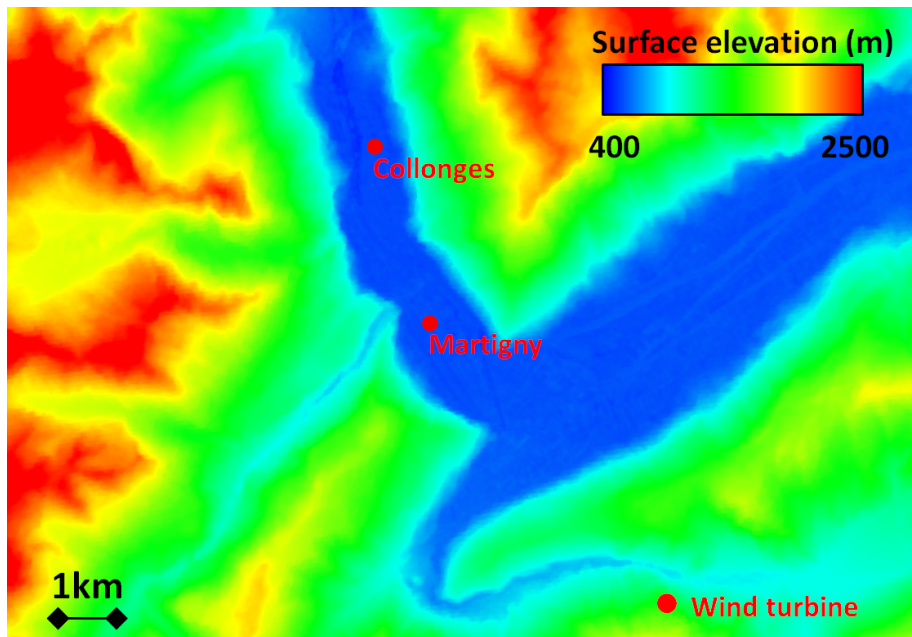
The Collonges and Martigny wind turbines are located in complex terrain in southern Switzerland. The elevation map at this site is shown in Fig. 2.8a. It can be seen that the turbines are located in a valley that extends from north-west to southeast. The valley is around 2000m deep, relative to the nearby mountains. Due to the terrain topology, the wind direction is stable, with a dominant direction that is parallel to the valley. The prevalent land cover, shown in Fig. 2.8b, is agricultural land and the surrounding mountains. The Collonges turbine is an Enercon E70 turbine with rated power of 2MW, rotor diameter of 70m and hub height of 98m AGL. The cut-in and rated wind speeds are 2m/s and 14m/s, respectively. The Martigny turbine is an Enercon E82 turbine with rated power of 2MW, rotor diameter of 82m and hub height of 98m AGL. The cut-in and rated wind speeds are 2m/s and 13m/s, respectively.

2.2.5 Gries wind turbine

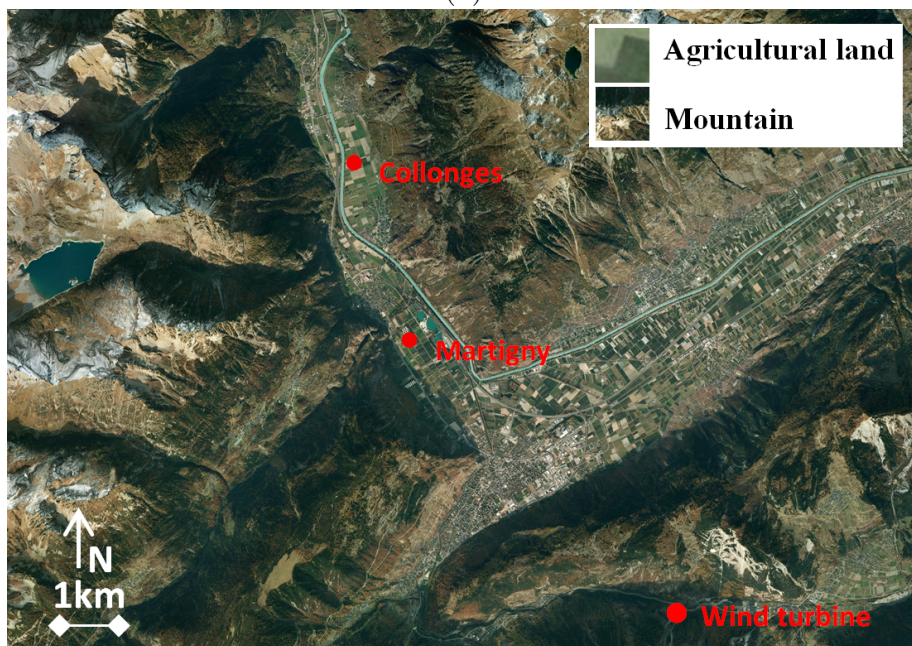
The Gries wind turbine is located in highly complex terrain in southern Switzerland. The elevation map at this site is shown in Fig. 2.9a. It can be seen that the surface elevation changes in 1800m-2800m range in 1km distance from the turbine. There is a 400m-high peak east of the turbine and a 500m-deep valley located north west of the turbine. The land cover, shown in Fig. 2.9b is steep mountainous area and a small water reservoir south west of the turbine. The Gries turbine is an Enercon E70 with a rated power of 2.3MW, rotor diameter of 71m and hub height of 85m. The cut-in and rated wind speeds are 2m/s and 14m/s, respectively.

2.2.6 Lindenberg meteorological observatory (Falkenberg)

Lindenberg meteorological observatory (Falkenberg) is located in flat terrain in eastern Germany. This observatory is equipped with a meteorological mast with cup anemometers and wind vanes at heights of 40m AGL and 98m AGL. The cup anemometers are Adolf Thies GmbH & Co model 4.33303.22.000 and wind vanes are model 4.3121.32.000. The measurement accuracies are 0.3m/s and 2.5° in wind speed and direction, respectively. As

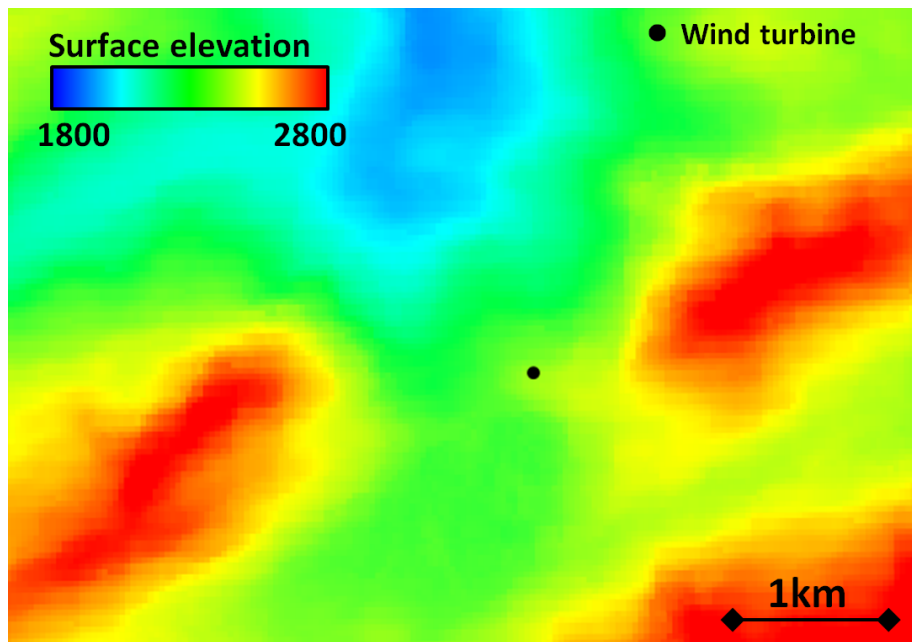


(a)

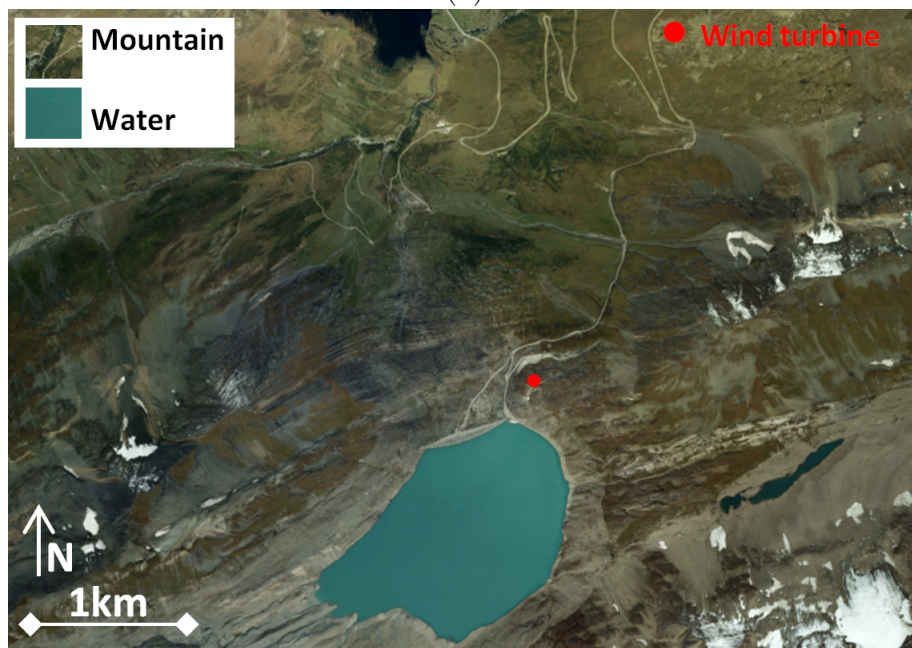


(b)

Figure 2.8: Collonges and Martigny wind turbines located in complex terrain in southern Switzerland. Map of (a) surface elevation, and (b) land cover.



(a)



(b)

Figure 2.9: Gries wind turbine located in highly complex terrain in southern Switzerland. Map of (a) land elevation, and (b) land cover.

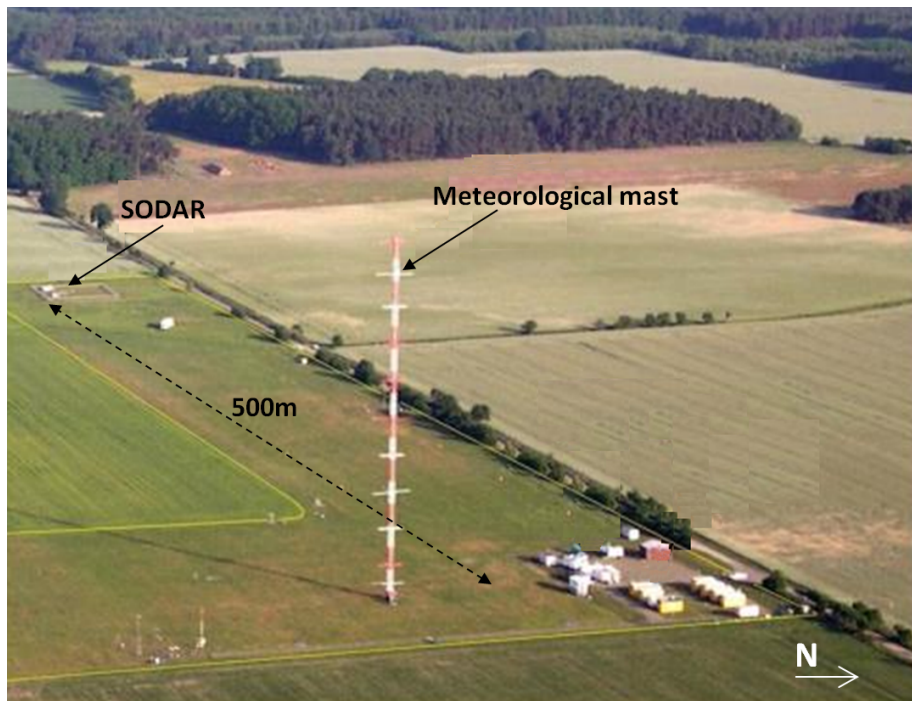


Figure 2.10: Lindenberg meteorological observatory (Falkenberg), located in eastern Germany.

shown in Fig. 2.9, the SODAR is positioned 500m west of the meteorological mast. The surrounding terrain is flat agricultural land with forests 1.3km west of the measurement site. The SODAR is a METEKO DSDPA.90-64 that uses a 1598Hz acoustic signal for measurements with accuracies of 0.3m/s and 3° in wind speed and direction, respectively.

2.3 Measurement procedure and data processing

2.3.1 Wind turbulence

The Turbulence Intensity (TI) is derived from the LiDAR measurements in a stare scanning mode; that is measurements of the Line-Of-Sight (LOS) wind speed along a fixed elevation angle. A 10-minute time series is sampled at a frequency of 0.9Hz at each of the 25 range gates which have a spatial resolution of 30m. The time series of measured wind speeds are filtered based on the signal-to-noise ratio. Local interpolation in time is used to estimate

the filtered wind speeds. The TI is given as:

$$TI = \frac{\sqrt{\frac{1}{3}(\overline{u'^2} + \overline{v'^2} + \overline{w'^2})}}{u_{ref}} \quad (2.1)$$

Since the LOS wind speed is measured, the degree of turbulence anisotropy, Equ. 2.2, is used to bound the range of TI, as the TI is a function of the three Cartesian velocity components, Equ. 2.1.

$$DA = \frac{2\overline{u'^2}}{\overline{v'^2} + \overline{w'^2}} \quad (2.2)$$

The industry standard IEC 61400-1 [66], specifies the standard deviations in the three directions as:

$$\left(\frac{\overline{v'^2}}{\overline{u'^2}}\right)^{0.5} = 0.8 \quad \left(\frac{\overline{w'^2}}{\overline{u'^2}}\right)^{0.5} = 0.5 \quad (2.3)$$

which yields a DA of 2.25. Measurements of ETH Zurich using a wind turbine nacelle-mounted probe [67] and a kite-based probe [68], as well as atmospheric measurements conducted elsewhere [69–71] report DA in the range of 0.8 – 2.28. This range is used to bound the expected range of turbulence intensities that are based on the TI derived from the measurements of the LOS wind speed [17]. In this regard, for different DAs, the fluctuations of wind speed in the LOS direction of the LiDAR beam are related to the wind speed fluctuations in the principal wind directions using:

$$\sigma_u = \frac{\sigma_{u,los}}{\sqrt{\cos^2(\theta) + \left(\frac{\overline{w'^2}}{\overline{u'^2}}\right) \sin^2(\theta) + 2\left(\frac{\overline{u'w'}}{\overline{u'^2}}\right) \cos(\theta)\sin(\theta)}} \quad (2.4)$$

where the components of the turbulence stress tensor are given as:

$$\begin{bmatrix} \overline{u'^2} & \overline{u'v'} & \overline{u'w'} \\ \overline{v'u'} & \overline{v'^2} & \overline{v'w'} \\ \overline{w'u'} & \overline{w'v'} & \overline{w'^2} \end{bmatrix} = \begin{bmatrix} a_{11} & 0 & a_{13} \\ 0 & a_{22} & 0 \\ a_{31} & 0 & a_{33} \end{bmatrix} \quad (2.5)$$

in which the ratio a_{13}/a_{11} is taken as $1/2.4^2$ following [72]. As the coefficients along the diagonal of the stress tensor are a function of DA, σ_u is calculated from Equ. 2.4 for different DAs, and the TI, given in Equ. 2.1, is then calculated as:

$$TI = \frac{\sigma_u \sqrt{\frac{1}{3} \left[1 + \left(\frac{\overline{v'^2}}{u'^2} \right) + \left(\frac{\overline{w'^2}}{u'^2} \right) \right]}}{u_{ref}} \quad (2.6)$$

2.3.2 Time-averaged 3D wind vector in wind-turbine scale

These measurements are made from the three different positions, as shown in Fig. 2.11. The variations of wind speed and wind direction during measurements are monitored with reference measurements, that is SCADA measurements of upstream turbines or VAD scans during measurements.

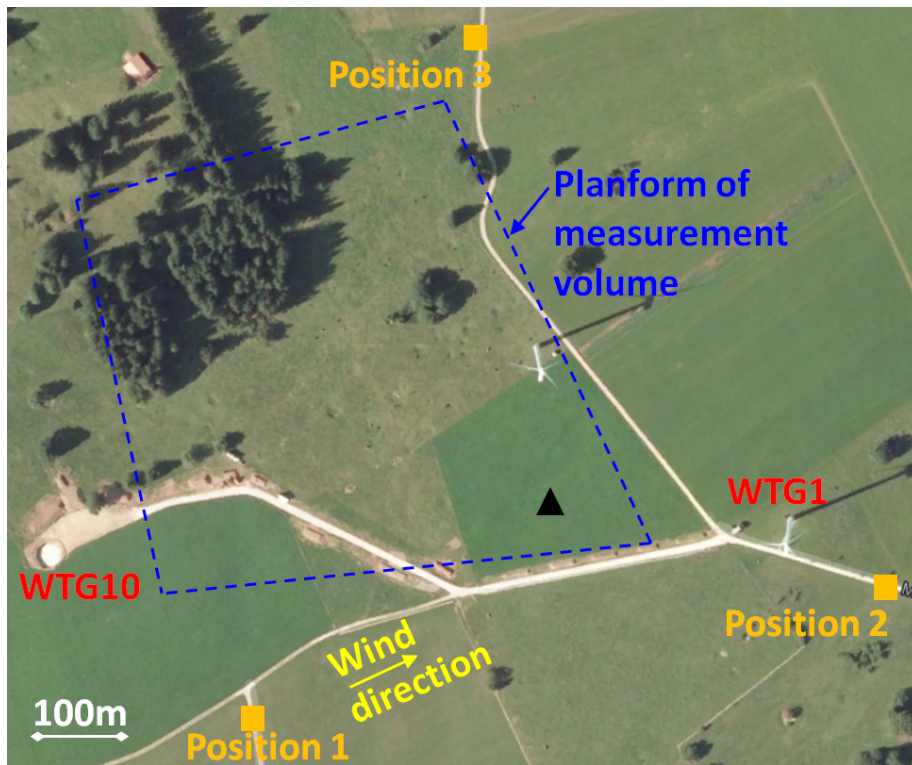


Figure 2.11: The volumetric, time-averaged measurements of the three-dimensional wind velocity are made in the volume whose planform is shown with the blue dashed line. The bottom and top heights of the measurement volume are 50m AGL and 170m AGL, respectively. The reference undisturbed vertical profile of wind speed is measured at the location of the filled triangle symbol.

In the experiment shown in Fig. 2.11, the wind speed differs by less than 14% and the wind direction by less than 5°, Fig. 2.12. As the wind speeds and wind direction

vary little, and since the wind speeds (below rated wind speed) and the variations of wind directions are less than the threshold for initiating yaw indicate that the turbines' operating conditions do not change, the meteorological conditions are considered stable.

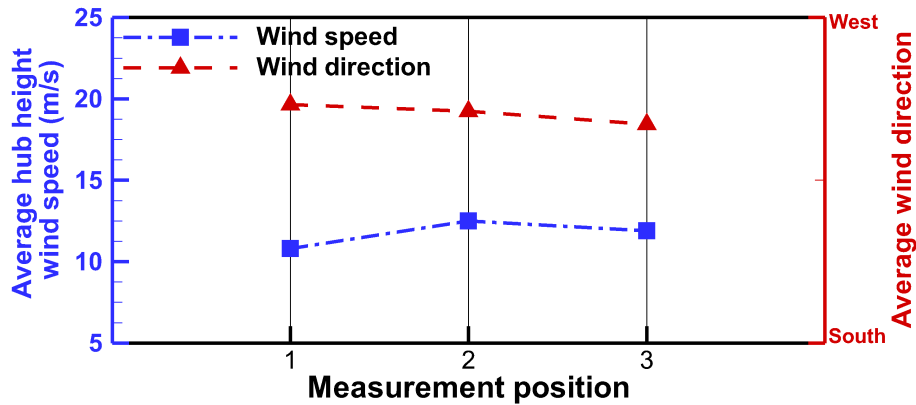


Figure 2.12: Reference wind condition at the three measurement points that are used for the volumetric time-averaged measurements of the three-dimensional wind velocity vector.

The LOS wind speed component is measured in the measurement volume whose horizontal planform is shown by the dashed blue line, Fig. 2.11. The bottom and top heights of this measurement volume are 50m AGL and 170m AGL, respectively. The average density of measurement gates within the volume, which is the ratio of the number of measurement points within the volume to the size of the volume in cubic meter, is set to $5 \times 10^{-4} m^{-3}$. This volumetric density ensures that there is the same linear density in both the azimuthal and elevation directions. From each position, the volume is scanned 10 times. This number of repeated scans ensures that: a) the total duration of measurements is sufficiently short, such that the measurements are unaffected by diurnal wind fluctuations; and b) there is sufficient data to average out the turbulent fluctuations. The scan pattern is comprised of first a series of successive Plan Position Indicator (PPI) scans, at different elevation angles to cover the entire measurement volume, whose planform is shown in Fig. 2.11, and then finally a VAD scan. The vertical profiles of wind speed and direction during each series of PPI scans are measured in VAD scans that are made at the beginning and end of each series of PPI scans. The PPI scans are performed with an angular velocity of $1.8^\circ/s$ and angular resolution of 3° . The ranges of the azimuthal and elevation scans are chosen such that the whole measurement volume is scanned. The LOS wind velocity measurements from the 3 positions are used to calculate the Cartesian components of wind velocity. In order to account for variations within the stable wind conditions during the measurements, the measurement data is filtered and normalised in two steps. In a first step, the wind speed during each PPI scan is calculated following a VAD-processing method. The wake region of the turbines is excluded from the measurements derived from

VAD scans. Azimuthal scans with wind speeds more than 1m/s difference from the mean wind speed are filtered out. Subsequently, the remaining wind speed measurements are scaled relative to the predominant wind condition and averaged. In a second step, the averaged LOS wind velocities at one position are used as the baseline condition, and the measurements from the other two positions are corrected for differences in wind speed and direction relative to the baseline wind condition. The scaling of wind speed in the wake is done over a wind speed range of 1.1m/s. Over this range, the difference between linear and non-linear scaling of wind speeds is negligible, relative to the measurement uncertainty.

2.3.3 Time-averaged 2D wind vector in wind-farm scale

Wind-farm scale measurements of the 2D wind vector are performed at the AltenbruchII (Section 2.2.3) and EOSH (Section 2.2.2) wind farms. From LiDAR scans of LOS components of wind speed, the streamwise and lateral component of wind velocity are calculated at the hub-height plane of wind turbines at the wind farm. The experiment procedure is comprised of four steps; a) preprocessing experiment, b) initialize measurement, c) scanning and d) post-processing results. The developed automatic software minimizes human interaction for performing these four steps.

a) preprocessing: prior to beginning the experiment, the position of available roads for driving and parking windRoverII are defined. Additionally, the GPS position, hub height and rotor diameter of the wind turbines in the wind farm are specified.

b) initialize measurement: immediately before beginning the experiment, the LiDAR maximum scanning range is quantified by assessing the signal-to-noise ratio along the LiDAR's laser beam. In order to quantify the maximum range, the LiDAR is set to stare with an elevation angle of 4° from horizontal. Available range of the LiDAR depends on the environmental conditions, such as the density of moist and particulates in the air, hence the initialization is performed immediately before beginning the experiment. Following stare measurements, the vertical profile of wind speed and wind direction are measured using a VAD scanning scheme during 20 minutes. In addition to measuring the vertical profile of wind speed and direction, the stability of wind conditions is assessed during VAD scans. Subsequently, considering the wind farm layout, the LiDAR's maximum range and wind direction, windRoverII's optimum positions from which upstream and downstream of wind turbines can be scanned are determined. Scanning positions are determined such that up to 3 diameters upstream and 10 diameters downstream of intended wind turbine are within the available scanning range of LiDAR. Despite this restriction, scanning positions must be as far as possible from the intended wind turbine, to minimize laser beam's elevation angle for scanning at the hub-height plane. The observed elevation angles during the measurements are normally less than 4° . For each turbine, two scanning positions are determined to enable calculation of streamwise and lateral component of wind velocity. In order to minimize the uncertainty in measuring the streamwise component, one of

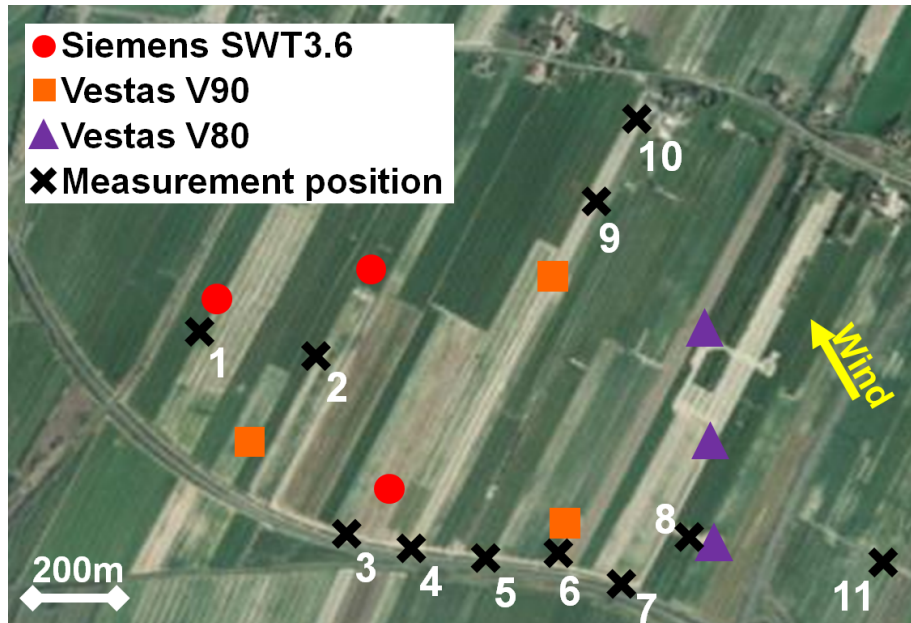


Figure 2.13: The layout of optimum positions determined to scan upstream and downstream of 9 wind turbines of the wind farm. Wind direction is 150° , shown with the yellow line.

the two measurement positions is set such that the line-of-sight direction is parallel to the streamwise direction. Figure 2.13 shows the 11 optimum positions determined at AltenbruchII wind farm to scan the wake flow downstream of nine wind turbines of the wind farm in a wind direction of 150° shown with the yellow line.

c) scanning: based on the optimum positions, determined in the last step, the driver is led to each scanning position. Subsequently, the scanning pattern is determined to measure LOS wind speed at the hub height of wind turbines over an area covering 3 diameters upstream and 10 diameters downstream of the wind turbine. The angular velocity and angular resolutions of the scan patterns are the same as the measurements of the time-averaged 3D wind vector described in previous section. This procedure is repeated to scan from all predefined optimum positions. The scanning period at AltenbruchII wind farm lasted for 2 hours.

d) post-processing: the LOS component on the hub-height plane of each wind turbine scanned from two positions is used to calculate the streamwise and lateral component of wind velocity. Results of this experiment are detailed in Chapter 4.

2.3.4 Tower deflection and calculation of damping ratio

The opto-mechanical system is used for measurements of structural deflection on towers of full-scale wind turbines. The laser head is set to an elevation angle such that the laser beam hits the tip of the tower. Measurements during the period when the rotor direction is parallel/perpendicular to the line-of-sight of the opto-mechanical platform are used in the data processing to measure, respectively, the fore-aft/sideways deflections of tower head. A time series of tower head deflections is sampled at 500Hz. The time series is divided into 1-minute time windows and the PSD of tower head deflections is averaged over all 1-minute windows. Tower damping is estimated using two different models: a free oscillation model and a forced oscillation model. A damped free oscillation of SDOF model is used to estimate the damping of the turbine tower during the transition from normal operation of the turbine to idling. The damped free oscillation of SDOF model is given as:

$$y(t) = ae^{-\zeta\omega_n t} \cos(\omega_n \sqrt{1 - \zeta^2} t - \theta_0) \quad (2.7)$$

$y(t)$ is determined from the tower deflection measurement using the opto-mechanical system. A least squares curve fit of the independent variable t , to the dependent variable $y(t)$, is used to determine the coefficients ζ and ω_n . A damped forced oscillation of SDOF model is used to determine the modal damping parameters during operation of the turbine. This model is relevant since the wind turbine is a lightly damped system. The amplitude response of the SDOF model is given as:

$$|H(\omega)|^2 = \left| \frac{Y(\omega)}{X(\omega)} \right|^2 = \frac{1/k^2}{[1 - (\omega/\omega_n)^2]^2 + [2\zeta(\omega/\omega_n)]^2} \quad (2.8)$$

where $H(\omega)$ is the transfer function, $Y(\omega)$ is the response function of the tower's deflection and $X(\omega)$ is the forcing function resulting from the upstream wind. The response function, $Y(\omega)$, is determined from the PSD of the deflections measured with the opto-mechanical system, whereas the forcing function, $X(\omega)$, is calculated from the PSD of upstream turbulence, which is derived from the simultaneous LiDAR measurements. A least squares curve fit of the independent variable, ω/ω_n , to the dependent variable, $H(\omega)$, is used to determine the coefficients k and ζ . A similar approach to calculate damping ratios has been used in other work [73–75].

2.4 Uncertainty analysis

The uncertainty in the measurement of the time-averaged wind vector is discussed in this section.

Table 2.3: Uncertainties in the measured quantities.

Variable	Measurement uncertainty
LOS wind speed	0.25m/s
Pitch angle	0.1deg.
Roll angle	0.1deg.
Laser beam azimuth angle	0.1deg.
Laser beam elevation angle	0.1deg.
Heading	1deg
Latitude	2.5m
Longitude	2.5m
Altitude	2.5m

a) *time-averaged 3D wind vector in wind-turbine scale*: in order to calculate the time-averaged Cartesian velocity vector 9 variables that are summarised in Table 2.3, are measured from 3 different positions. Table 2.3 also summarises the measurement uncertainties of the instrumentation.

Figure 2.14 shows the flowchart diagram of the uncertainty model that is used to determine the combined uncertainty in the measured Cartesian velocity vector. The method of the Guide to Expression of Uncertainty in Measurement [76] was used to calculate the uncertainty in the Cartesian velocity components. This method is comprised of three steps; in a first step, a mathematical model that is based on the definition of the final measurement is developed. In the present work, the mathematical equations that describe the calculation procedure are used as the mathematical model. In the mathematical model, the direction of the line-of-sight in LiDAR's frame of reference is determined from the azimuthal and elevation angles of the laser beam. The line-of-sight direction is transposed from the LiDAR's frame of reference to the Earth's frame of reference using the heading, pitch angle and roll angle of windRoverII. The location of the range gate within the measurement volume is determined from the altitude, latitude and longitude of windRoverII together with the distance of the range gate. Thus, in the mathematical model the measured LOS wind speed components and LOS directions at the three measurement positions are used to calculate the Cartesian velocity vectors throughout the measurement volume. In a second step the uncertainties of interim measurements as determined from observations, data sheets, etc. are converted to probability distributions. In a last step, the extended uncertainty of the Cartesian velocity vector is calculated by propagating the probability distribution of interim measurands through the mathematical model. The final uncertainty is a function of all measured quantities and their uncertainties. The sources of uncertainties associated with the LiDAR system are from the LOS wind speed component, the azimuth and elevation angles of the laser beam, and the pitch and roll angles of win-

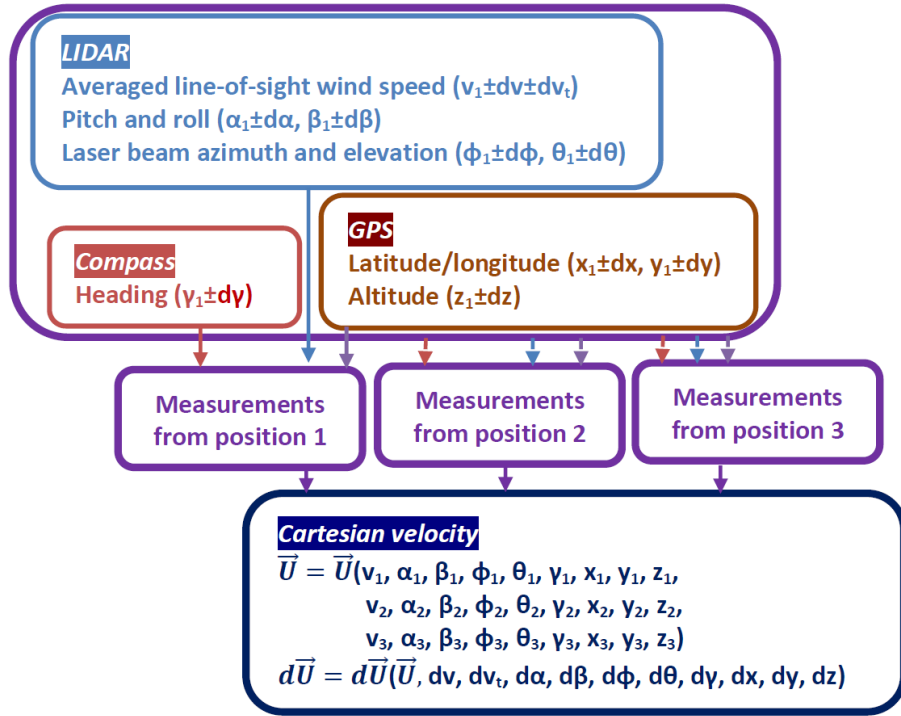


Figure 2.14: Flowchart diagram of uncertainty propagation considering all sources of uncertainty in the measured Cartesian velocity vector.

dRoverII. The sources of uncertainties associated with the GPS and the compass system are from the altitude, latitude, longitude and heading of windRoverII. The high frequency turbulent fluctuations are averaged out by repeat measurements during the 25-30 minute averaging time period at a given position – position 1, position 2 and position 3. The results of a parametric study regarding the effect of the number of PPI scans on the RMS errors of the LOS wind speed are shown in Fig. 2.15. It is seen that there is less than a 1% change in the RMS error for 10 or more scans. The combined measurement uncertainties in all 3 components of the Cartesian velocity are in the range of $\pm 0.25m/s$ to $\pm 1.1m/s$.

b) time-averaged 2D wind vector in wind-farm scale: the uncertainty in the calculation of the 2D wind vector is assessed in the same way as the uncertainty in the measurement of the 3D wind vector. The mathematical model used for this assessment is discussed here. Equ. 2.9 determines how the final measured components are perturbed due to wind direction fluctuations. U and V are the streamwise and lateral components of wind vector, respectively. \vec{U} is the final measured components of wind vector. U' is further expanded

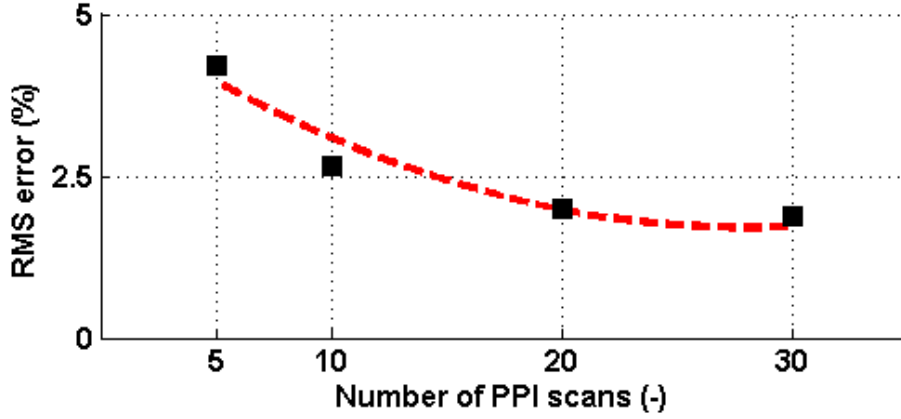


Figure 2.15: Effect of number of PPI scans on the RMS error in the LOS component of wind speed.

in Equ. 2.10. α_e is the uncertainty due to the fluctuations of wind direction.

$$\begin{bmatrix} \bar{U} \\ \bar{V} \\ 0 \end{bmatrix} = \begin{bmatrix} U' \\ V' \\ 0 \end{bmatrix} + \begin{bmatrix} V' \cdot \tan(\alpha_e) \\ U' \cdot \tan(\alpha_e) \\ 0 \end{bmatrix} \quad (2.9)$$

U' is defined in Equ. 2.10. A is a 3×3 matrix detailed in Equ. 2.11. los_i are the line-of-sight components measured with LiDAR. $U_{e,turb}$ is the error due to the turbulent fluctuations of wind speed. $U_{e,gps}$ is the error in wind speed due to the uncertainty in measuring LiDAR's position.

$$\begin{bmatrix} U' \\ V' \\ 0 \end{bmatrix} = A^{-1} \begin{bmatrix} los_1 \\ los_2 \\ 0 \end{bmatrix} + \begin{bmatrix} U_{e,turb} \\ V_{e,turb} \\ 0 \end{bmatrix} + \begin{bmatrix} U_{e,gps} \\ V_{e,gps} \\ 0 \end{bmatrix} \quad (2.10)$$

Matrix A , as defined in Equ. 2.11, is the transfer function between the measured line-of-sight components and the calculated wind vector. θ_i and φ_i are the azimuth and elevation angles of the laser beam, respectively. The azimuth angle is measured from north and elevation angle is measured from the horizontal. The measured angles are perturbed, as shown with θ_e and φ_e , to account for the uncertainty in measuring laser beam orientation.

$$A = \begin{bmatrix} \cos(\varphi_1 + \varphi_e)\cos(\theta_1 + \theta_e) & \cos(\varphi_1 + \varphi_e)\sin(\theta_1 + \theta_e) & \sin(\varphi_1 + \varphi_e) \\ \cos(\varphi_2 + \varphi_e)\cos(\theta_2 + \theta_e) & \cos(\varphi_2 + \varphi_e)\sin(\theta_2 + \theta_e) & \sin(\varphi_2 + \varphi_e) \\ 0 & 0 & 1 \end{bmatrix} \quad (2.11)$$

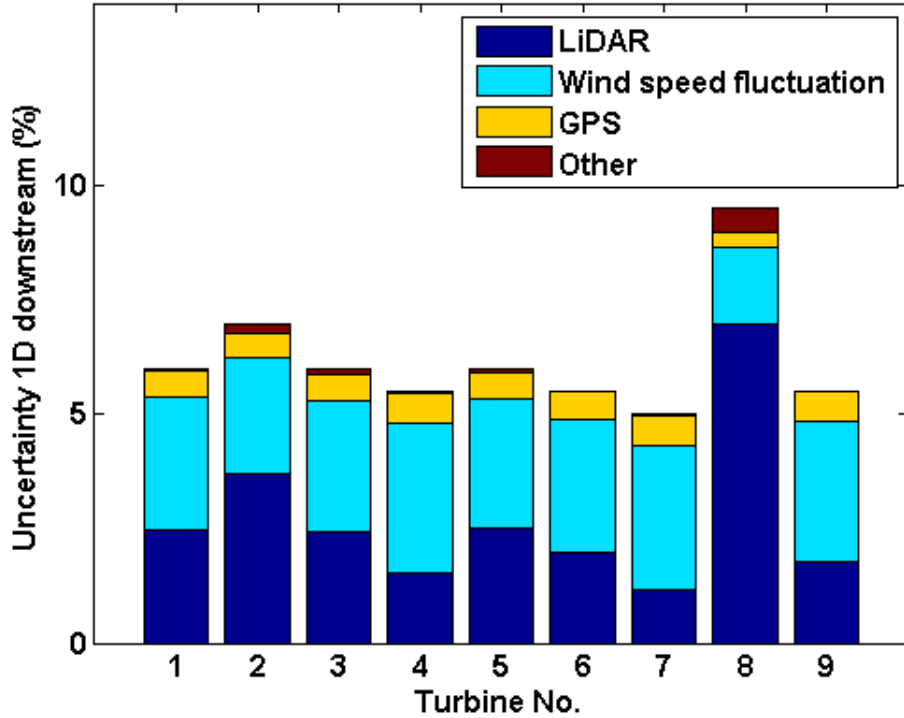


Figure 2.16: The budget of uncertainty in measurements of the 2D wind vector. Turbine numbers are shown in Fig. 2.7.

The calculated uncertainties in measuring the streamwise component of wind speed are shown in Fig. 2.16. The uncertainties are calculated at one diameter downstream of 9 turbines in AltenbruchII wind farm, described in section 2.2.3.

The details of this experiment are provided in section 2.3.3. As observed, the estimated uncertainties are in a range of 5% – 10%. Figure 2.16 also shows the budget of the uncertainty. It can be seen that the dominant contribution to the uncertainty is from the error due to turbulent fluctuations and measuring line-of-sight wind speed. As seen, the uncertainty for Turbine 8 is larger compared to other turbines. The wake flow downstream of turbine 8 is measured from Position 2 and 5 in Fig. 2.13. The large misalignment between line-of-sight direction from both measurement positions and the streamwise direction accounts for larger measurement uncertainty downstream of Turbine 8.

2.5 Other tools

The results of full-scale experiments from the present work are used to validate and develop the numerical and semi-empirical models that are products of the following in-house tools. This section provides a short description of these tools.

2.5.1 RANS CFD tool, MULTI3

MULTI3 is a second order Reynolds-Averaged Navier-Stokes solver that employs an explicit, finite-volume, node-based Lax-Wendroff method [77]. In this solver, wind turbines are modelled as immersed bodies, which simulate both the blockage and the momentum extraction of the turbine. The use of an immersed body does not have the limitations of either an actuator disc model, which oversimplifies the rotor to a disc, or an actuator line model, which requires detailed knowledge of the wind turbine blade's geometry, which is not accessible to others than the turbine manufacturer. The details of this in-house CFD tool are provided in [77].

2.5.2 ETH sub-scale wind turbine facility

In LEC's dynamically-scaled wind turbine test facility, detailed measurements of wind turbine wakes under different ambient turbulence conditions (zero and low ambient turbulence) are made. LEC's dynamically-scaled water channel facility is comprised of a water towing tank and a carriage with the installation of the sub-scale wind turbine and the instrumentation. The carriage has an overall length of 5m. It is positioned on the rails running along each side of the water channel. The carriage can be moved at the desired velocity by a carriage drive motor that is positioned at the end of the channel. In addition to the sub-scale model of the turbine, the carriage can accommodate a probe for flow measurements. The details of this facility is provided in [78].

Chapter 3

Validation experiments

3.1 LiDAR versus Meteorological mast and SODAR

Figure 3.1 compares the 10-minute-averaged wind speeds measured with LiDAR, meteorological mast and SODAR, described in 2.2.6. The LiDAR measurements are averaged over 150 stare scans, performed during each 10-minute time window. The measurements are performed from 100m north of the meteorological mast, position 1 shown in Fig. 3.2. From the meteorological mast and SODAR measurements the line-of-sight component of wind speed in the direction of the LiDAR beam are compared with LiDAR measurements. In order to make the comparisons, different LiDAR elevation angles are used. For the comparison to the anemometers at 40m AGL and 98m AGL respectively on the meteorological mast, LiDAR elevation angles of 22° and 45° , relative to the horizontal, are used. For comparison to the SODAR, a LiDAR elevation angle of 20° , relative to the horizontal, is used. The LiDAR's staring spot is offset 10m from the meteorological mast to avoid the LiDAR measurements from being affected by the presence of mast. The comparisons of the LiDAR to meteorological mast span the low-velocity range of 1m/s to 5m/s, as the measurement station is relatively low, at a height of 98m, whereas the comparisons with SODAR are over a higher velocity range of 5m/s to 12m/s since these measurements are at a height of 200m.

The measured correlation coefficients, Table 3.1, are within the range of 0.92-0.99 for the comparative measurements of remote sensing devices for wind resource assessment reported in [24]. However, the average difference is larger than the nominal 0.05m/s-0.10m/s uncertainty band of LiDAR. The reasons for this larger difference can be the mismatch between the LiDAR's staring point and the locations of the measurement devices on the meteorological mast and SODAR. Additionally, cup anemometers and SODAR are not calibrated to measure the vertical component of wind speed; however, the LiDAR's measurement includes also the vertical component of the wind velocity.

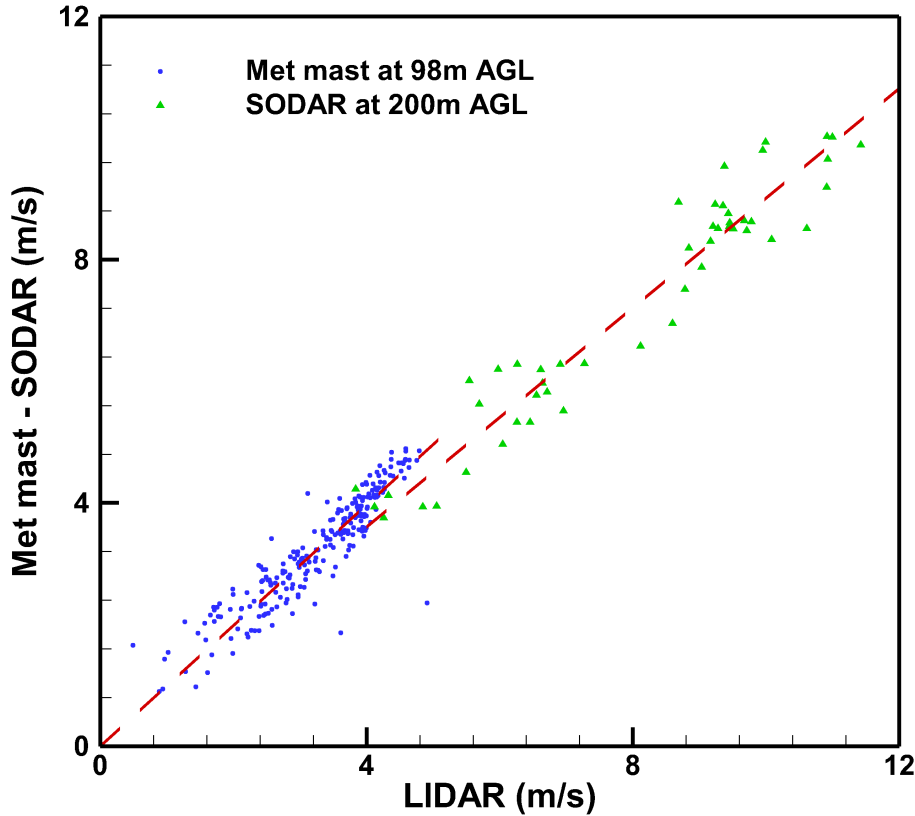


Figure 3.1: Comparison of the line-of-sight wind velocity measured with the mobile LiDAR to simultaneous measurements by SODAR and an instrumented meteorological mast.

Table 3.1: Comparison of LiDAR line-of-sight wind velocity measurement with meteorological mast and SODAR.

Instrument	Height AGL (m)	Correlation coefficient (%)	Average difference (m/s)
Met mast	98	92	0.25
Met mast	40	93	0.30
SODAR	200	96	0.84

3.2 Volumetric time-averaged 3D wind vector

The line-of-sight component of wind speed in the measurement volume shown in Fig. 3.2 is scanned from positions 1-3. The duration of the measurements was one hour. The volumetric measurements made from each position are the same as those described above in section 2.3. Specifically the measurements are comprised of successive PPI scans at

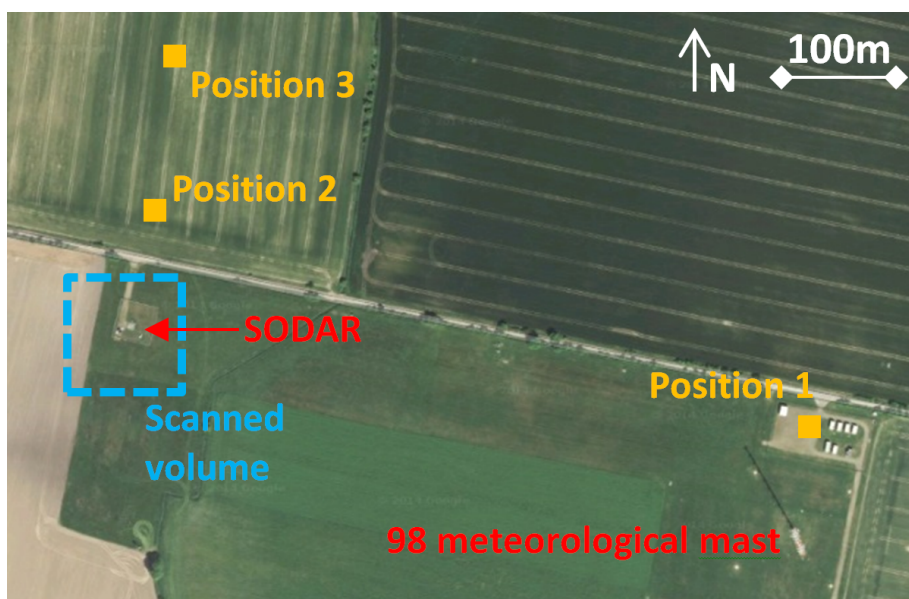


Figure 3.2: Validation measurements are performed at Lindenberg Meteorological Observatory (Falkenberg).

different elevation angles in order to cover the vertical extent of the measurement volume, followed by VAD scans after the series of PPI scans.

The time-averaged vertical profiles of horizontal wind speed and direction are compared in Fig. 3.3. The LiDAR measurements are compared to SODAR measurements that are simultaneously made and averaged over the same hour long period. Overall there is very good agreement between the LiDAR and SODAR measurements. The RMS differences are 0.3m/s and 3.4° , respectively. Also shown by the solid black line in Fig. 3.3 is the difference between the LiDAR and SODAR measurements. As there is no correlation between the difference and the height of the measurements, the differences are attributed to random errors, rather than systematic errors in the measurement procedure.

Interestingly it is observed that from 50m to 200m height AGL, which is typical of the swept height of a multi-megawatt wind turbines' rotor, the wind direction changes up to 40° . This considerable wind veer results in unfavorable variation of incidence angles over one rotor rotation, if a wind turbine were to operate in such conditions. The assessment of velocity triangles at 75% span showed that the observed wind veer causes the incidence angles on the blades to fluctuate with an amplitude of 0.75° over one complete rotor rotation. Since the geometric specifications of the blades are not publicly available, the blade data of NREL 5MW wind turbine, whose blade specifications are openly accessible, are used for this assessment. As flow separation over blade aerofoil occur typically above incidence angle of 12° , the incidence angle fluctuations with 0.5° amplitude have negligible

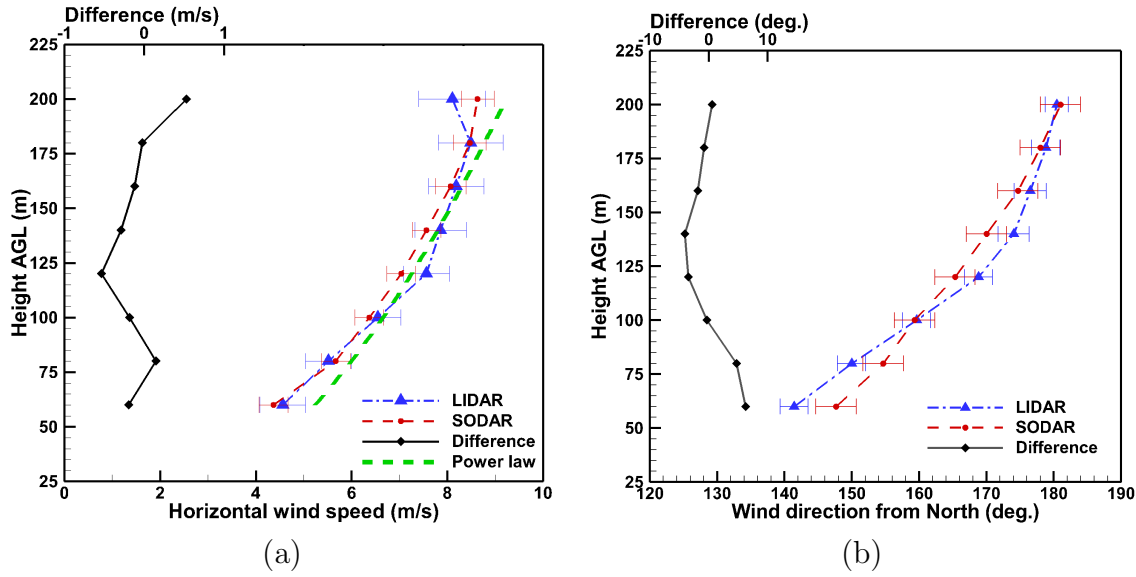


Figure 3.3: Comparison of (a) wind speed, and (b) wind direction from LiDAR 3D wind measurement to simultaneous SODAR measurement. The RMS differences are 0.3m/s and 3.4°, respectively.

impact on the aerodynamic performance of blades.

3.3 LiDAR versus drone system

Wind measurements with the present LiDAR system were compared with ETH's instrumented drone. The instrumented drone [79, 80] is equipped with a fast response aerodynamic probe in order to provide measurements of the wind velocity at a sampling rate of 500Hz. For the present assessment, the drone was programmed to fly along a straight horizontal line passing above the 3D scanning LiDAR system; the LiDAR was programmed to track the drone's trajectory. Since the LiDAR measures the line-of-sight wind velocity, whereas the drone-mounted aerodynamic probe measures the wind velocity vector, from the drone-based measurements the line-of-sight wind velocities were therefore determined at the locations of the LiDAR range gates that coincided with the horizontal flight path. In the conditions of an 8m/s horizontal wind speed, over the range of simultaneous measurements the magnitude of the line-of-sight wind velocity varies monotonically from +4m/s to -2m/s, Fig. 3.4. Overall, the maximum difference between the two measurements, which is less than 15% of the measured wind speed, occurs at a horizontal distance of -80m.

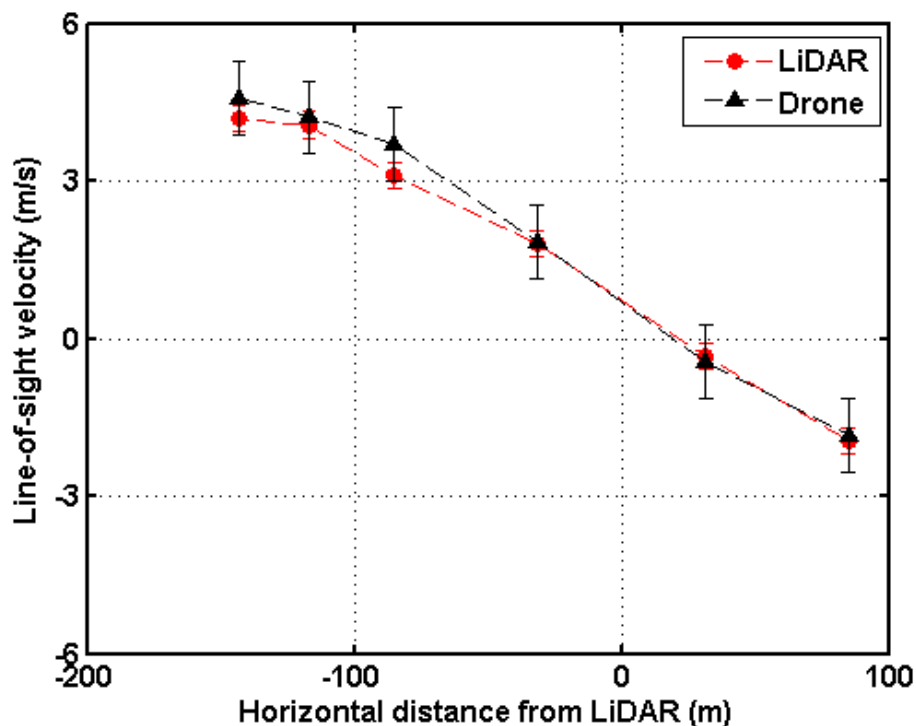


Figure 3.4: Comparison of the line-of-sight wind velocity measured with the 3D scanning LiDAR to simultaneous measurements using ETH’s instrumented drone.

3.4 Opto-mechanical platform versus strain gauge

Figure 3.5 compares the PSD of sideways tower deflections measured simultaneously with the opto-mechanical platform and with strain gauges. The opto-mechanical measurements are at the head of the tower of Turbine 11 in Juvent wind farm, described in section 2.2.1. The strain gauge measurements are at the root of Turbine 10 in Juvent wind farm; more complete details of the strain gauge measurements can be found in [81]. As seen in Fig. 2.5 Turbines 10 and 11 are adjacent to each other. The PSDs are normalised relative to their respective maximum amplitudes. Overall excellent agreement is observed between the two independent measurement systems. Both measurement systems have a maximum amplitude at 0.01Hz, and have the same decay in the slope at lower frequencies. Furthermore, as can be seen in the close-up inset in Fig. 3.5, both systems capture the rotor frequency and tower natural frequency of 0.25Hz and 0.27Hz, respectively.

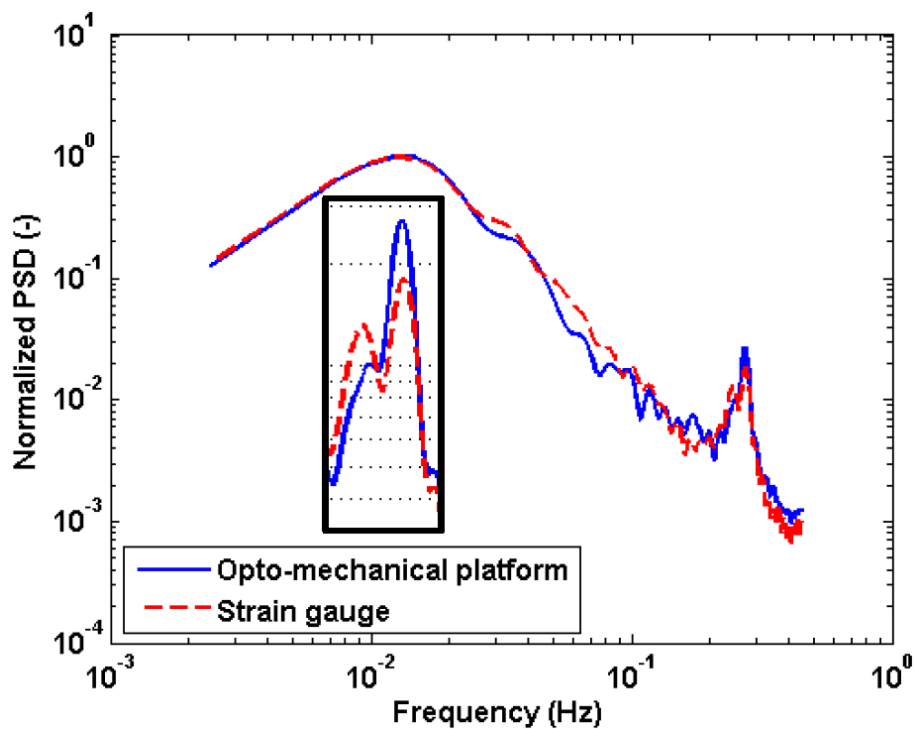


Figure 3.5: Comparison of the PSD of sideways tower deflections measured with the opto-mechanical platform and with strain gauges. The PSDs are normalised with the respective maximum amplitudes. The close-up inset compares the PSDs over the range 0.23Hz-0.30Hz.

Chapter 4

Wind turbine operation in non-uniform flow

The results of three experiments for flow field measurements are presented in this chapter. The first two experiments are related to the wind-farm-scale flow field at AltenbruchII (Section 2.2.3) and EOSH (Section 2.2.2) wind farms and the third experiment is related to the wind-turbine-scale flow field at Turbine 4 of the EOSH wind farm. Next, the impact of wind flow field on power generation of wind turbines is discussed. Additionally, the recovery of velocity deficit in single-wake and double-wakes are investigated. Finally, using the experimental results, the predictions of the wind flow field with the CFD tool, MULTI3, are assessed. The chapter ends with the key findings.

4.1 Wind flow field in scale of wind farm

The contour of horizontal wind speed at the hub height of 9 wind turbines of AltenbruchII wind farm (Section 2.2.3) are shown in Fig. 4.1. The experiment procedure is discussed in Section 2.3.3. Wind direction is 150° shown with the blue line. Velocity deficits of up to 52% are observed downstream of wind turbines of the wind farm. The wake propagation direction, shown with the dash-dot lines, downstream of Vestas V80 turbines is up to 7° different as compared to the adjacent Vestas V90 turbines. The vertical profile of wind direction, Fig. 4.2, accounts for the observed misalignment of wakes.

As shown in Fig. 4.2, the horizontal wind direction shows wind veer of up to 13° per 100m change in height at the heights below 200m AGL. The hub height of Vestas V80 turbines is 45m smaller as compared to the hub height of Vestas V90 turbines. The observed wind veer yields a wind direction change of 5.8° over the 45m hub-height difference of the two turbines, which is in the same order as the observed misalignment of the wakes of the two turbines.

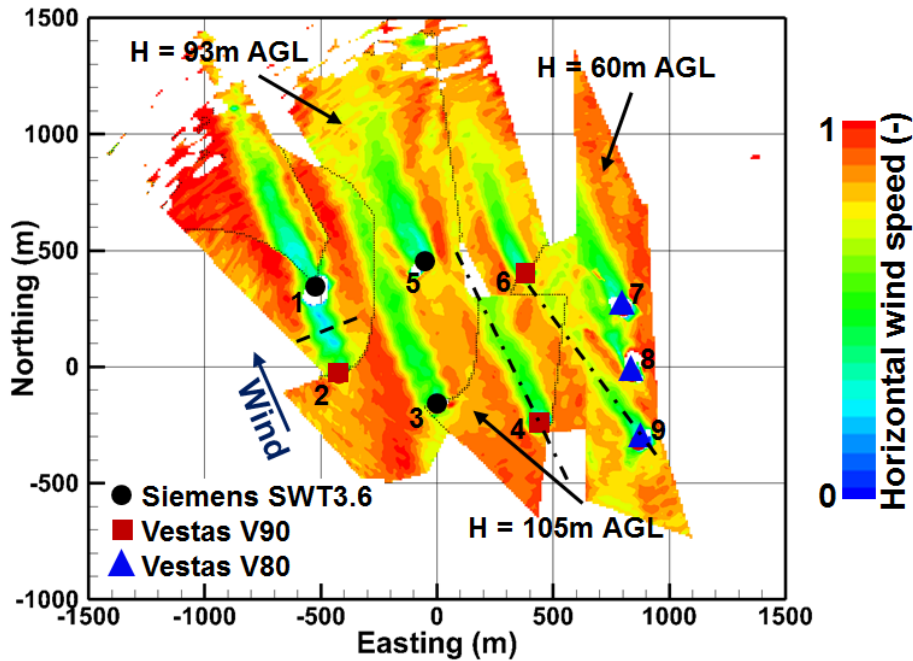


Figure 4.1: The horizontal wind speed measured in the hub-height plane of wind turbines at AltenbruchII wind farm (Section 2.2.3). Wind direction is shown with the blue line. Number of each turbine within the wind farm is shown next to the turbine symbols. Dash-dot line shows the wake centerline downstream of Turbine 4 and Turbine 9. Velocity distribution over dashed line is shown in Fig. 4.5.

The assessment of velocity triangles at 75% span showed that the observed wind veer causes the incidence angles on the blades to fluctuate with an amplitude of 0.5° over one complete rotor rotation. Since the geometric specifications of the blades are not publicly available, the blade data of the NREL 5MW wind turbine, whose blade specifications are openly accessible, are used for this assessment. As flow separation over blade aerofoils occur typically above incidence angles of 12° , the incidence angle fluctuations with 0.5° amplitude should have negligible impact on the aerodynamic performance of blades.

The wind flow field in the scale of wind farm is also measured at EOSH wind farm (Section 2.2.2). Figure 4.3 shows the contour of wind speed at the hub height of 14 turbines of the wind farm, which are shown with black circles. The hub height of Turbines 1 – 9 is 100m AGL and the hub height of Turbines 10 – 14 is 78m AGL. The turbines shown with black triangles are from another wind farm and their specifications are not accessible. The general wind direction is 100° . The wind farm includes two clusters of turbines at the south-western corner and at the north-eastern corner. Several wakes from wind turbines in each cluster cause a complex flow field in the wind farm. The wake flow field downstream of Turbines 2, 3 and 14 is further investigated in Section 4.4.1.

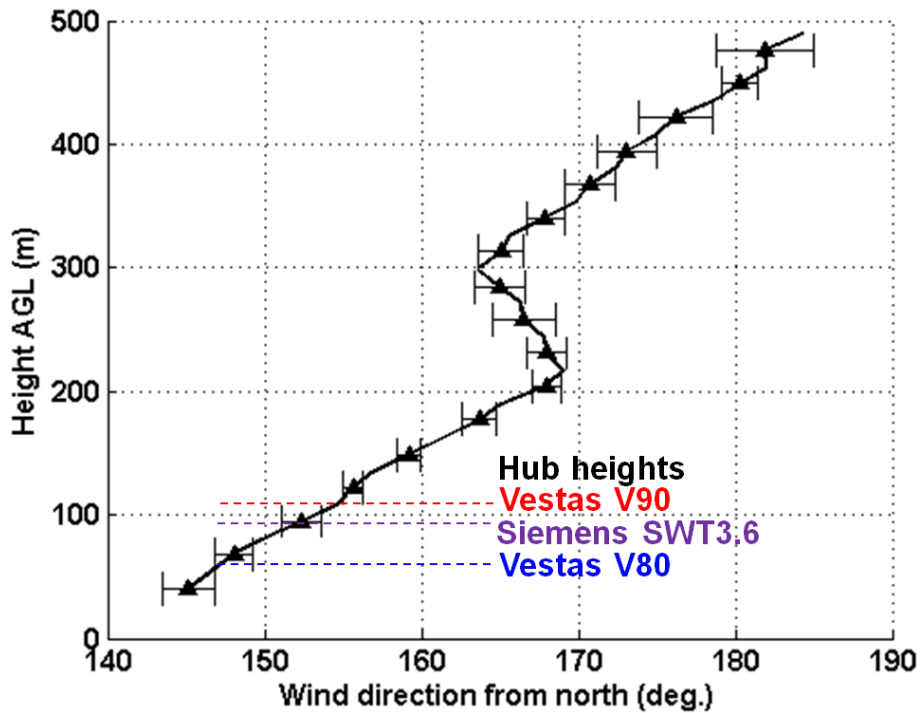


Figure 4.2: Vertical profile of wind direction during measurements of Fig. 4.1. The hub height of various turbines of the wind farm are shown with the dashed lines.

4.2 Wind flow field on the scale of a wind turbine

The time-averaged 3D vector of wind speed is measured within the volume around Turbine 4 that is shown in Fig. 4.4. Turbine 4 is located at EOSH wind farm (Section 2.2.2). The measurements are made within a volume whose horizontal planform is shown by the dashed line and whose height extends from 50m AGL to 150m AGL. The LOS wind speed component is measured from three different positions – position 1, position 2 and position 3 – and the averaged 3D vector of wind speed is then derived from the three different measurements. Further details of this measurement scheme are provided in Section 2.3.2. The wind flow field within the volume is presented in Section 4.4.2.

4.3 Power generation in wake

The power generation of 9 wind turbines at AltenbruchII wind farm is shown in Fig. 4.5a. The power generation levels are taken from the SCADA data of the turbines during the period that measurements of Fig. 4.1 are made. The generated power by Turbine 3, which operates in the undisturbed wind, is used to normalize the power generation of wind turbines of the same type, that is Turbine 1 and 5; similarly the generated power of

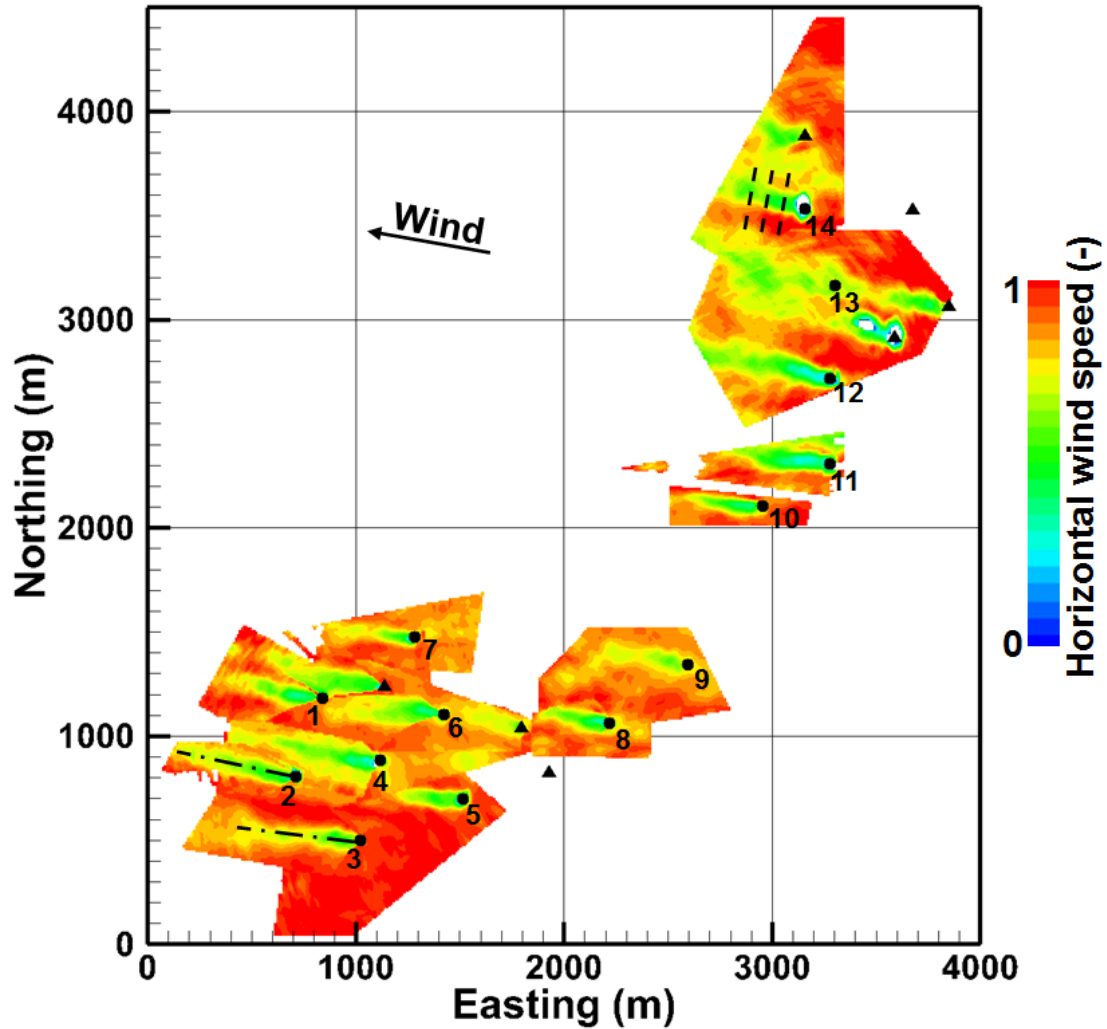


Figure 4.3: Horizontal wind speed measured in the hub-height plane of wind turbines at EOSH wind farm (Section 2.2.2). Wind direction is shown with the black line. Turbines of the wind farm are shown with black circles. The turbines shown with black triangles are from another wind farm. The number of each turbine within the wind farm is shown next to the turbine symbols. Streamwise wake recovery over dash-dot lines are shown in Fig. 4.6. Spanwise distribution of wake deficit over dashed lines is shown in Fig. 4.7.

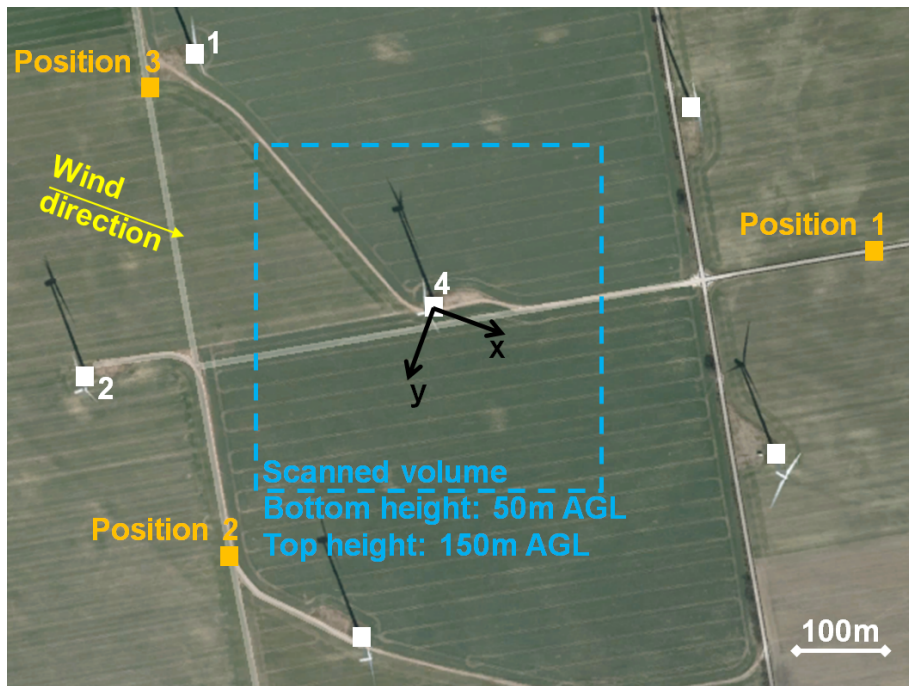


Figure 4.4: Plan view of the measurement volume within which measurements of time-averaged wind vector are made. Measurements of the LOS wind speed component are made from position 1, position 2 and position 3. Turbines are shown with white squares.

Turbine 4 is used to normalize the generated power of Turbine 2 and 6 and the generated power of Turbine 9 is used to normalize the generated power of Turbine 7 and 8. 39% of power deficit is observed for Turbine 1. As observed in Fig. 4.1, operation in the wake of Turbine 2 can account for the observed power deficit of Turbine 1. Turbines 5 and 6 have over-performance of 10%. The higher wind speed in the periphery of the wakes from upstream turbines can account for the over-performance of these turbines. The high-velocity region in the periphery of the wakes is caused by the radial expansion of stream tubes which enclose the wake of the turbines.

Turbine 2 shows a 6% power deficit despite operating in the undisturbed wind. The reason is further investigated by assessing the lateral distribution of velocity deficit along black dashed lines in Fig. 4.1, which is at 2D downstream of Turbine 2. As observed in Fig. 4.5b, the center of wake deficit is laterally offset by $0.3D$ from the rotor center. As discussed in [82,83], the lateral offset of the wake center can be an indicator of misalignment between rotor yaw angle and wind direction. Hence, rotor yaw misalignment is a potential reason for the observed 6% power deficit of Turbine 2.

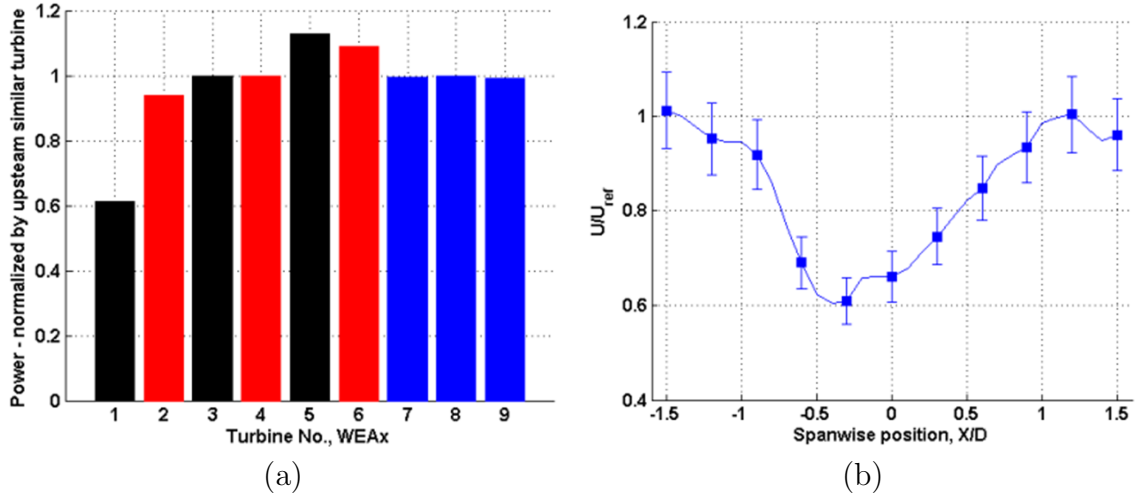


Figure 4.5: (a) power generation of wind turbines during measurements shown in Fig. 4.1. Power generation levels are extracted from SCADA of the turbines, and (b) spanwise distribution of velocity deficit downstream of Turbine 2 in Fig. 4.1.

4.4 Impact of operating conditions on wake propagation

4.4.1 Wake recovery in double-wake

Figure 4.6 shows the wake recovery along the dash-dot lines in Fig. 4.3, which are downstream of Turbine 2 (double-wake) and Turbine 3 (single-wake). The wake flow field downstream of Turbine 2 is influenced by the wake of Turbine 4; hence the term double-wake is used for this turbine. The recovery in the wake is driven by the shear stress and turbulent mixing between the low-velocity region inside the wake and the peripheral high-velocity region outside the wake. The wake flow field in the single-wake, downstream of Turbine 3, is exposed to high-velocity region on both sides, however in the double-wake, downstream of Turbine 2, the peripheral velocity on the northern side is lower due to the wake from the upstream turbine. This results in a higher recovery rate downstream of the Turbine 3, single-wake in Fig. 4.6, as compared to the double-wake.

Figure 4.6 shows two different regimes of recovery occurring in the single-wake; a fast recovery rate in the near-wake, between $1.3D$ to $3D$ downstream position, and a slower recovery rate in the far-wake, from $3D$ position to $7D$ position. Up to 72% of velocity recovery occurs in the near-wake. Figure 4.6 also shows a model of flow recovery in the wake which is resulted from independent measurements downstream of full-scale wind turbines using a drone, [1]. This model shows that the normalized velocity in the wake recovers from 40% at $1D$ downstream position, to 70% at the $3D$ downstream position. The fast recovery in the near-wake correlates very well in the drone and LiDAR measurements of

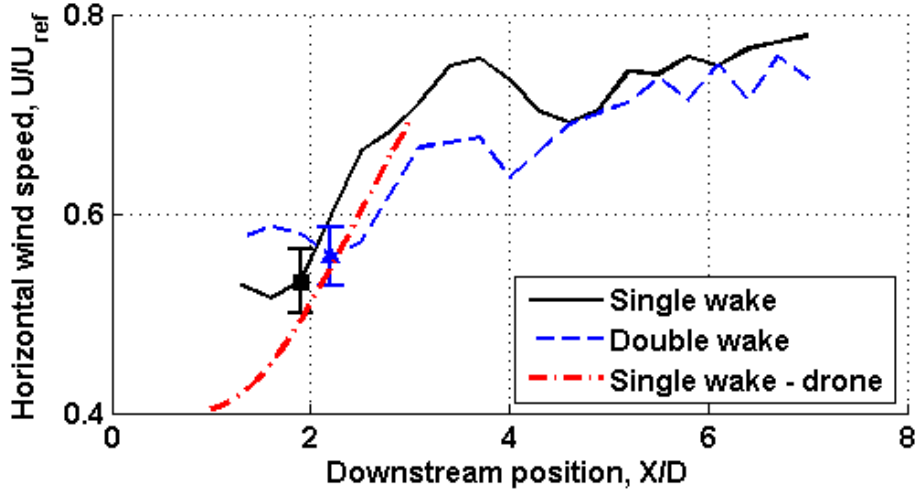


Figure 4.6: Velocity recovery in the wake of Turbine 3 (single-wake) and Turbine 2 (double-wake) of Fig. 4.3. Dash-dot line shows the model resulted from full-scale measurements [1] with drone.

the single-wake. Unlike the single-wake, the recovery in the double-wake is monotonous in all measured axial positions, with a rate which is smaller than the fast recovery rate in the near-wake region ($1D - 3D$) of the single-wake.

The impact of the double-wake on the evolution of the wake is also investigated along the dashed lines in Fig. 4.3, which are downstream of Turbine 14. Figure 4.7 shows the spanwise evolution of velocity deficit in the wake of this turbine. The velocity deficits are at $1.5D$, $2.5D$ and $3.5D$ downstream positions, shown with the dashed lines in Fig. 4.3. The positive and negative Y/D ranges in Fig. 4.7 are respectively related to the northern and southern periphery of the wake region of Turbine 14. As observed in Fig. 4.7, wind flow on the right side of the wake region from Turbine 14 is disturbed due to the wake from an upstream turbine. This disturbance causes the low-velocity region on the right side of the wake downstream of Turbine 14, as compared to the left side. The high velocity on the left side of the wake causes the higher lateral velocity gradients and hence results in a faster recovery on the left side, as compared to the right side. Such asymmetric wake recovery causes the center of the wake to deflect to the right side in more downstream positions; that is the lateral position of wake's centerline is respectively at $0.2D$, $0.4D$ and $0.7D$ for downstream positions of $1.5D$, $2.5D$ and $3.5D$.

4.4.2 Wake flow in non-uniform inflow

Figure 4.8 shows the three components of the wind vector, that is axial wind speed in Fig. 4.8a, lateral wind speed in Fig. 4.8b and vertical wind speed in Fig. 4.8c, in streamwise

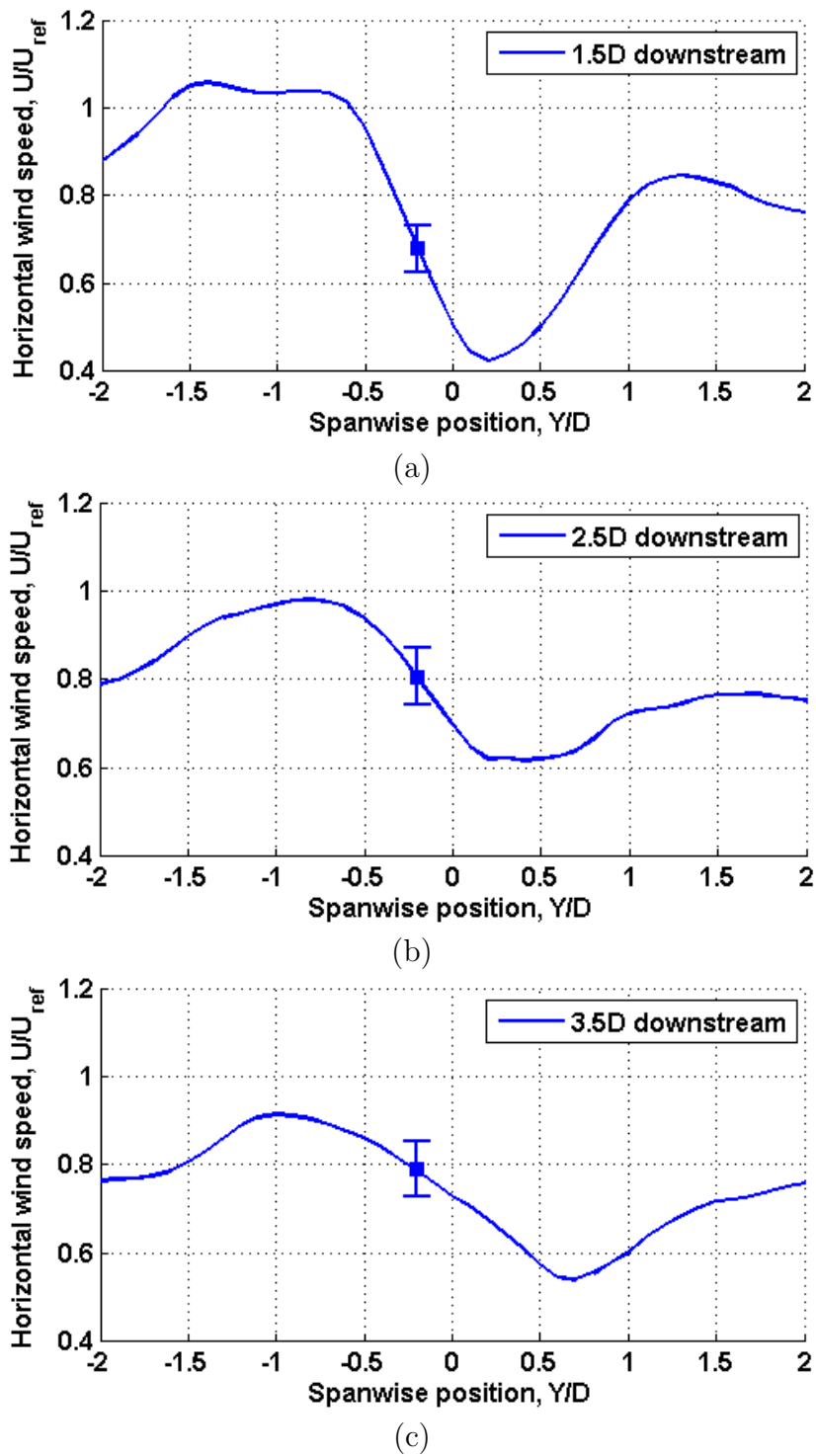


Figure 4.7: Spanwise distribution of velocity deficit downstream of Turbine 14 of Fig. 4.3.

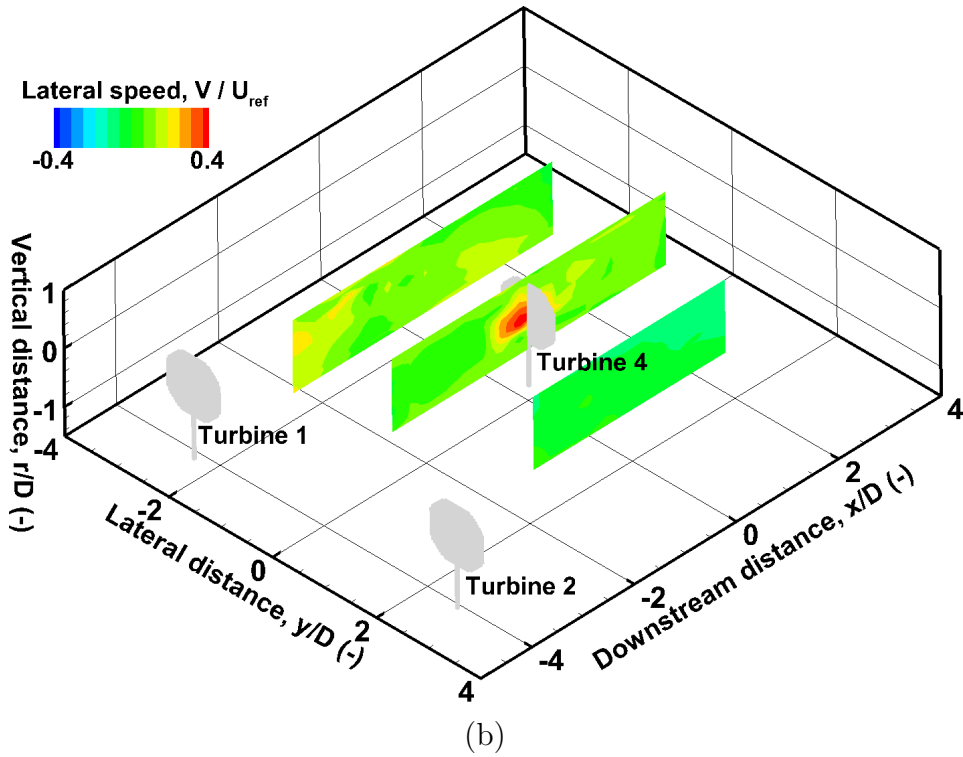
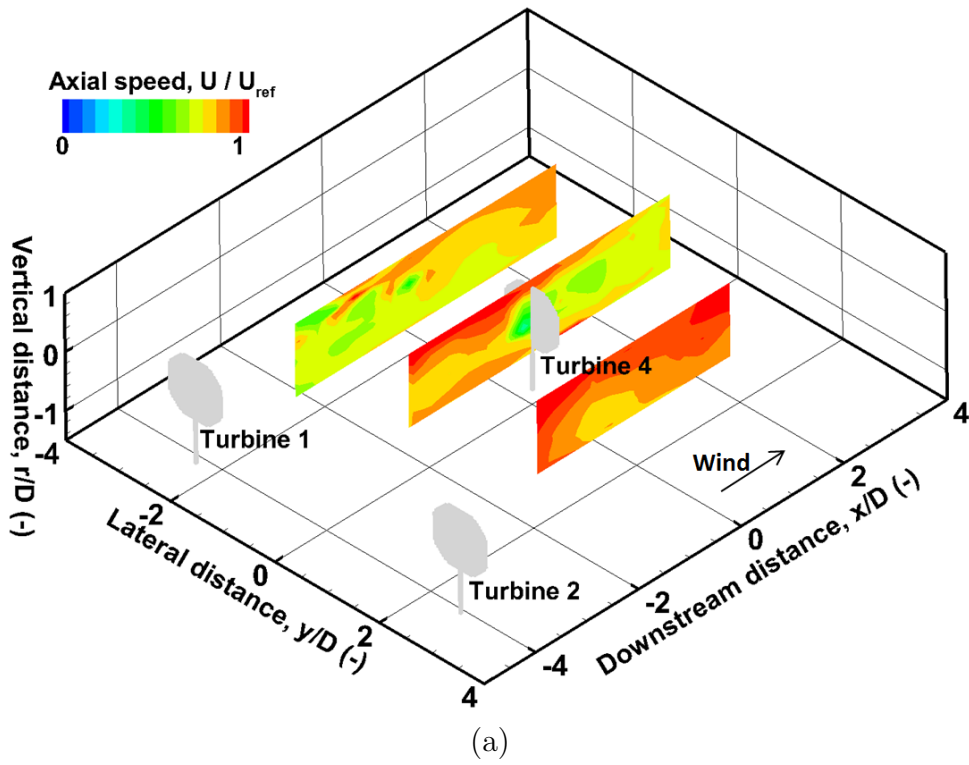
vertical planes at $Y = \pm 1.8D$ and $0D$; Turbine 4 is located at $X/D = 0$, $Y/D = 0$ as shown in Fig. 4.4. The streamwise evolution of the axial wind speed in a vertical plane through Turbine 4 is shown in the central plane in Fig. 4.8a. It is observed that over the vertical extent of the rotor due to the wakes of Turbine 1, the incoming wind varies up to 33% of the undisturbed wind speed. Velocity deficits of up to 45% are observed in the wake of Turbine 4. Downstream of Turbine 1, the velocity deficit decreases from 31% at $X/D = -3.0$ to 10% at $X/D = 2$. Traces of the velocity deficit from Turbine 2 are observed in the streamwise plane at $Y/D = 1.8$.

The significant observation in the contour of lateral wind speed, Fig. 4.8b, is the high values measured at rotor plane of Turbine 4. The lateral migration at the rotor plane of Turbine 4 is attributed to the expansion of the wake region downstream of Turbine 1. Apart from the observed high values at the rotor plane of Turbine 4, the lateral wind speed is negligible in the rest of the measured domain. The vertical wind speeds are shown in Fig. 4.8c. A strong upwards vertical wind speed is observed up to $0.5D$ downstream of Turbine 4. The vertical wind speed decreases as the wake evolves. The vertical wind speed is associated with a vertical migration of the wake flow. This vertical migration is a result of the sheared inflow upstream of the turbine. As a consequence of this shear, at different rotational positions of the blade, there are different incidence angles at a given blade section. Furthermore even though modern wind turbines are equipped with collective or individual blade pitch control systems, the variation of incidence across the blade span will vary with blade's rotational position. Thus, the non-uniform power extraction across the vertical extent of the rotor results in a non-uniform pressure distribution downstream of the rotor. The absence of a radial equilibrium due to the non-uniform pressure distribution results in the subsequent vertical migration of the flow.

Figure 4.9 shows the vertical profiles of wind speed $1D$ upstream and downstream of Turbine 4. In the upstream profile, the impact of the wakes from the upstream turbines is evident, as the wind speed varies non-monotonically with height. The downstream profile shows the characteristics of a wake profile, with a maximum deficit in wind speed close to the hub height. A comparison of the two profiles shows the non-uniform work extraction over the vertical extent of the rotor. The work extraction is evidently larger in the upper half of the rotor swept area, and lower in the lower half.

4.5 Full-scale experiments versus CFD and Sub-scale model

The wind flow field at AltenbruchII wind farm (Section 2.2.3) is simulated using the CFD tool MULTI3 (Section 2.5.1). The simulation is performed with the same boundary conditions as during the wind-farm-scale measurements, described in Section 4.1. Figure 4.10 shows the comparison between the measurement, Fig. 4.10a, and simulations, Fig.



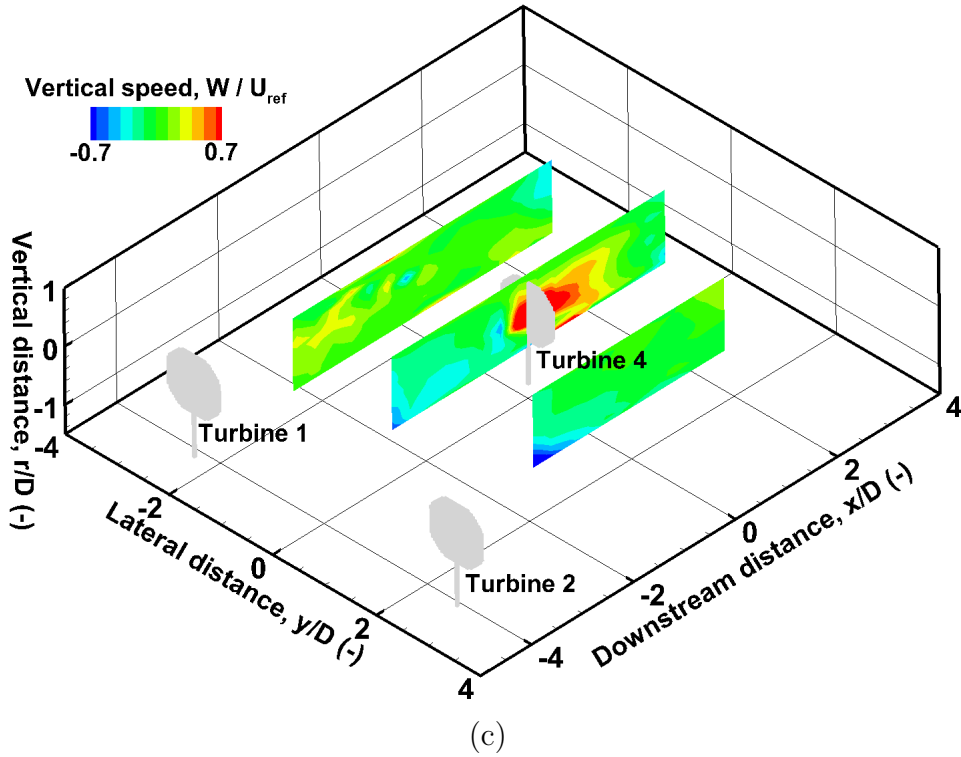


Figure 4.8: Time-averaged measurements of the wind vector in the volume shown in Fig. 4.4. Results are shown in three vertical planes at $Y/D = -1.8$ (downstream of Turbine 1), $Y/D = 0$ (upstream and downstream of Turbine 4) and $Y/D = 1.8$ (downstream of Turbine 2), (a) axial wind speed, (b) lateral wind speed and (c) vertical wind speed.

4.10b. The qualitative comparison of measurement and simulations is satisfactory. The simulated wake deficit and boundaries are generally in the same range as those of the the measurement. The wake misalignment due to the observed wind veer, Fig. 4.2, is not considered in simulations. The streamwise extent of the wake downstream of Turbine 3 is longer in the measurement, compared to the simulations. Slower velocity recovery due to the wake from Turbine 5 and upward migration of the wind flow field to the higher plane, at hub height of Turbine 2 can be the possible reasons for the observed longer wake extent downstream of Turbine 3, as compared to the simulations.

The velocity distribution along a streamwise line upstream and downstream of each turbine is extracted and normalized with the upstream wind speed. Table 4.1 shows the rms difference of the predictions from experimental results. The agreement upstream of turbines is good with an average rms difference of 6%. The differences in the wake region downstream of turbines are larger with an average rms of 14%. The streamwise distribution of horizontal wind speed at Turbine 1 and 5 are shown in Fig. 4.11.

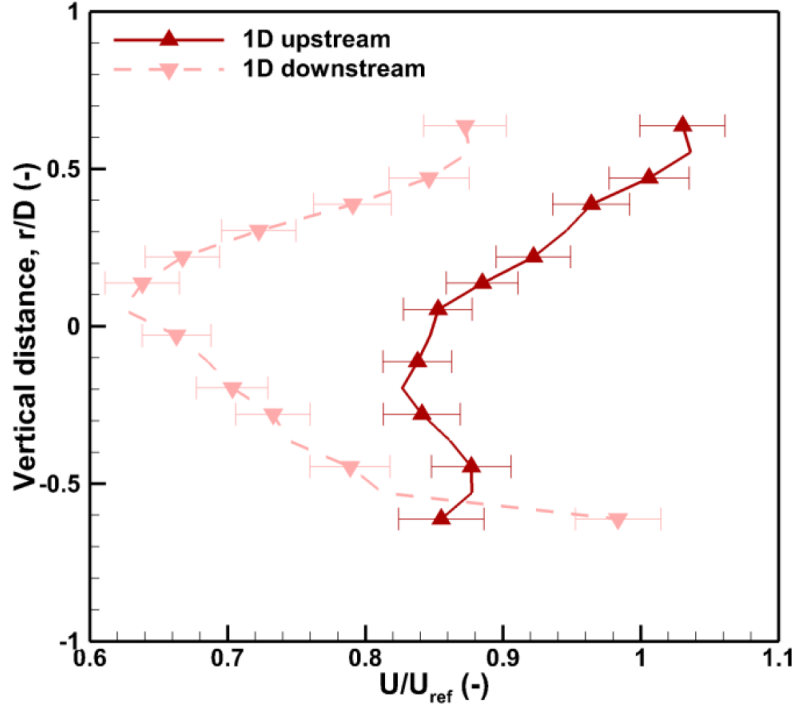
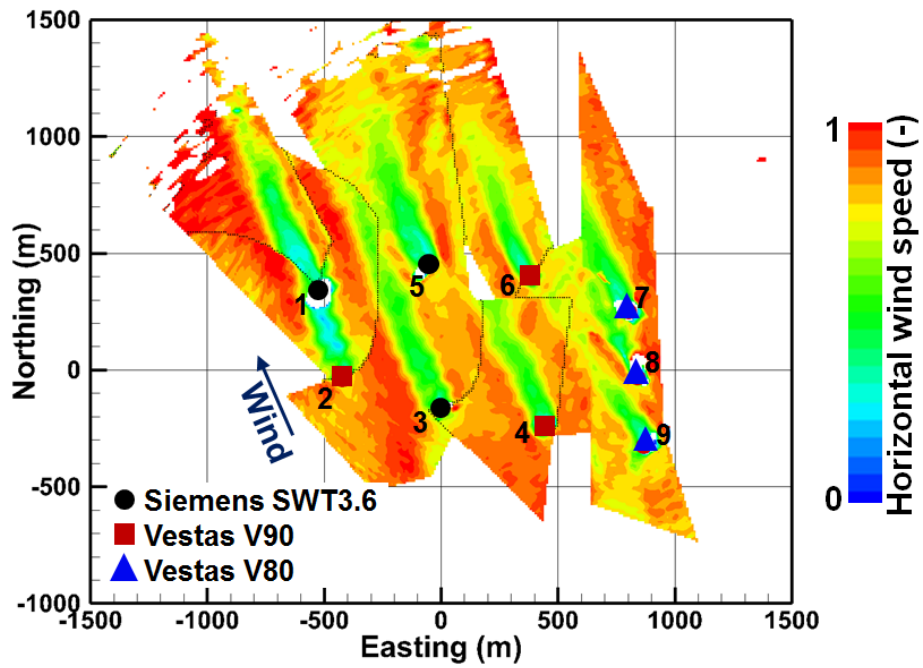


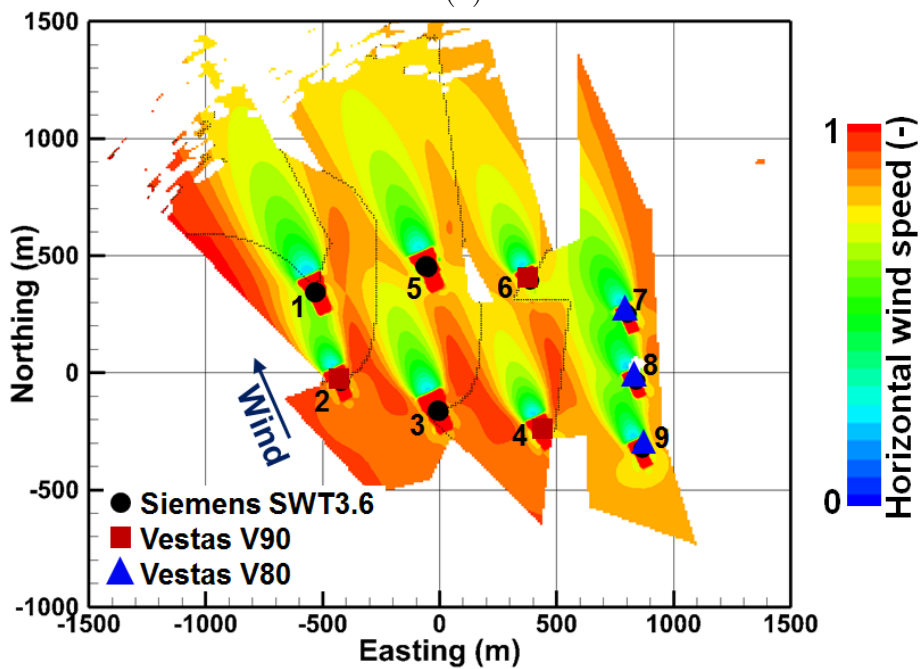
Figure 4.9: Vertical profiles of wind speed at $1D$ upstream and downstream of Turbine 4.

Table 4.1: The rms difference of measured and predicted horizontal wind speeds. The rms differences are related to the distribution of horizontal wind speed in the range of $5D - 1D$ upstream and the range of $1D - 7D$ downstream of the turbines of Fig. 4.10.

Turbine No.	1	2	3	4	5	6	7	8	9
Upstream (%)	27	3	5	2	3	6	4	5	4
Downstream (%)	18	18	14	13	7	7	13	14	17



(a)



(b)

Figure 4.10: Horizontal wind speed at AltenbruchII wind farm (Section 2.2.3). Wind direction is shown with the blue line. (a) measurements, and (b) simulations with CFD tool MULTI3.

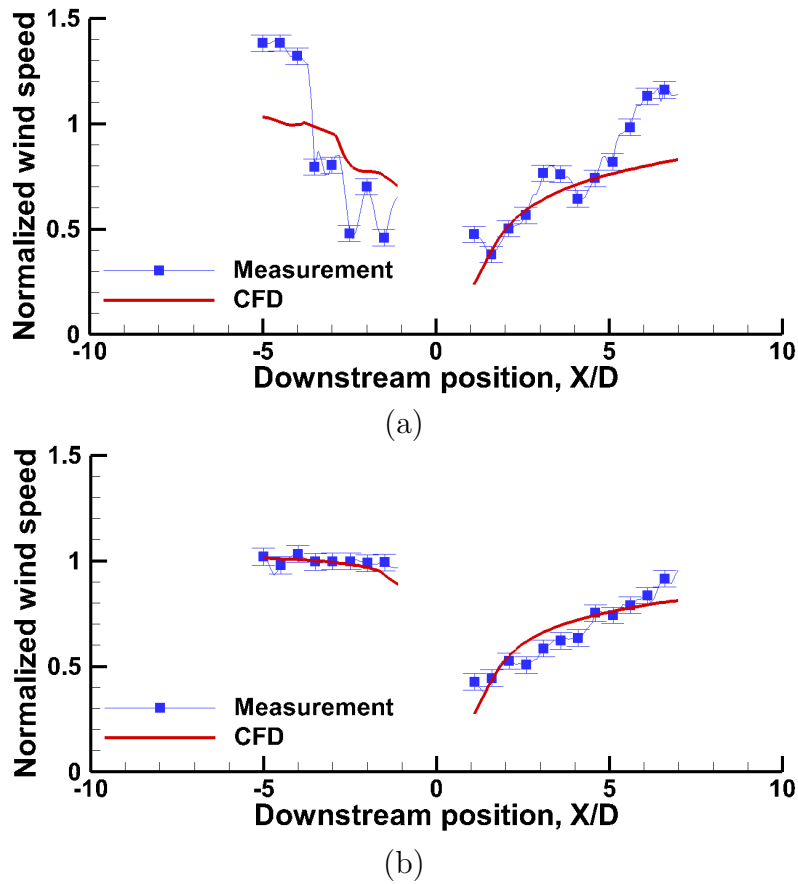


Figure 4.11: Streamwise distribution of horizontal wind speed. (a) Turbine 1, and (b) Turbine 5. The turbines are shown in Fig. 4.10.

As seen in Table 4.1, the difference between measurements and simulations are highest at Turbine 1 and lowest at Turbine 5. As observed in Fig. 4.11a, the upstream disturbances due to the wake from Turbine 2 are not well captured in the simulations, which accounts for the high differences at this turbine. Downstream of Turbine 1, Fig. 4.11a, the agreement is satisfactory in the near-wake. In the far-wake faster recovery is observed in the measurements. Higher lateral velocity gradients due to higher velocity at the western periphery of the wake and the narrower wake region observed in the measurements can account for the faster recovery rate observed in measurements. Fig. 4.11b shows the comparisons at Turbine 5. It is observed that experiment and simulations have satisfactory agreement over the shown axial range.

Figure 4.12 shows the spanwise distribution of the wake deficit compared between experimental results and predictions of the ETH wake model. The wake deficit is measured at Turbine 2 at the $1D$ downstream position. The ETH wake model is a semi-empirical,

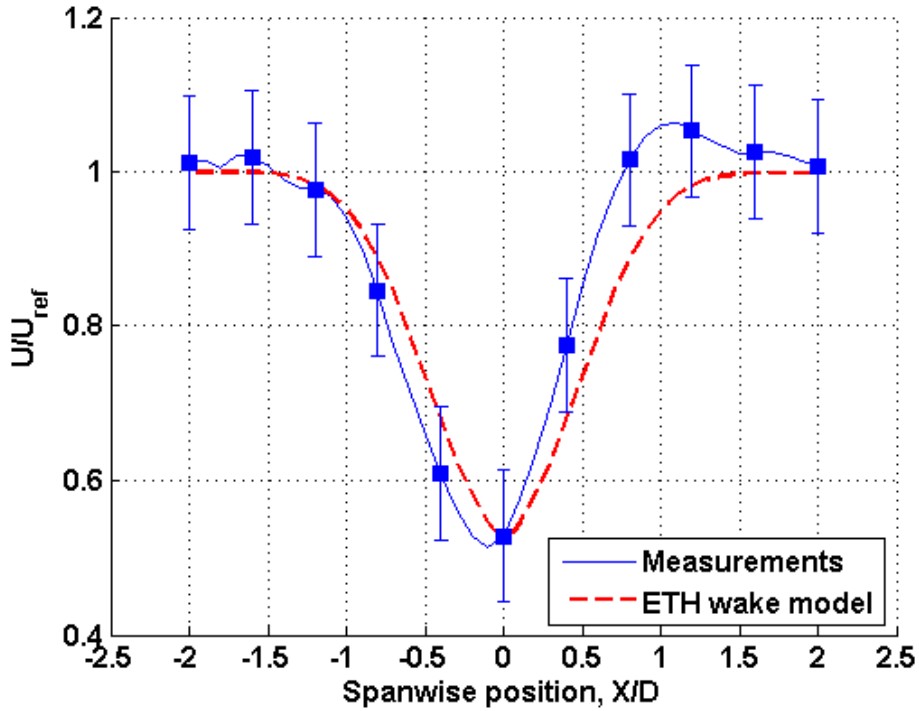


Figure 4.12: Spanwise distribution of velocity deficit in the wake of Turbine 2 of Fig. 4.1.

axisymmetric wake model based on experimental observations of the mixing layer that develops between the wake and the ambient flow. Thus, the model uses free shear flow theory to detail the evolution of the axial wind speed in the wake [84]. Comparison in Fig. 4.12 shows that the model can very well predict the velocity distribution with 6% rms difference. It is observed that the measured wake is laterally offset from the rotor centerline. The potential reason for this offset is further discussed in Section 4.3.

Simulations of wind flow in the same wind farm as that of the experiment shown in Fig. 4.8 is performed using the CFD tool MULTI3 (Section 2.5.1). Figure 4.13 shows the measured (Fig. 4.13a) and predicted (Fig. 4.13b) axial wind speed in streamwise vertical planes at $Y = \pm 1.8D$ and $0D$; the Turbine 4 is located at $X/D = 0, Y/D = 0$. In comparison to the measurements, the wakes from Turbine 1 and Turbine 2 are captured relatively well in planes $Y = \pm 1.8D$ of the simulation.

Figure 4.14a shows the streamwise evolution of the hub height wind speed in the wake of Turbine 1; the location of comparison is shown by the dashed line in Fig. 4.13a. It is seen that overall the quantitative agreement is excellent. Both the measurement and CFD show a maximum deficit of wind speed up to 40% at $1.5D$ downstream, which reduces to 20% at $7D$ downstream. The rms difference between measurement and CFD is 3% in this case. However in the plane $Y/D = 0$ the predictions differ more compared to

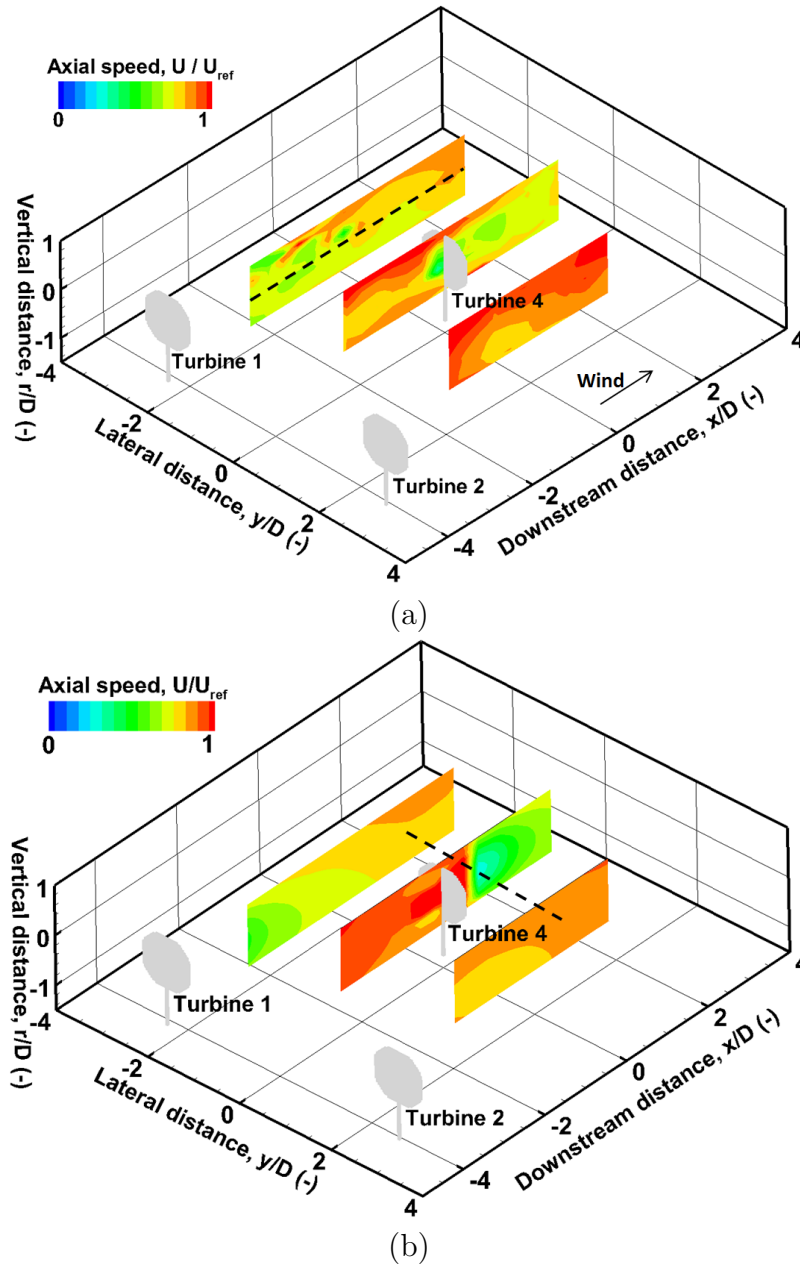


Figure 4.13: Comparison of time-averaged measurements and CFD prediction of axial wind speed. The results are shown in three vertical planes at $Y/D = -1.8$ (downstream of Turbine 1), $Y/D = 0$ (upstream and downstream of Turbine 4) and $Y/D = 1.8$ (downstream of Turbine 2), (a) Measurements, and (b) CFD predictions. CFD and measurements are compared along the black dashed lines in Fig. 4.14.

the experiments. The wake downstream of Turbine 4 is termed a double-wake since it is comprised of the wakes from both Turbine 4 and Turbine 1. As observed in Fig. 4.13b, this double-wake is not captured well in CFD simulations.

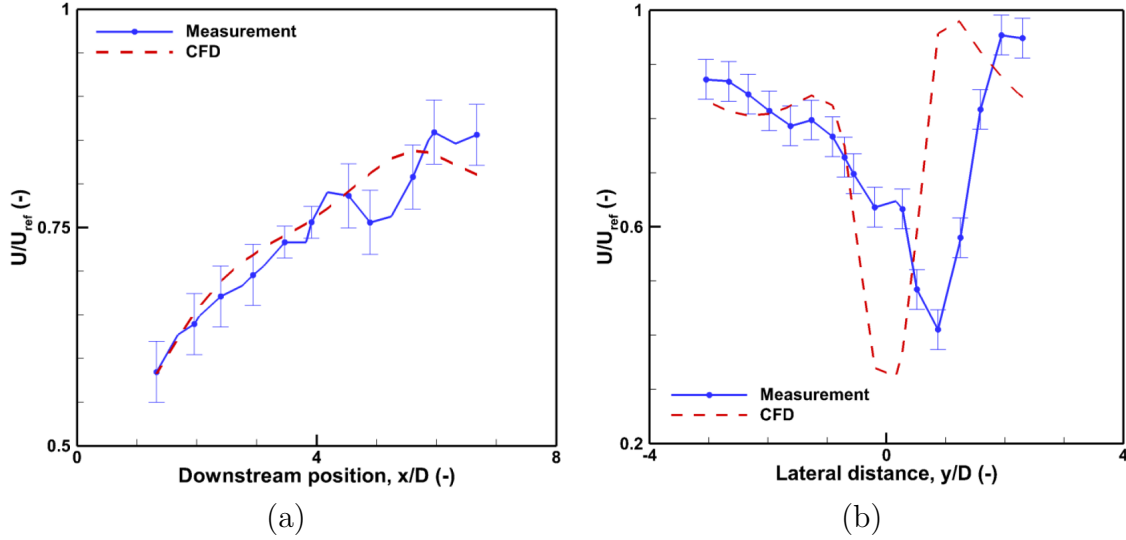


Figure 4.14: (a) Streamwise evolution of the hub height wind speed in the wake of Turbine 1 and (b) Spanwise (lateral) distribution of the axial wind speed at hub height at a distance of $1D$ downstream of Turbine 4.

The spanwise variation of the axial wind speed at hub height, $1D$ downstream of Turbine 4 is shown in Fig. 4.14b; this also includes the double-wake of Turbine 4. The position of the comparison is indicated by the dashed line in Fig. 4.13b. Outside the wake of Turbine 4, $Y/D < -1$, the predictions have a 4% rms difference compared to the measurements. Within the wake the maximum deficit is 65% compared to 60% in the measurements. Furthermore, it can be seen that lateral positions of the maximum deficit differ; the lateral position is $Y/D = 0$ for the prediction compared to $Y/D = 1$ for the experiment.

4.6 Concluding remarks

The horizontal extent of wakes downstream of wind turbines is modified due to the non-uniform distribution of wind speed on the lateral sides of the wake. The wake centerline was observed to be laterally offset by up to $0.7D$ at the $3D$ downstream position due to flow perturbations on one side of the wake. A non-uniform peripheral velocity distribution around the wake also modifies the velocity recovery rate. Velocity recovery in the wake of a turbine operating in the undisturbed flow (single-wake) shows a fast recovery occurring

in the near-wake, from $1D$ to $3D$ downstream positions, followed by a slow recovery rate in the far-wake, that is downstream of the $3D$ position. Up to 72% of velocity recovery occurs in the near-wake. The fast recovery rate in the near-wake is not observed in the wake of the turbine which was laterally exposed to the wake from upstream turbines (double-wake). Results in the single-wake are in good agreement with findings of previous full-scale measurements with an instrumented drone.

Vertical migration of the flow is observed in the wake of a turbine operating in the disturbed wind. The non-uniform velocity distribution results in non-uniform work extraction over rotor swept area. Lack of radial equilibrium due to the non-uniform work extraction can account for the observed vertical migration.

Predictions of CFD are in satisfactory agreement with experimental observations. Comparisons of the measured wind-farm-scale flow field with CFD predictions yield 6% rms difference upstream of turbines and 14% rms difference downstream of turbines. Excellent agreement with 3% rms difference between CFD and experiment was observed in the wake of a wind turbine operating in the undisturbed wind. Predictions in the wake of the wind turbine operating in the disturbed flow differ more compared to experiments.

Chapter 5

Forests and wind energy

Installed wind capacity has increased by seven folds in the past decade (59GW in 2005 to 433GW in 2015) [85]. 97% of installed capacity is onshore. In countries such as Germany and Denmark, the shortage of available land is one of the main obstacles against further development of wind energy. A recent study showed that if the set-back distance from forest edge decreases from 500m to 50m, the land area available for installation of wind turbines doubles [86]. In some countries such as Japan, where 67% of land area is covered with forests [87], the set-back distance from forests is suspected to have higher impact on the land area available for the installation of wind turbines. Nevertheless, the impact of forests on the downstream wind is not thoroughly known. Higher surface roughness of canopies, as compared to unforested fetch, accounts for higher drag force and turbulence generation above forests. These effects modify the boundary layer above and downstream of forests, which consequently impacts the performance of downstream turbines. This chapter reports wind flow measurements upstream and downstream of forests as well as load assessments on the tower of wind turbines in forested and unforested fetch. Impact of higher turbulence levels on the generated power will be further examined. Finally, the observations are used to compare and interpret long-term performance of wind farms in forested and unforested areas.

Measurements at a forest edge are made at EOSH wind farm, described in section 2.2.2. The turbines of interest in this measurement set, Turbine 10 and 14, have a hub height of 78m AGL. The close-up view of land cover at the position of these two wind turbines is shown in Fig. 5.1. There is a forest with an average height of 20m AGL west of the wind turbines. The forest of interest, whose downstream wind flow field is detailed in this work, is shown with the yellow dash-dot oval in Fig. 5.1. The measurements in the present work are performed with a wind direction of 245° , which is shown by the dashed yellow lines in Fig. 5.1. In this wind direction, Turbine 10 has a flat unforested fetch up to 1.7km, whereas Turbine 14 faces a forested fetch at 900m upstream. The direction-wise

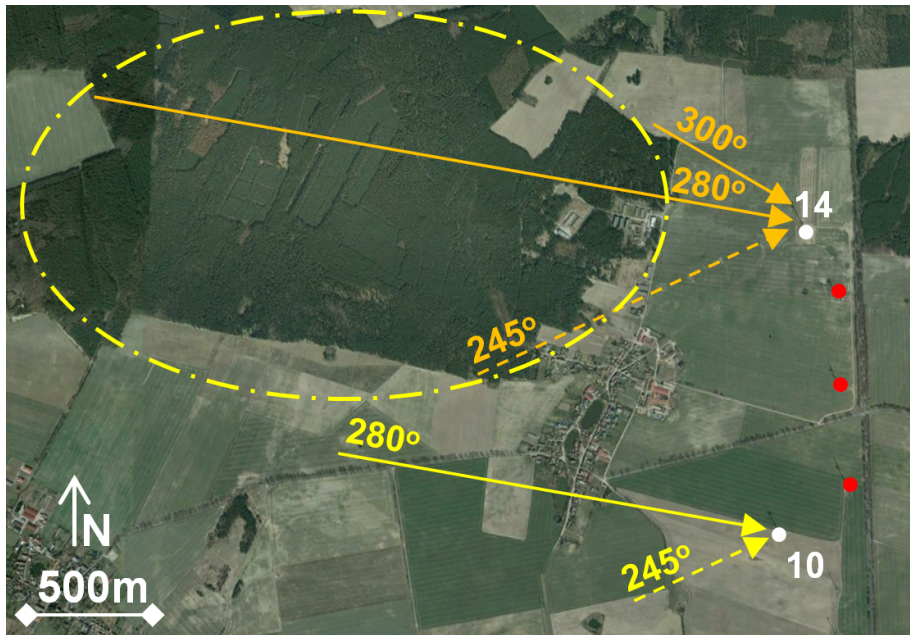


Figure 5.1: Close-up view of the positions of Turbines 10 and 14 relative to the forest edge. The layout of the complete wind farm is shown in Fig. 2.6. The range of wind directions over which the direction-wise AEY are evaluated are shown with the dashed and solid lines.

Annual Energy Yield (AEY) of Turbines 10 and 14 over the range of wind directions of 245° to 300° , as shown by the solid yellow lines in Fig. 5.1, are detailed in Section 5.4.1.

Fig. 5.2 shows the westward view of the landscape upstream of Turbine 14. The directions of 245° , 280° and 300° from north are shown with dash-dot red lines. The incoming wind to Turbine 14 from directions of 245° to 300° traverses the forest. This forest is comprised of Tsuga trees, see insert in Fig. 5.2, with an average height of 20m. The Leaf Area Index (LAI) derived from satellite imagery [88, 89] increases from 4 in winters to 7 in summers at the location of the forest. The present measurements are performed during March where LAI is 5.

The vertical profiles of undisturbed wind speed and direction are shown in Fig. 5.3. The vertical profile of wind speed, Fig. 5.3a, shows that the horizontal wind speed varies from 7m/s at $5H_{forest}$ (100m) AGL to 10m/s at $21H_{forest}$ (420m) AGL. The error bars show the standard deviation of the wind speed over the measurement period of 60 minutes. The measurements show that near the ground there are larger standard deviations, with a standard deviation of 21% at $5H_{forest}$ AGL and 12% at $22H_{forest}$ AGL. Fig. 5.3b shows the vertical profile of wind speed on a semi-log scale; overall, the correlation between the measured profile and the linear fit is good, with a correlation factor of 0.94. This good

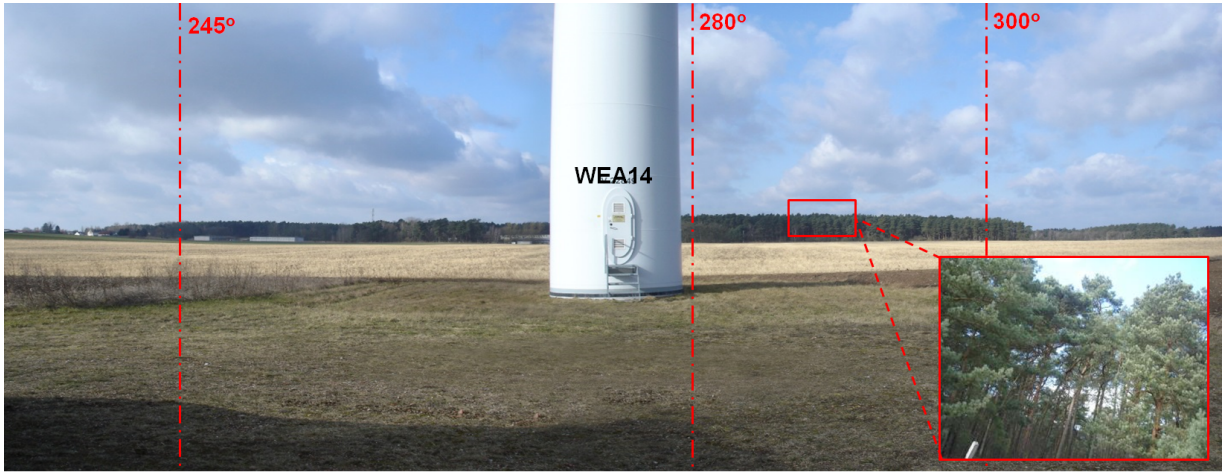


Figure 5.2: Westward landscape at the tower of turbine with forested fetch. The vertical dash-dot red lines correspond to the wind directions shown in Fig. 5.1. The forest of interest is comprised of Tsuga trees.

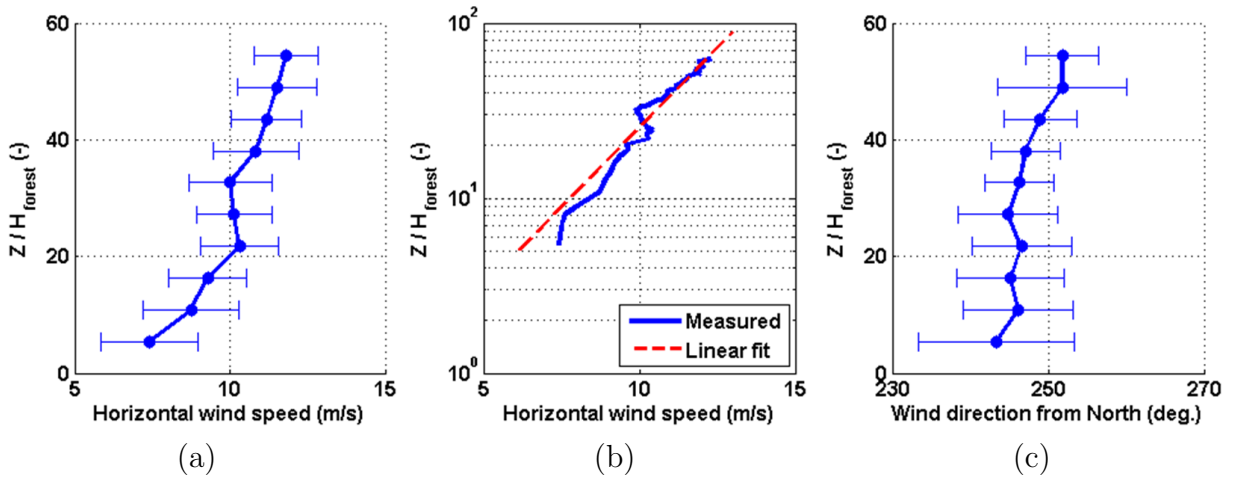


Figure 5.3: Vertical profiles of undisturbed wind speed and direction, (a) wind speed, (b) wind speed on semi-log scale and (c) wind direction.

linear fit is indicative of a neutrally-stable boundary layer [90]. Fig. 5.3c shows the vertical profile of wind direction. The mean wind direction adjacent to the ground is 245° . Below $20H_{forest}$, the mean wind direction varies less than 3° ; above $20H_{forest}$, there is a wind veer of 2° per 100m, which is in the same direction as the Coriolis force. As is observed in the case of the vertical profile of wind speed, the vertical profile of wind direction has larger standard deviations near the ground, compared to further away from the ground.

5.1 Impact of forested fetch on wind turbulence

Fig. 5.4a and Fig. 5.4b show the measured TI upstream of Turbine 10 and Turbine 14, respectively, along the LiDAR beams with elevation angles of 0° , 7.5° , 15° , 22.5° and 30° . The wind direction is from left to right and the turbines are at $X = 45H_{forest}$; and the forest edge is at $X = 0H_{forest}$ in Fig. 5.4b. The measured TI is up to three times higher upstream of Turbine 14 compared to Turbine 10. As Turbine 14 is downstream of the forest, the higher TI is attributed to be an impact of the forested fetch. The impact of the forest extends up to a height of $10H_{forest}$ AGL since the measured TI above $10H_{forest}$ is of the same magnitude upstream of Turbines 10 and 14. The TI upstream of Turbine 10 is in the range of 10% to 15%, which is comparable to the independent measurements in wind farms using a nacelle-mounted probe [67] and kite-mounted probe [68]. On the other hand, the TI is as large as 25% upstream of Turbine 14 due to the presence of the forest. Downstream of the forest, Fig. 5.4b, adjacent to the ground ($elevation = 0^\circ$), TI decreases monotonically from 18% at $X = 5H_{forest}$ to 11% at $X = 40H_{forest}$; at the most downstream distances, the TI is comparable to the 10% TI at the ground as is measured with the unforested fetch, Fig. 5.4a. The vertical extent swept by the rotor of Turbine 14 is shown with the red dashed lines in Fig. 5.4b; it can be seen that the most elevated-turbulence levels downstream of forest cover the same height that is swept by the rotor.

Fig. 5.5 shows the vertical profiles of TI at $X = 10H_{forest}$, $20H_{forest}$ and $30H_{forest}$; these profiles are derived from the measurements shown in Fig. 5.4. As discussed above, the error bars show the expected variation of TI due to turbulence anisotropy; this variation ranges from 3% to 10% of the mean TI. It is evident from the profiles that with the forested fetch the TI is elevated up to two-and-a-half times compared to the TI with the unforested fetch. The variation of TI shows an increase with decreasing height. As the LiDAR beam's elevation angle decreases, the LOS wind speed component has a larger proportion of the horizontal wind speed, which is the primary component of the wind speed. Thus for lower elevation angles, there is a stronger sensitivity in the variation of TI to turbulence anisotropy. This in part explains the larger variations in the TI that are seen closer to the ground in Fig. 5.5.

5.1.1 Impact of turbulence on power fluctuations

Figure 5.6 shows the standard deviation of generated power versus turbulent kinetic energy measured at Martingy wind turbine, section 2.2.4. The data are binned based on the wind speed that is shown by the color code. It is observed that the turbulent kinetic energy increases at higher wind speeds. The dashed line is the linear fit to the measured data in each wind speed bin. It is observed that the power fluctuations increase with turbulence. The equations next to the dashed lines are related to each fitted line. The slope of the fitted

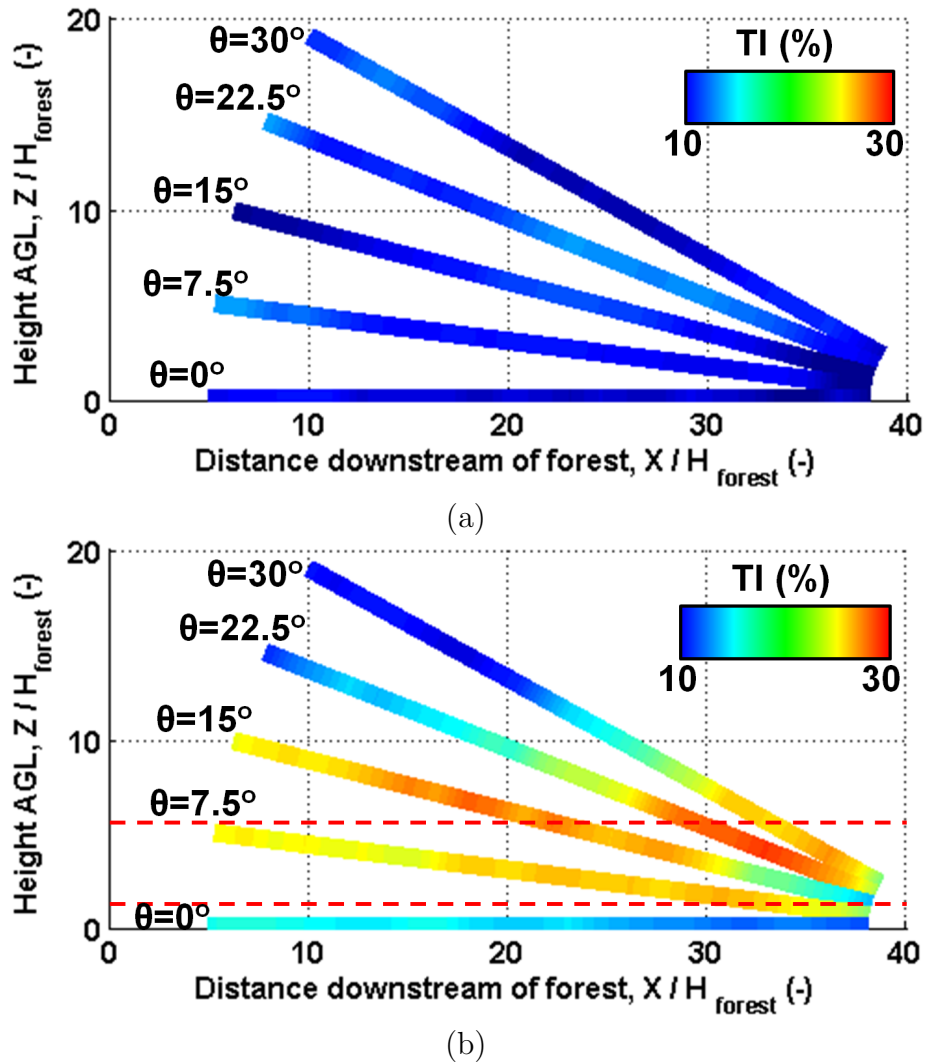


Figure 5.4: TI upstream of turbines along LiDAR beams with elevation angles 0° , 7.5° , 15° , 22.5° and 30° ; the wind direction is from left to right, and the wind turbines are located at a distance of $X = 45H_{forest}$. a) TI upstream of the turbine with flat fetch (Turbine 10 in Fig. 5.1) b) TI upstream of the turbine with forested fetch (Turbine 14 in Fig. 5.1); the forest edge is at $X = 0H_{forest}$. The red dashed lines show the vertical extent swept by the rotor of the turbine.

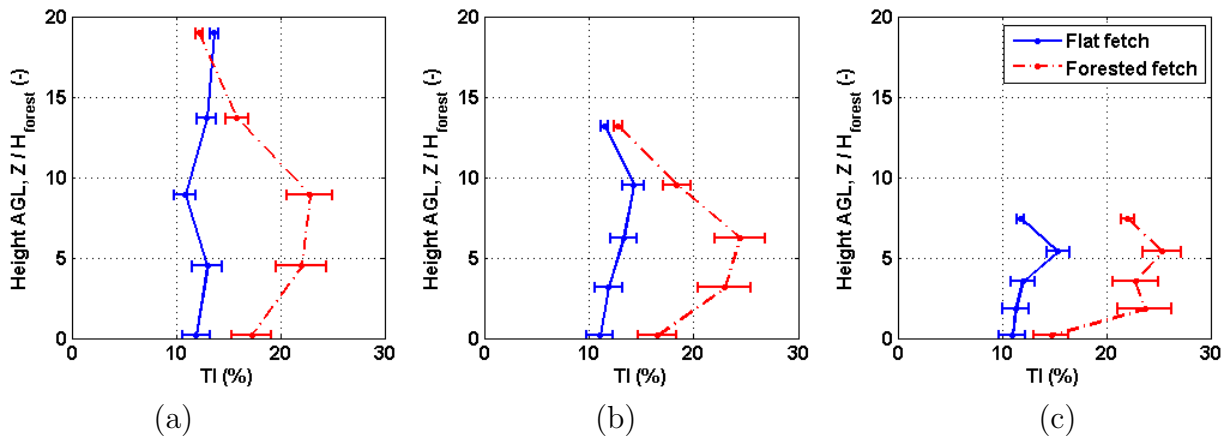


Figure 5.5: Vertical profiles of TI at (a) $X = 10H_{forest}$, (b) $X = 20H_{forest}$ and (c) $X = 30H_{forest}$.

line is indicative of the sensitivity of the power fluctuation to turbulent kinetic energy. It is seen that the highest sensitivity is at wind speeds of $9m/s$ that is slightly below the rated wind speed of $11m/s$. Blade pitching at wind speeds above $10m/s$, can be the reason for lower sensitivity relative to turbulent kinetic energy of power fluctuations, at wind speeds higher than $10m/s$.

5.2 Impact of forested fetch on structural loads on wind-turbine towers

Figure 5.7 shows the deflections of the tower of Turbine 10 as the turbine transitions from a feathered-blade mode of operation to a normal mode of operation (below rated wind speed). The three phases of the turbine's operations are highlighted by the coloured background in Fig. 5.7: the green background corresponds to the feathered mode of operation from $time = 0s$ to $time = 200s$; the yellow background indicates the transition from $time = 200s$ to $time = 340s$; and the pink background corresponds to the normal operating mode that is measured from $time = 340s$ onwards. During these measurements of the tower deflections, the measurements of turbulence reported above in section 5.1 were made. In Fig. 5.7, the deflections are measured relative to the mean position of the tower head during the feathered-mode of operation (that is the mean position is evaluated over the time period of $0s$ to $200s$). The standard deviation of tower head deflections is $0.04m$ during the feathered blade mode of operation, and is $0.12m$, three times larger, during the normal operation mode.

Fig. 5.8 shows the PSD of the deflections of the tower heads of the turbines with unforested (Turbine 10 in Fig. 5.1) and forested (Turbine 14 in Fig. 5.1) fetch. The range

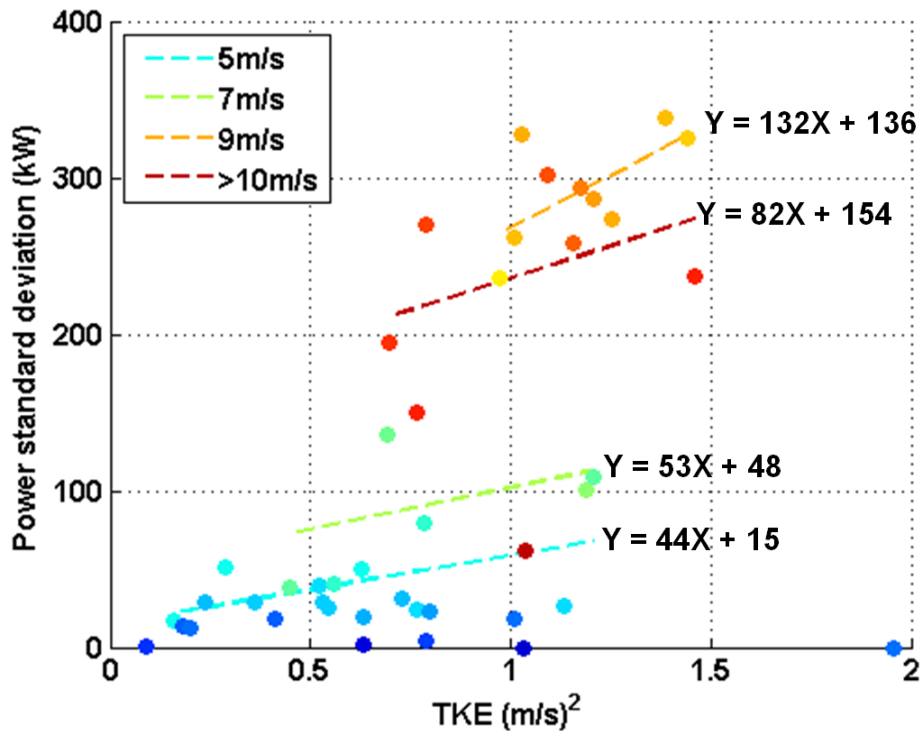


Figure 5.6: Power fluctuations measured at Martigny wind turbine, section 2.2.4. The dashed lines are linear fits at each wind speed bin. The fitted line equation in each wind speed bin is shown next to the line.

of turbine rotor speeds, from $10.8rpm$ to $19.1rpm$, is highlighted in Fig. 5.8. Figure 5.8 shows the PSD during feathered-blade mode. In the PSD of the deflections of the turbine with unforested fetch, no distinct peak is seen, whereas for the turbine with forested fetch there is a spectral peak at $0.32Hz$. This peak in the PSD is attributed to the tower first bending harmonic in the fore-aft direction. It is evident that the tower natural frequency is above the range of the rotor's operational speeds. Such a design would allow the tower's mass to be optimised and the deflections of the tower head to be minimised during normal operation of the turbine. The amplitude of the PSD at the tower's natural frequency is 4 times larger for the turbine with forested fetch, compared to the amplitude for the turbine with unforested fetch. Fig. 5.8b shows the PSD of tower head deflections during normal operation of the turbines. For the turbine with forested fetch, the PSD amplitude at the tower natural frequency is reduced by a factor of 3.4 during operation, compared to the amplitude during feathered-blade mode; this reduction in the amplitude is attributed to the increased aerodynamic damping during normal operation of the rotor [91]. The dominant spectral peak for both turbines is at a frequency of $0.27Hz$ ($16rpm$), which is the rotor rotation frequency. However, the PSD amplitude at this frequency is 2.8 times

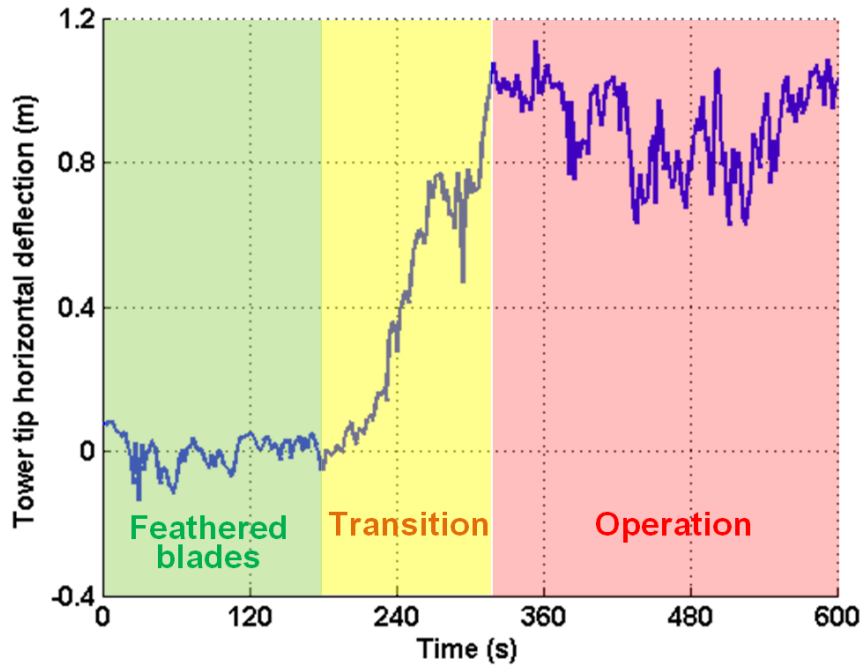


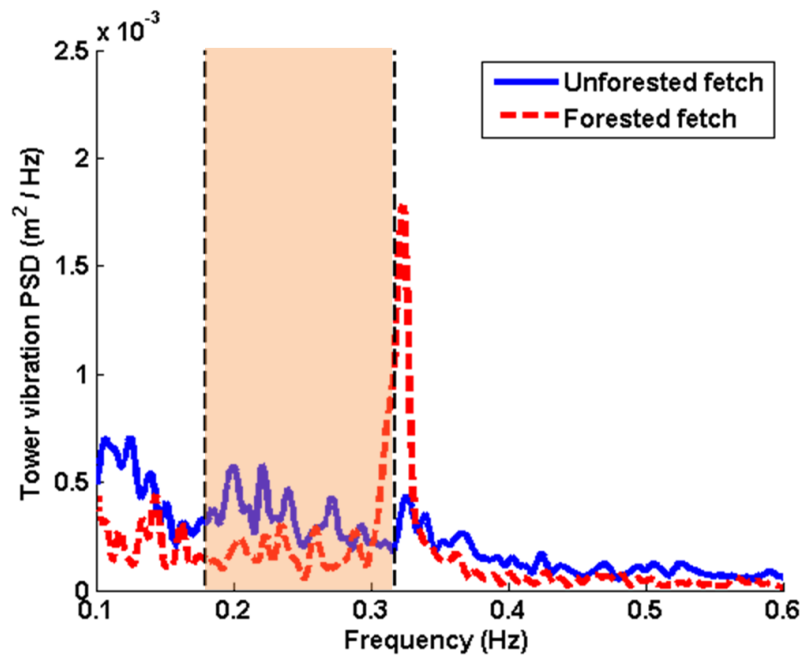
Figure 5.7: Deflection of the tower head of the turbine with flat fetch (Turbine 10 in Fig. 5.1) during three phases of (i) feathered-blade (highlighted in green), (ii) transition to operation (highlighted in yellow) and (iii) operation (highlighted in red).

higher for the turbine with forested fetch, compared to the amplitude for the turbine with unforested fetch. As discussed above the TI in the forested fetch upstream of Turbine 14 is up to 2.5 times larger than the TI in the unforested fetch upstream of Turbine 10. This may explain the larger amplitude in the PSD.

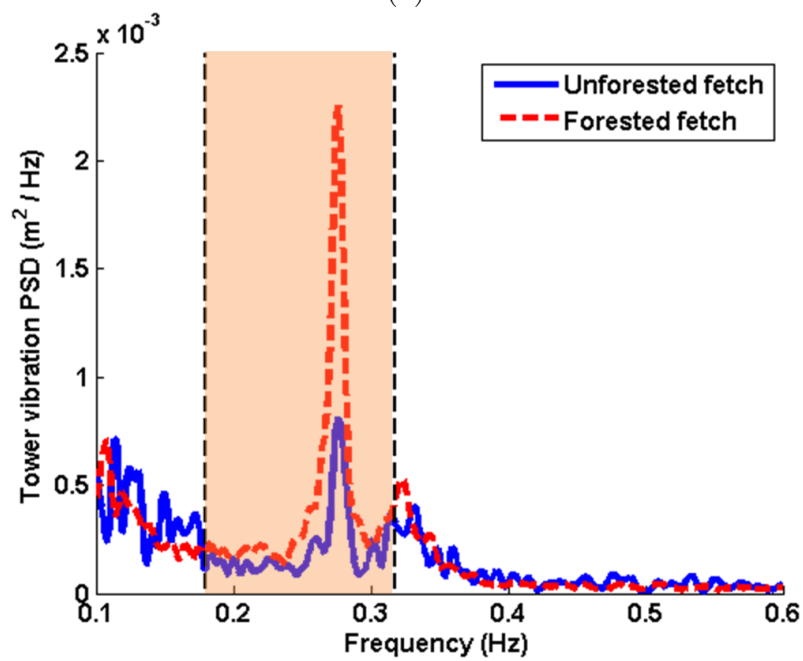
5.3 Generalized model of impact of forest on downstream flow field

An analytical solution for the disturbance of the turbulent boundary layer due to a finite rough surface is provided in [2]. An undisturbed neutral boundary layer over a smooth surface with roughness length Z_1 is considered, Fig. 5.9. Due to the finite rough surface with roughness length Z_0 , three different zones are considered for the flow field; a) Zone 1, where turbulent kinetic energy is not modified; b) Zone 2, where vertically-diffused turbulent energy from the rough surface increases the Reynolds stress; and c) Zone 3, where influence of relieved surface stress due to the smoother surface is included in the streamwise drag force.

Reynolds stress and shear stress are considered as the drag force in Zone 1. In Zone 2,



(a)



(b)

Figure 5.8: PSD diagram of tower tip vibrations, (a) during feathered-blade mode of the turbines, (b) during operation of the turbines.

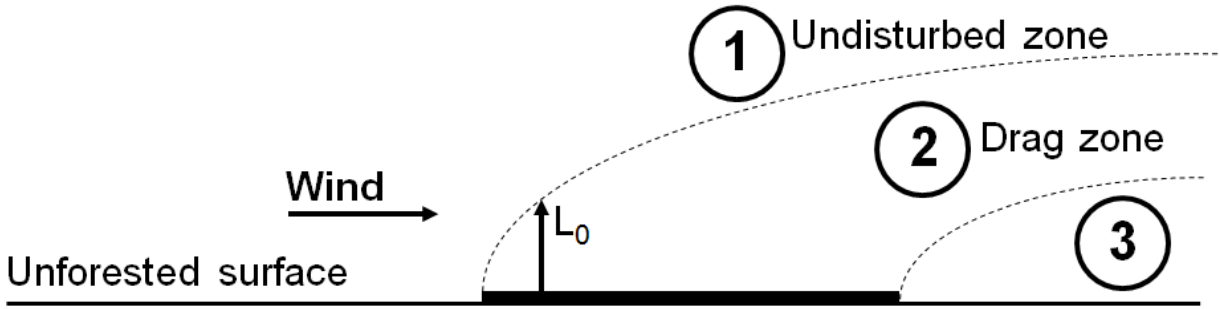


Figure 5.9: Schematic of the analytical solution provided in [2].

Reynolds stress is modified, with an unknown function $F(z/L_0)$, to include the influence of higher turbulent kinetic energy from the rough surface with roughness length Z_0 . In Zone 3, in addition to the disturbance included in Zone 2, a third unknown function, $G(z/L_0)$, is considered to include the impact of roughness length reverting to Z_1 . Equations of mass and momentum conservation are considered for all three zones to determine the unknown functions, $F(z/L_0)$ and $G(z/L_0)$.

In order to achieve the final solution, three assumptions are made; a) neutral boundary layer is assumed for the vertical profile of wind speed in the undisturbed region; b) the roughness length Z_0 is small compared to the thickness of the disturbed region, L_0 in Fig. 5.9, that is $Z_0 \ll L_0$; c) the thickness of the disturbed region, L_0 , is small compared to the thickness of the boundary layer. As detailed in [2], the solution results in a self-similar form shown in Equ. 5.1.

$$\frac{\kappa}{\nu_0} \left(1 - \frac{U}{U_{undisturbed}} \right) = \begin{cases} e^{-z/L_0} + \frac{\log(z/L_0)}{\log(L_0/z_0)}, & z < L_0 \\ e^{-z/L_0}, & z \geq L_0 \end{cases} \quad (5.1)$$

in which κ is the Karman constant, U is the horizontal wind speed downstream of the forest and $U_{undisturbed}$ is the undisturbed horizontal wind speed. The discussed analytical solution is used to develop a semi-empirical model of impact of forest on the downstream flow field. The measurements made at a forest adjacent to EOSH wind farm (Section 2.2.2) are used for developing this model. Measurements of vertical profiles of wind speed from Positions 1-4, shown in Fig. 5.10, are used to develop this model.

Figure 5.11a shows the vertical profile of undisturbed wind speed measured at Position 1. The power-law fit, $U(h) = U_0(h/h_0)^\alpha$, yields an exponent α of 0.1. According to [92], this exponent is within the range of power-law exponents that are attributed to a neutral boundary layer. Figure 5.11b shows the deviation of measurements from the power-law fit, computed in the shape of $1 - U/U_{undisturbed}$, which is the same as the convention used by the analytical solution, Equ. 5.1. The vertical profile in the undisturbed flow has 1.5%

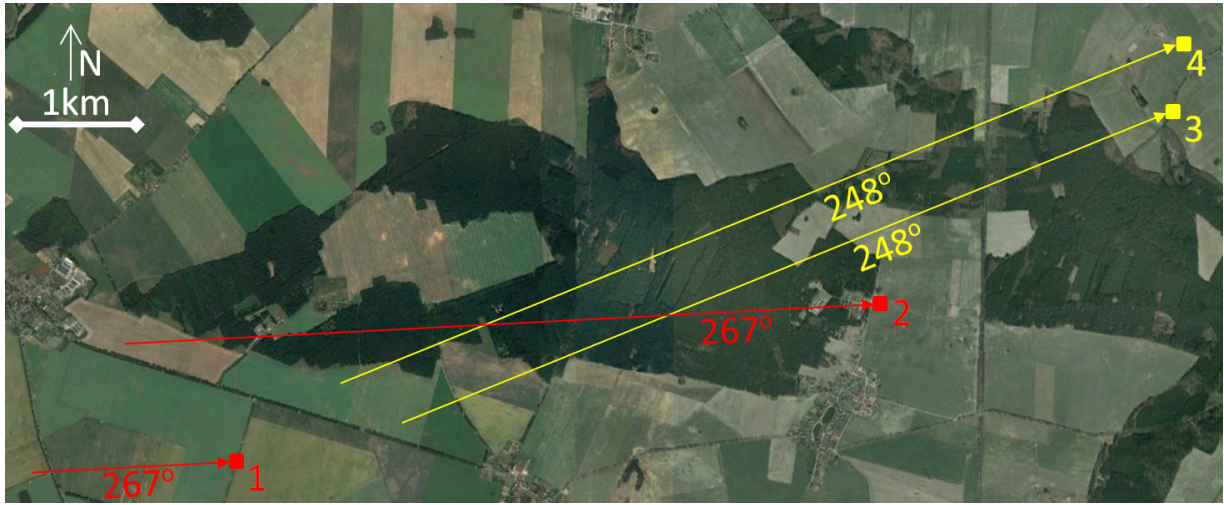


Figure 5.10: Map of land cover at measurement site. The vertical profile in undisturbed flow is measured at Position 1. Vertical profiles at $5H_{forest}$, $25H_{forest}$ and $45H_{forest}$ downstream of the forest edge are respectively measured at Position 2, 3 and 4. Wind directions during measurements are shown with red and yellow lines.

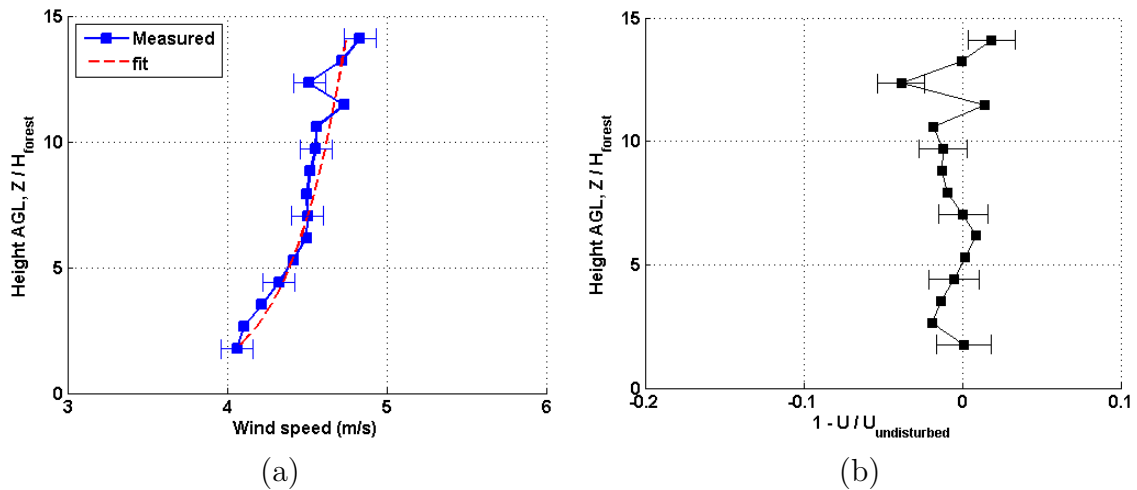


Figure 5.11: Vertical profile of wind speed for undisturbed flow (a) horizontal wind speed, and (b) velocity deficit calculated with the same convention as Equ. 5.1.

deviation in absolute terms from power-law fit.

Immediately following measurements at Position 1, the vertical profile is measured at Position 2, which is located $5H_{forest}$ downstream of the forest edge. The streamwise extent of forest is $280H_{forest}$ for the wind direction of 267° , shown with the red line. The wake deficit, measured at Position 2 is shown in Fig. 5.12. The tuned model, as

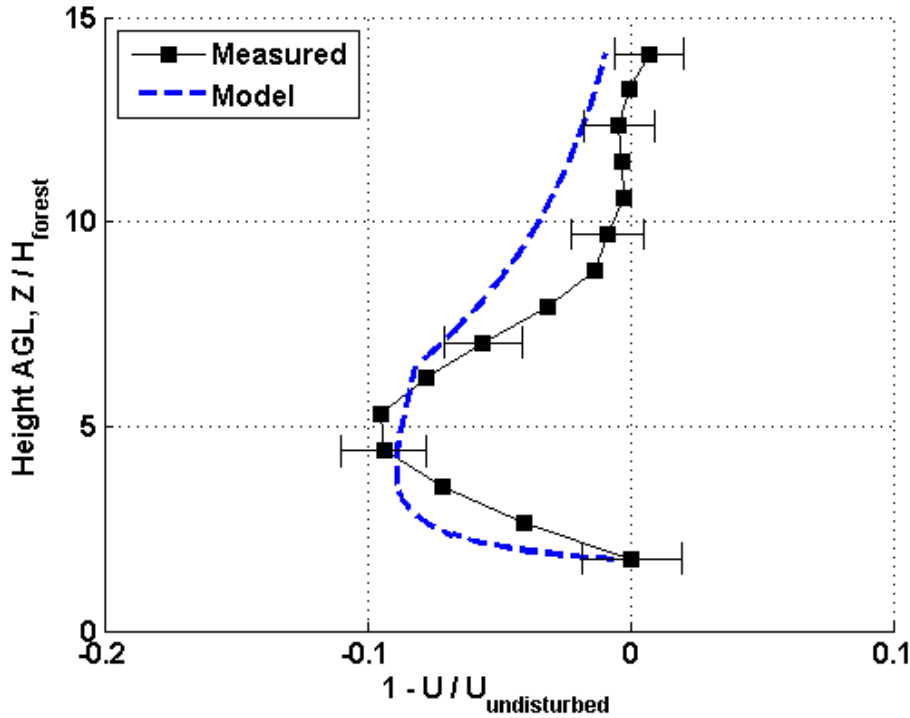


Figure 5.12: Vertical profile of velocity deficit at $5H_{forest}$ downstream of forest edge.

detailed in Equ. 5.2, is also shown in Fig. 5.12. C_{sc} is used to scale the amplitude of the wake to fit the measurements. The turbulent kinetic energy is taken as $3u_1^2$ in the analytical solution, in which u_1 is the friction velocity in the undisturbed flow. However, as discussed in [2], turbulence in atmospheric flow can be higher due to the impact of large-scale eddies, which results in a higher turbulent mixing rate. In order to consider higher possible turbulent mixing in the atmospheric flow, the weight of the surface roughness in the model is increased by introducing the coefficient C_{tr} . The least-squares fit of the model to the measured vertical profile yields a value of $98m$ ($5H_{forest}$) for L_0 , which is the thickness of the disturbed zone. The observed high velocity gradients at this height, which is the typical height of wind turbines at EOSH wind farm, can have adverse effects on the operation of downstream turbines. C_{sc} and C_{tr} are respectively 0.25 and 1.43 for the vertical profile shown in Fig. 5.12.

$$1 - \frac{U}{U_{undisturbed}} = \begin{cases} C_{sc} \left(e^{-z/L_0} + C_{tr} \frac{\log(z/L_0)}{\log(L_0/z_0)} \right), & z < L_0 \\ C_{sc} \left(e^{-z/L_0} \right), & z \geq L_0 \end{cases} \quad (5.2)$$

Since the analytical solution [2] results in self-similar vertical profiles at farther downstream positions, the streamwise wake recovery downstream of the forest, Fig. 5.13, is

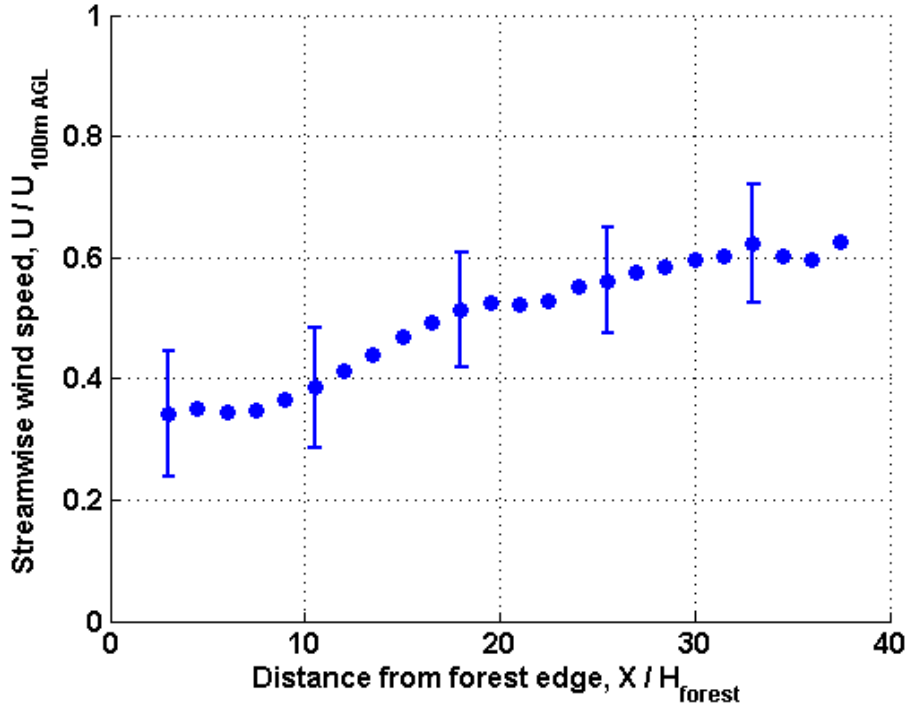


Figure 5.13: Streamwise velocity recovery downstream of a forest edge.

used to generalize the model to farther downstream positions. The wake recovery is calculated from the streamwise wind speed measured along a horizontal beam, starting from Position 4 in Fig. 5.10 towards the forest edge. The uncertainty bars show the standard deviation of wind speeds during the scanning period. Wind speeds are normalized with the simultaneous wind speed at height of 100m AGL. It is observed that recovery rate in the range of $10H_{forest}$ to $20H_{forest}$ downstream of forest edge is considerably higher compared to the recovery rate in the rest of the scanned range.

The observed streamwise recovery is used to scale the wake amplitude at other downstream positions. Additionally, the growth rate of the disturbed region, L_0 in Fig. 5.9, suggested in [2] is considered for generalizing the model to other downstream positions. Figure 5.14 shows the model of Fig. 5.12 at $X/H_{forest} = 5$, together with the generalized model at other downstream positions.

The measured vertical profile of wind speed at Position 3, $25H_{forest}$ downstream of the forest edge, and at Position 4, $45H_{forest}$ downstream of the forest edge, are used to assess the predictions by the model in farther downstream positions. The rms difference of measurements from the model at $X/H_{forest} = 25$ and $X/H_{forest} = 45$ is respectively 1.4% and 1.5% in the absolute terms, while the maximum difference of 3.6% occurs at the downstream position of $X/H_{forest} = 25$ at the height of $Z/H_{forest} = 10$.

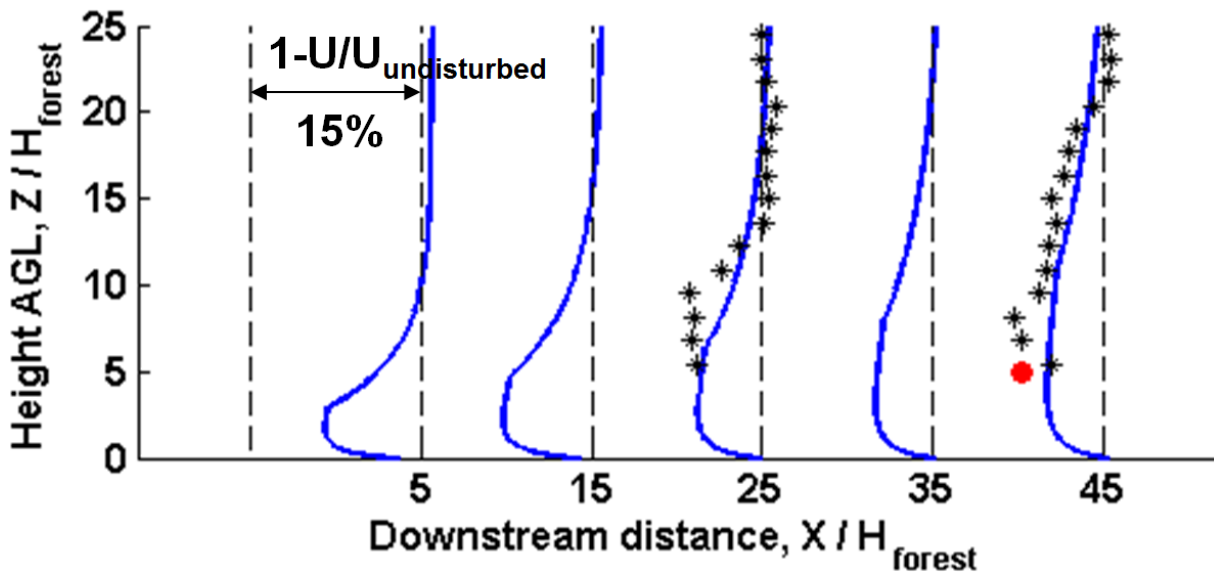


Figure 5.14: Vertical profile of the velocity deficit downstream of a forest. The predictions from the model are shown with the blue lines. Measurements at Position 3 and 4 in Fig. 5.10 are shown with black stars. Red circle shows the equivalent velocity deficit of power loss for a turbine operating at $45H_{forest}$ downstream of forest.

The red circle at the downstream position of $X/H_{forest} = 45$ shows the equivalent velocity deficit, calculated from the observed annual power deficit of a turbine which operates at $45H_{forest}$ downstream of the forest edge. Further details of this long-term data are provided in Section 5.4.1. It is seen that the model is underestimating the velocity deficit up to 4.1% in absolute terms. In addition to the velocity deficit, power losses can occur due to sheared inflow and higher turbulence. This issue can account for the underestimated velocity deficit by the model, as compared to the deficit of the annual energy yield of the turbine.

5.4 Considerations for installing wind farms in forested terrain

Long-term performance of wind turbines in forested and unforested terrain are assessed in this section. One-year SCADA data of wind turbines at EOSH wind farm (section 2.2.2), AltenbruchII wind farm (section 2.2.3) and Martigny wind turbine (section 2.2.4) are used for this assessment. The findings of the previous sections are used to interpret this long-term data. This assessment concludes the study of how a forested fetch can impact the performance of a wind farm.

5.4.1 Annual energy yield

The direction-wise AEY of wind turbines with forested and unforested fetch are compared next. The energy yields of the turbines with unforested fetch (Turbine 10 in Fig. 5.1) and forested fetch (Turbine 14 in Fig. 5.1) are examined, Fig. 5.15. In the calculation of the energy yields, the power generation during the maintenance periods of either of the turbines are excluded. Fig. 5.15a shows the deficit in energy yield of the turbine with forested fetch compared to the turbine with unforested fetch; the deficit is normalised by the direction-wise energy yield of the turbine with forested fetch. The turbine in forested fetch has a maximum deficit of 30% in the wind direction 260° ; for this wind direction for Turbine 14 the upstream extent of the forest is $240H_{forest}$ ($4.8km$) and the distance to the forest is $33H_{forest}$ ($660m$). The upstream extent of the forest determines how far upstream the forest-affected flow is located and the distance to the forest edge determines from how far upstream the elevated turbulence levels start to decay. As observed in Fig. 5.1, Turbine 14 operates downstream of the forest for wind directions 240° to 280° . This range of wind direction is highlighted in Fig. 5.15a. Turbine 10 faces an unforested fetch over the same range of wind directions. Both turbines generate the same AEY in wind directions of 220° and 300° . For a wind direction 220° , both turbines face an unforested fetch and for a wind direction 300° , both turbines face a forest edge that is $70H_{forest}$ and $72H_{forest}$ upstream, respectively. Thus the deficit in energy yield of Turbine 14 over the wind directions in the range 240° to 280° is attributed to the impact of the forested fetch. Over the range of wind directions of 220° to 240° the energy deficit increases from 0% to 17%, although Turbine 14 does not directly face a forest edge. The lateral diffusion of the elevated turbulence due to the lateral mixing could be one reason for this deficit. Furthermore the wind directions shown in Fig. 5.15 are based on the hub height wind direction; however due to wind veer, the wind direction could vary with height. The direction-wise AEYs of the turbines in 10-degree bins, for wind directions of 220° to 300° are shown in Fig. 5.15b.

The direction-wise AEY's range from $16MWh$ to $189MWh$. Over the 220° to 300° range of wind directions Turbine 14 has a deficit in energy yield of $193MWh$ compared to Turbine 10. Based on the 2015 feed-in-tariff of $0.09EUR/kWh$, these deficits translate into a yearly loss in income of $17'000EUR$.

The wind rose at the wind farm is shown in Fig. 5.16. It can be seen that the dominant wind directions are west, south-west and east. In this regard the placement of Turbine 14 relative to the forest is unfortunate as these wind directions have the highest occurrences. Based on the wind rose, the observed deficit in energy yield that is shown in Fig. 5.15a, over wind directions from 220° to 300° , constitutes a 17% of loss in the total AEY of Turbine 14.

As observed in Fig. 5.1, the streamwise extent of forest upstream of Turbine 14 varies at different wind directions. The streamwise extent of forest is expected to influence the power deficit of downstream turbines. Figure 5.17 shows the direction-wise power deficit

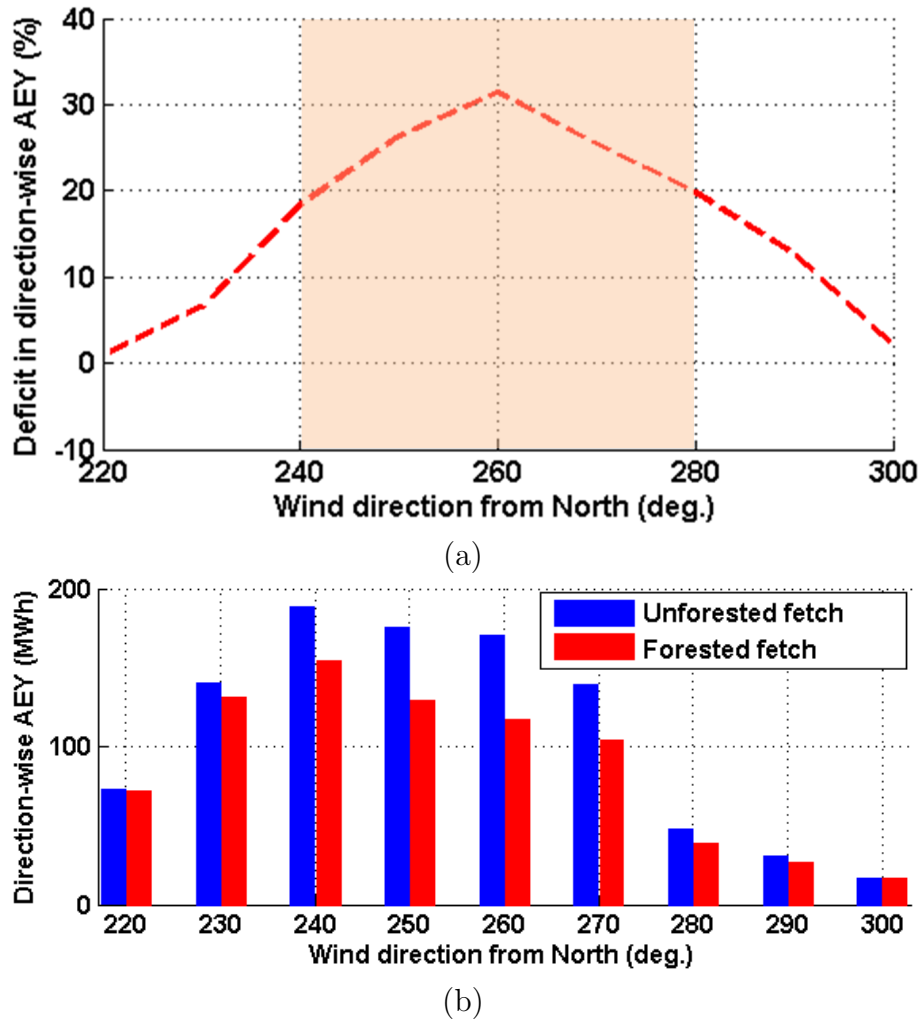


Figure 5.15: (a) Deficit in direction-wise AEY of a turbine with forested fetch relative to turbine with flat fetch (Turbine 14 and 10 in Fig. 5.1, respectively); the deficit is normalised relative to the direction-wise AEY of turbine with flat fetch, (b) direction-wise AEYs of turbines with flat and forested fetch.

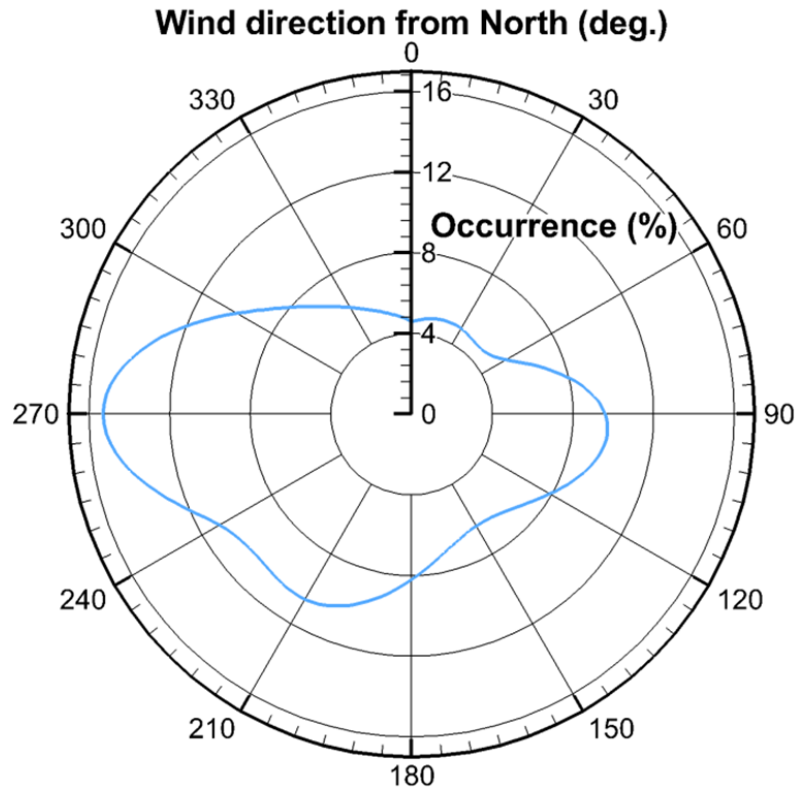


Figure 5.16: Wind rose at the location of EOSH wind farm, detailed in 2.2.2.

of Turbine 14 versus streamwise extent of forest at each wind direction bin. The fitted curve is the same as Equ. 5.2, where the streamwise extent of forest is used as the length scale, z , in Equ. 5.2. It is observed that the power deficit increases for forest streamwise extent smaller than $100H_{forest}$, however for forest extent longer than $100H_{forest}$, there is no specific correlation between power deficit and forest extent.

5.4.2 Power curve scatter

Power fluctuations with a time-scale of 10 minutes can increase the grid operating costs [93]. Additionally, power fluctuations increase the scatter in the actual power production around the nominal power curve. The latter increases unpredictability of power generation in the wind sector. As the installed wind capacity continues to increase, predictability in power generation is of increasing importance in the operation of power systems [94]. The average scatter in the power generation relative to the power curve of six turbines at the three different sites derived from a one year time-series of SCADA data is shown in Fig. 5.18. The scatter is calculated as the difference of the actual power generation from the power curve, normalised by the generated power, for wind speeds between the cut-in and rated

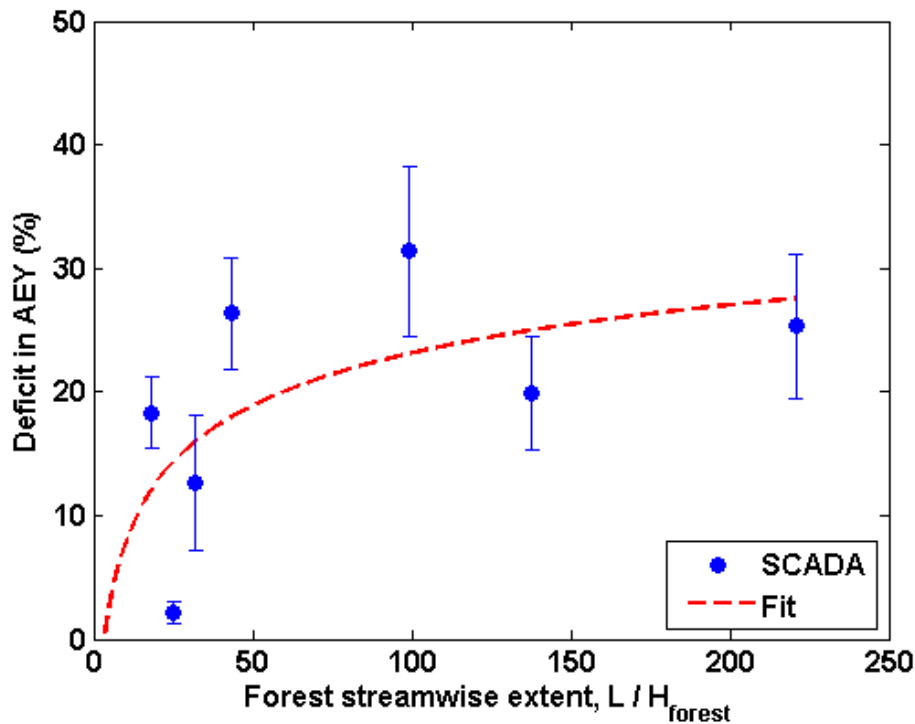


Figure 5.17: The power deficit of wind turbine versus the streamwise extent of forested fetch.

wind speeds of the turbines. EOSH wind farm (section 2.2.2), shown with green, is located in flat forested terrain, AltenbruchII wind farm (section 2.2.3), shown in blue, is located in flat unforested terrain and Martigny wind turbine (section 2.2.4), shown in red, faces a flat fetch with agricultural land from the dominant wind direction. In general, the wind turbines in forested terrain have higher scatter. It can be observed that similar turbines, Vestas V80 with hub height of 100m, which are located in two different terrains, one in forested terrain and the other one in unforested terrain have considerable differences; that is the turbine in forested terrain shows a 2 times higher power curve scatter, compared to the turbine in unforested terrain.

5.4.3 Power deficit due to wake

The impact of forests on the wake losses within wind farms is examined in Fig. 5.19. As wakes are characterised by a deficit in wind speed and elevated levels of turbulence, both of which are seen in the measurements above to be features of the flow downstream of forests, this impact is relevant for the further development of onshore wind farms. For this assessment, the one-year power generation of the wind turbines at EOSH wind farm (Section 2.2.2), which is in flat forested terrain, and AltenbruchII wind farm (Section

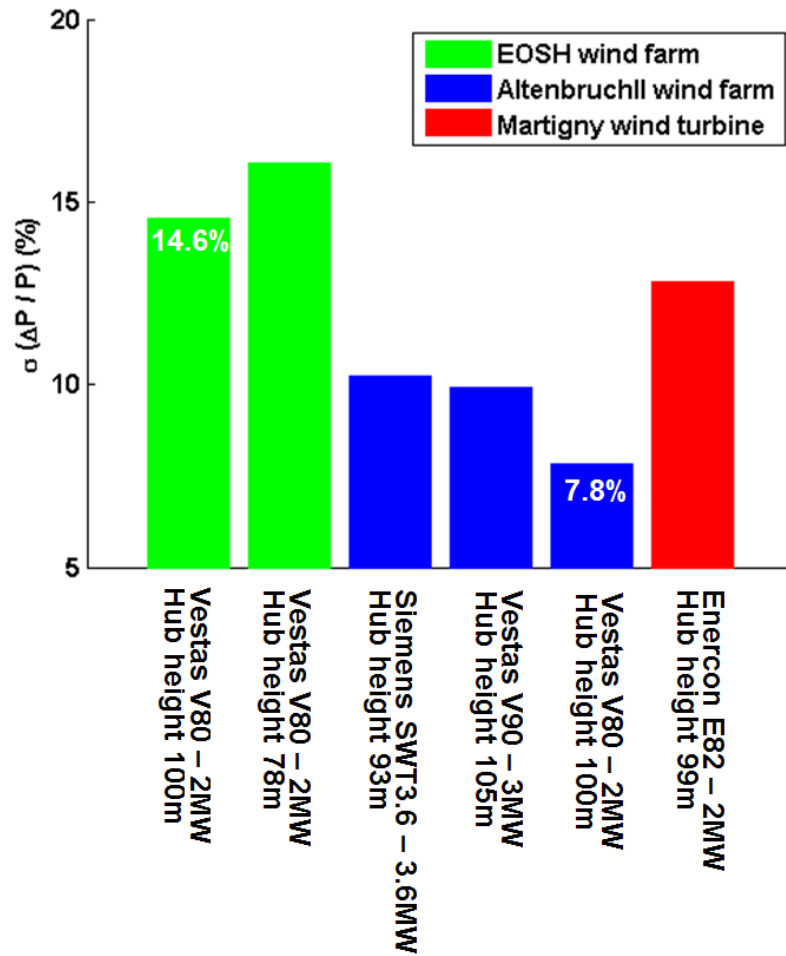


Figure 5.18: Normalized power curve scatter for six wind turbines in three wind farms.

2.2.3), which is in flat unforested terrain, are assessed. From the 10-degree bin bucketed energy yields, Fig. 5.19 shows the decrease in the energy yield, that is wake loss, between each pair of turbines which are installed within a distance less than $7D$ from each other. Overall it can be seen in Fig. 5.19 that as the separation distance between wind turbine pairs increases the wake losses decrease. The maximum wake loss of 55% occurs in flat unforested terrain for turbines with a separation distance of $3.5D$ and the minimum wake loss of 20% in flat forested terrain for separation distance of $6.5D$. It can also be seen that for a given separation distance, the wake losses are larger in the unforested terrain compared to the forested terrain. As forests result in elevated turbulence levels, the higher mixing rates in the wake result in a faster recovery in the wind speeds, and therefore a smaller wake loss. In order to assess this hypothesis, CFD simulations using MULTI3, the in-house CFD tool described in section 2.5.1, are performed.

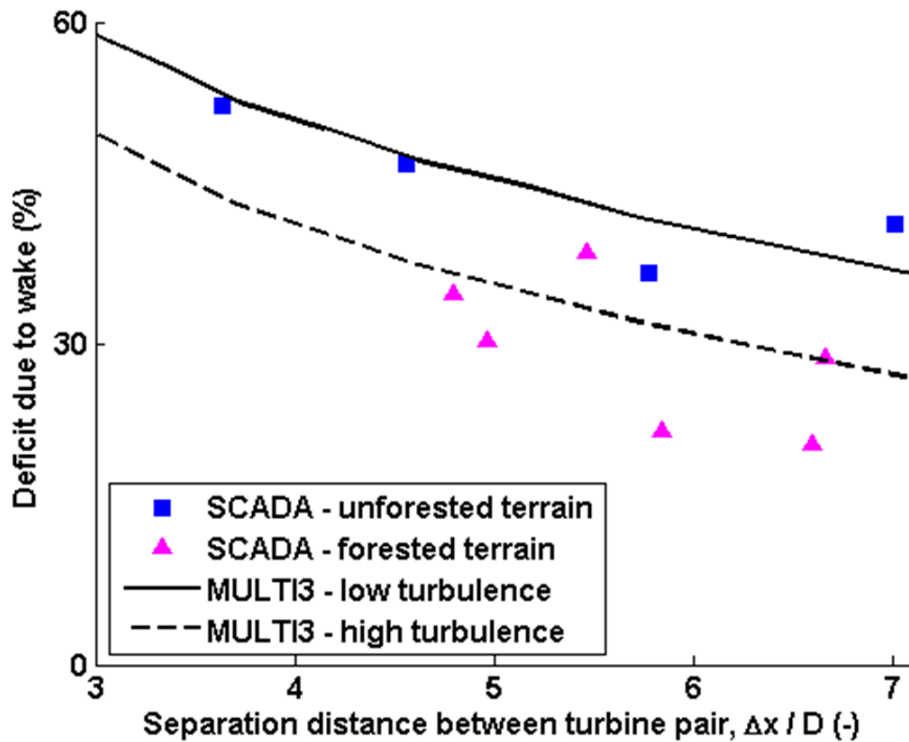


Figure 5.19: Impact of turbine separation distance on the power deficit due to the wake from upstream turbines. The symbols show the deficit in the direction-wise AEY measured on the turbines' SCADA. The solid and dashed lines show the deficit predicted using the in-house CFD tool, MULTI3.

Deficits in cubed hub-height wind speed, predicted by MULTI3, are also shown in Fig. 5.19. Simulations were performed for two different turbulence levels. The difference in TI in high-turbulence and low-turbulence case is adjusted according to average difference in TI of forested and non-forested fetch observed in Fig. 5.4. The deficit in cubed wind speed is on average 9.7% lower in the high-turbulence case, which is in good correlation with the averaged difference of 11% between power deficit in forested and unforested terrain. This analysis shows that higher turbulence in the forested fetch can account for lower power deficit due to the wake of upstream turbines in forested terrain.

5.4.4 Maintenance requirements

The measurements of TI, presented above, show up to 2.5 times larger TI in the forested fetch compared to the unforested fetch. Furthermore, the measured tower head deflections of turbines in a forested fetch compared to unforested fetch are 2.8 times larger during normal operation and 3.4 times larger when the blades are feathered. The larger aeroelastic

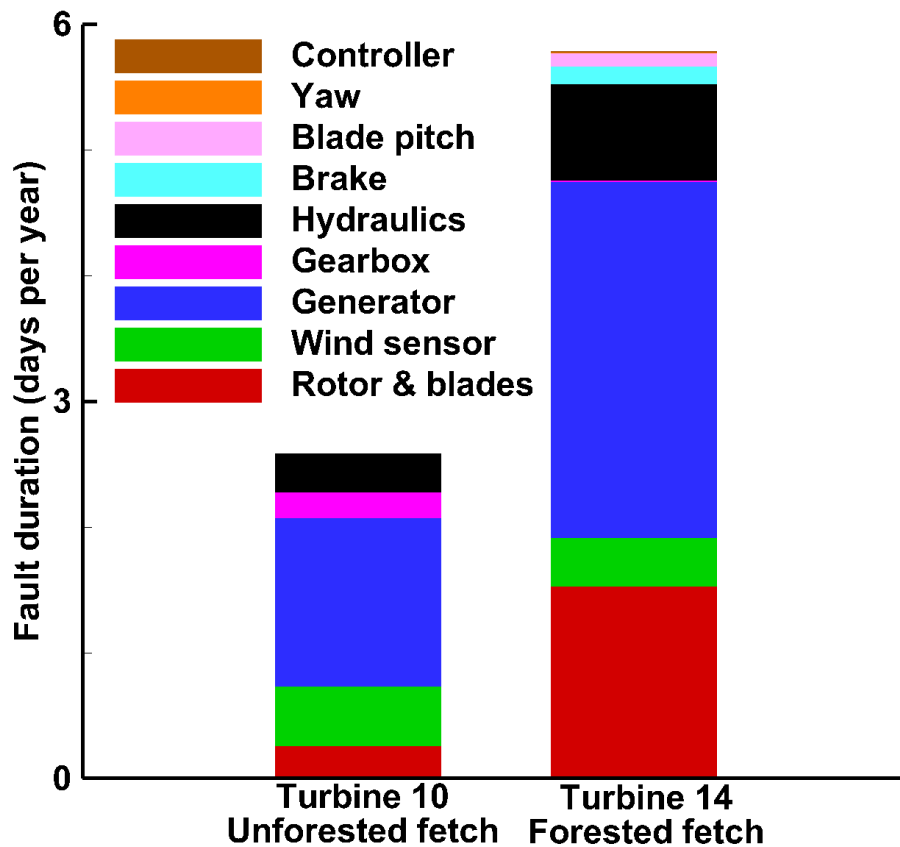


Figure 5.20: Component-wise maintenance of turbines averaged over 7 years; the scheduled annual and bi-annual maintenance of turbines is excluded.

deflections of the tower head imply that there are larger fatigue loads on a turbine in a forested fetch, which may consequently be manifested in larger occurrence of faults in the turbine's mechanical load-bearing components. This larger number of faults would result in higher maintenance costs. It should be noted that based on the wind rose that is shown in Fig. 5.16 and the positions of the wind turbines relative to forest as shown in Fig. 5.1, the fraction of the time that the Turbine 14 faces the forest with a distance of less than 1km upstream is 55%, whereas this fraction for Turbine 10 is 4%. In order to assess the impact of the forested fetch on the maintenance requirements of wind turbines, the 7-year event-logs of Turbines 10 and 14 are compared. Fig. 5.20 summarises the fault durations associated with events related to rotor and blades, wind sensor, generator, gearbox, hydraulics, brakes, blade pitch mechanism, nacelle yawing mechanism and controller. The events related to the annual and bi-annual maintenance of the wind farm are excluded in Fig. 5.20.

As summarised in Table 5.1, the mean fault duration for Turbine 14 is 5.8 days per year, which is 2.2 times larger than the mean fault duration of Turbine 10. The compo-

Table 5.1: Summary of fault durations derived from event-logs of turbines in forested and unforested fetch.

Mean fault duration per year (day)	Unforested fetch	Forested fetch
Total	2.6	5.8
Rotor and blades	0.3	1.5
Generator	1.3	2.8
Hydraulics	0.3	0.8

nents that are most problematic on Turbine 14 are the rotor and blades, generator and hydraulics, which have respectively 5.9, 2.1 and 2.4 times larger fault durations, compared to Turbine 10. This observation may be expected as, in addition to larger fluctuating loads on the generator, the higher torque fluctuations caused by larger turbulence produce higher fatigue loads on rotor, blades and hydraulics. Unlike Turbine 14, no fault durations related to brake, blade pitch mechanism, yawing mechanism and controller are observed on Turbine 10.

5.5 Concluding remarks

Turbulence matters for wind energy. Higher turbulence levels increase the fluctuations of the generated power at all wind speeds; with highest sensitivity being observed at wind speeds immediately below rated wind speed. The aeroelastic deflections on the tower of the turbine increase at higher turbulence levels. This phenomenon is observed for the wind turbine whose blades are feathered as well as the wind turbine in operating mode.

The rough surface of canopies increases downstream turbulence intensity for up to 15% in absolute terms. The analysis of the power generation shows that there is up to 30% of deficit in energy yield for specific wind directions due to the forested fetch and overall a 17% lower annual energy yield for the turbine in a forested fetch compared to the turbine in an unforested fetch. Turbines in forested area show up to 2 times higher power curve scatter. An analysis of the maintenance log of the wind farm in forested terrain shows fault durations associated with the rotor, generator and hydraulics on the turbine in a forested fetch are 5.9, 2.1 and 2.4 times larger compared to the turbine in an unforested fetch. Although deficits in wind speed and elevated turbulence levels due to forests are shown to have an adverse impact on power generation, wake losses are observed to be lower in forested terrain compared to unforested terrain. The smaller wake losses are attributed to higher mixing and faster recovery due to the elevated turbulence levels downstream of the forest. This hypothesis is verified by CFD simulations of wake recovery.

The observations made in this work should be considered as the development of wind farms close to forested areas is continued.

Chapter 6

Structural vibration during steady and transient operation

This chapter details aeroelastic deflections of wind turbines. The measurements are performed at Juvent wind farm (Section 2.2.1). The turbines of interest in this experiment are Turbines 10 and 11, shown in Fig. 2.5, which are Vestas V90 wind turbines with rated power of $2MW$, rotor diameter of $90m$ and hub height of $95m$. The chapter begins with the details of the upstream topology of the two turbines and LiDAR-measured vertical profiles of wind speed and wind turbulence. Second, the performance of the opto-mechanical platform in measuring the geometry and structural deflections of full-scale wind turbine is demonstrated. Next, the tower deflection during transition to cut-off of power and normal operation of the turbine are investigated and the potential load alleviation schemes are assessed. The chapter concludes with key findings of this analysis.

6.1 Upstream conditions; terrain topology and wind turbulence

The wind direction during the measurements is 300° from North. Figure 6.1 shows the surface elevation and the extent of forested fetch upstream of Turbines 10 and 11 along the 300° wind direction. The surface elevation is measured relative to the surface elevation at the base of the respective turbines and is normalised with the hub height. The distance upstream is measured relative to the location of the turbine and is normalised by the rotor diameter. The extent of forested fetch is shown by the thicker line. For Turbine 10 there is an unforested fetch up to $5.5D$ ($500m$) upstream, whereas for Turbine 11 the unforested fetch extends up to $7.8D$ ($700m$) upstream. For both turbines the unforested fetches have monotonic downward slopes of 5° . In the case of Turbine 10, in the forested fetch there

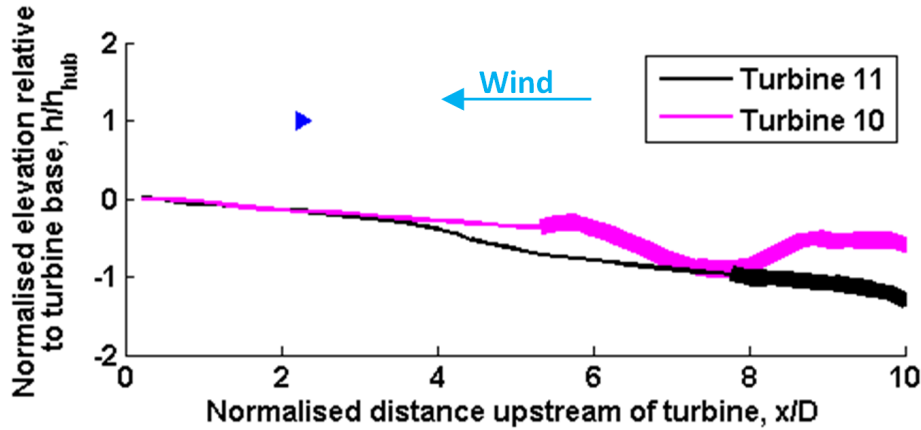


Figure 6.1: Surface elevation and extent of forested fetch upstream of Turbines 10 and 11 along the wind direction. The thicker line indicates the extent of the forest. The measurements of turbulence are made at the location shown by the blue triangle. The location of Turbines 10 and 11 is shown in Fig. 2.5.

is a valley at $6.2D$ ($560m$) whose depth and width are $0.5H_{hub}$ ($50m$) and $2.4D$ ($220m$), respectively.

Fig. 6.2 shows the vertical profiles of wind speed and wind direction. The error bars show the standard deviation of measurements during the 40-minute-long period of the VAD scan. The vertical profile of wind speed is shown in Fig. 6.2a. The dashed red line shows the power law fit, given as:

$$U(z) = U_0 \left(\frac{h}{h_0} \right)^\alpha \quad (6.1)$$

where h is the height above ground level and U_0 is the reference wind speed at the height of h_0 . The exponent, α , is determined to be 0.03 for the present measurements. The small shear coefficient of 0.03 is indicative of a rather uniform flow over the rotor swept height. The vertical profile of wind direction is shown in Fig. 6.2b. The wind direction is 300° at a height of $108m$ AGL, and decreases monotonically to 290° at a height of $490m$ AGL. This average rate of wind direction change with respect to height translates to 5° wind direction change over the rotor swept height. The change in wind direction over height is in the opposite direction to the change that would be expected from the Coriolis force in the Northern hemisphere, thus, other atmospheric processes are also occurring in this atmospheric boundary layer.

Figure 6.3a shows the TI measured upstream of Turbines 10 and 11 in Juvent wind farm (Section 2.2.1). The TI measurements are from the time windows during which the hub height wind speeds are approximately the same for Turbines 10 and 11 (average hub

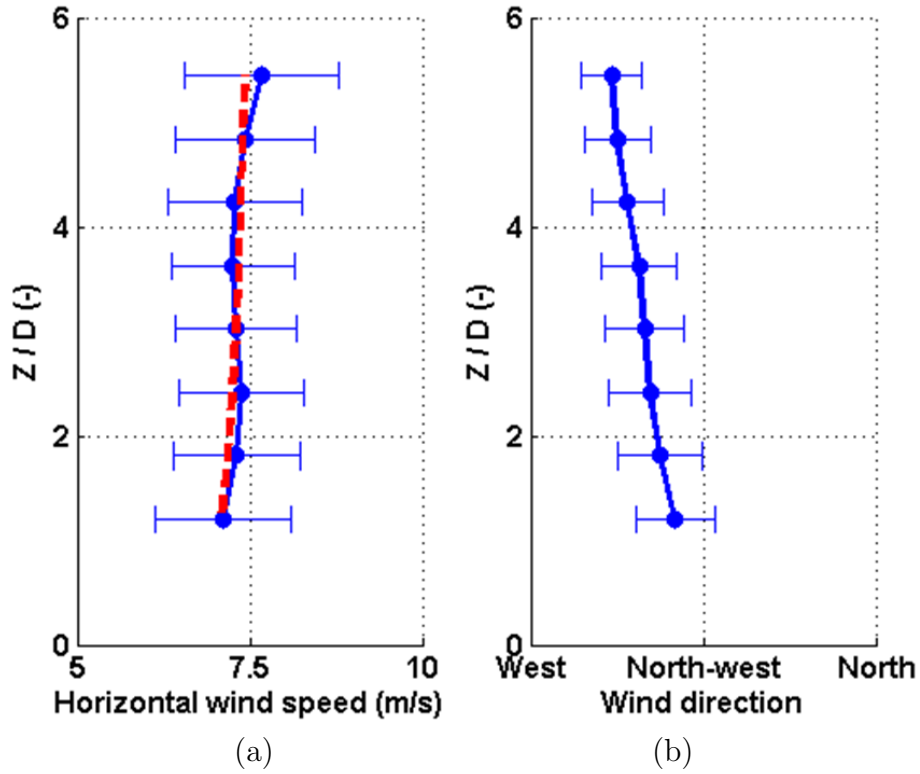
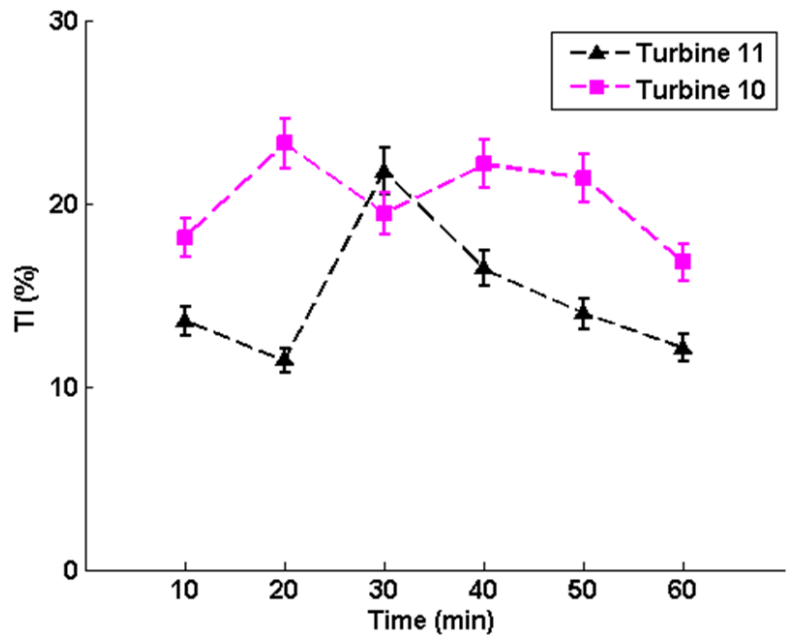
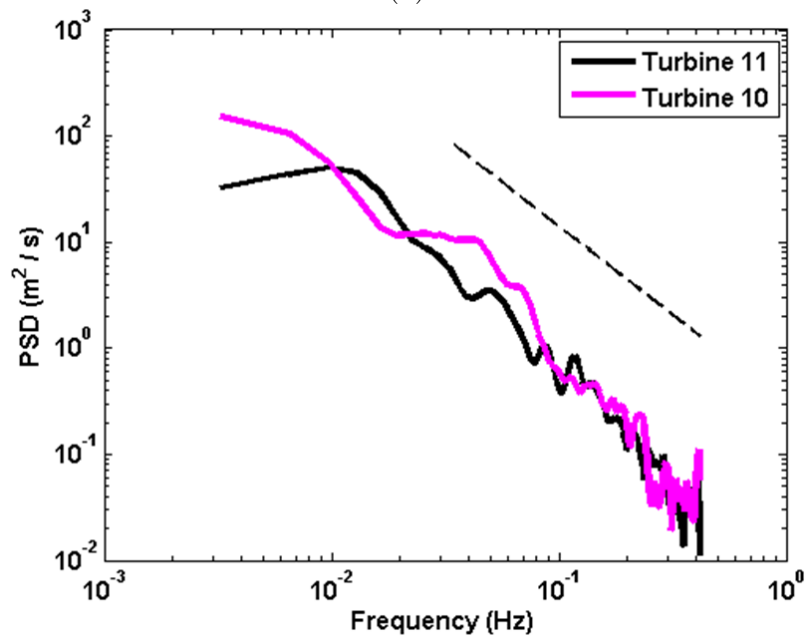


Figure 6.2: Vertical profiles of (a) wind speed and (b) wind direction measured in undisturbed wind.

height wind speed of 7.6m/s for Turbine 10 and 7.4m/s for Turbine 11). The uncertainty bars in Fig. 6.3a indicate the expected range of TI due to turbulence anisotropy. The average TI is 20% for Turbine 10 and 15% for Turbine 11. The larger TI for Turbine 10 is attributed to the impact of the upstream topography, Fig. 6.1. For the wind direction of 300° , there is a 50m deep valley upstream of Turbine 10 and the forested fetch is at $5.5D$ upstream; however, for Turbine 11 the slope in the elevation is constant and the forested fetch is at $7.8D$ upstream. There are two main factors that determine TI; atmospheric stability and upstream topography. Since the interval between the TI measurements at Turbines 10 and 11 is 30 minutes, which is short compared to the periods of semi-diurnal (10 hours) and synoptic (100 hours) weather fluctuations, and because there is no significant difference (less than 3%) in the average wind speeds at Turbine 10 (7.6m/s) and Turbine 11 (7.4m/s), the difference of TI between the two turbines is not attributed to a change in the atmospheric stability condition, but to the upstream topography. Changes in TI due to stability conditions range from 7% for a stable boundary layer to more than 20% for an unstable convective boundary layer [92]. Fig. 6.3a shows that the influence of upstream topography on TI is of the same order of magnitude as that of atmospheric stability.



(a)



(b)

Figure 6.3: (a) Time-series of TI, and (b) PSD of turbulence, measured upstream of Turbines 10 and 11 in Juvent wind farm, section 2.2.1. The black dashed line in Fig. 6.3b shows the slope in the inertial sub-range.

Figure 6.3b shows the PSD of turbulence at Turbines 10 and 11. As observed in Fig. 6.3b, there are larger amplitudes of the PSD, and thus turbulence levels, at Turbine 10 in two frequency ranges: a) frequencies less than $0.01Hz$ which are, related to wind fluctuation with periods more than 100s; and b) in the frequency range of $0.023Hz - 0.085Hz$. The average wind speed during the 10-minute window over which this PSD is calculated is $6.8m/s$. The length scale, U_{ref}/f , attributed to the frequency range of $0.023Hz - 0.085Hz$ is $297m$ to $80m$. It is interesting to note that this length scale is comparable to the $220m$ width of the upstream valley, Fig. 6.1. Both PSDs show the $-5/3$ slope in the inertial sub-range. The onset of the inertial sub-range, attributed to largest eddy size, is in the range of $0.0065Hz$ to $0.0098Hz$, which is equivalent to a length scale of $1000m$ to $700m$.

6.2 Geometry and structural deflections of a full-scale wind turbine

The geometry of a multi-megawatt wind turbine, measured using the opto-mechanical system, is shown in Fig. 6.4. The measurements are made at a 2.0MW Vestas V90, which is Turbine 11 at Juvent wind farm (Section 2.2.1). This turbine is a pitch-controlled, variable-speed wind turbine with a rated wind speed of $13m/s$. Mean wind speed during measurements is $7m/s$. In Fig. 6.4 the tower and nacelle (filled black circle symbols), blade at topmost position (filled blue circle symbols) and blade at bottommost position (filled magenta circle symbols) are shown. The leading and trailing edges of the blade are shown. The tangent to the leading edges of the blades over the most inboard section is shown by the diagonal red dash-dot line. In the bottommost blade position the tip is $2.5m$ from the tangent, and the clearance distance between the tip and tower is $6.2m$.

Simultaneous measurements of wind speed and the leading edge blade geometry of the same turbine (as in Fig. 6.4) are shown in Fig. 6.5. The vertical profiles of horizontal wind speeds, Fig. 6.5a, over the vertical extent of the blade above hub-height, are derived from velocity-azimuth display scans of the scanning LiDAR, which is placed $100m$ upstream of the wind turbine. The profiles are shown for two mean hub-height wind speed conditions of $5m/s$ (low wind speed condition) and $7m/s$ (high wind speed condition). The corresponding blade deflections are shown in Fig. 6.5b; the deflections are measured relative to the blade root. It can be seen that there is a $1.5m$ larger deflection of the blade tip in the high wind speed condition compared to the low wind speed condition.

Figure 6.6 shows the deflections of the upper portion (heights $70m$ to $85m$) of the tower of the same turbine (as in Fig. 6.4). Simultaneous LiDAR measurements show that average wind speed has been $7m/s$ in high-wind condition and $5m/s$ in low-wind condition. There is an approximately $30cm$ difference in the tower deflections under the two different wind conditions.

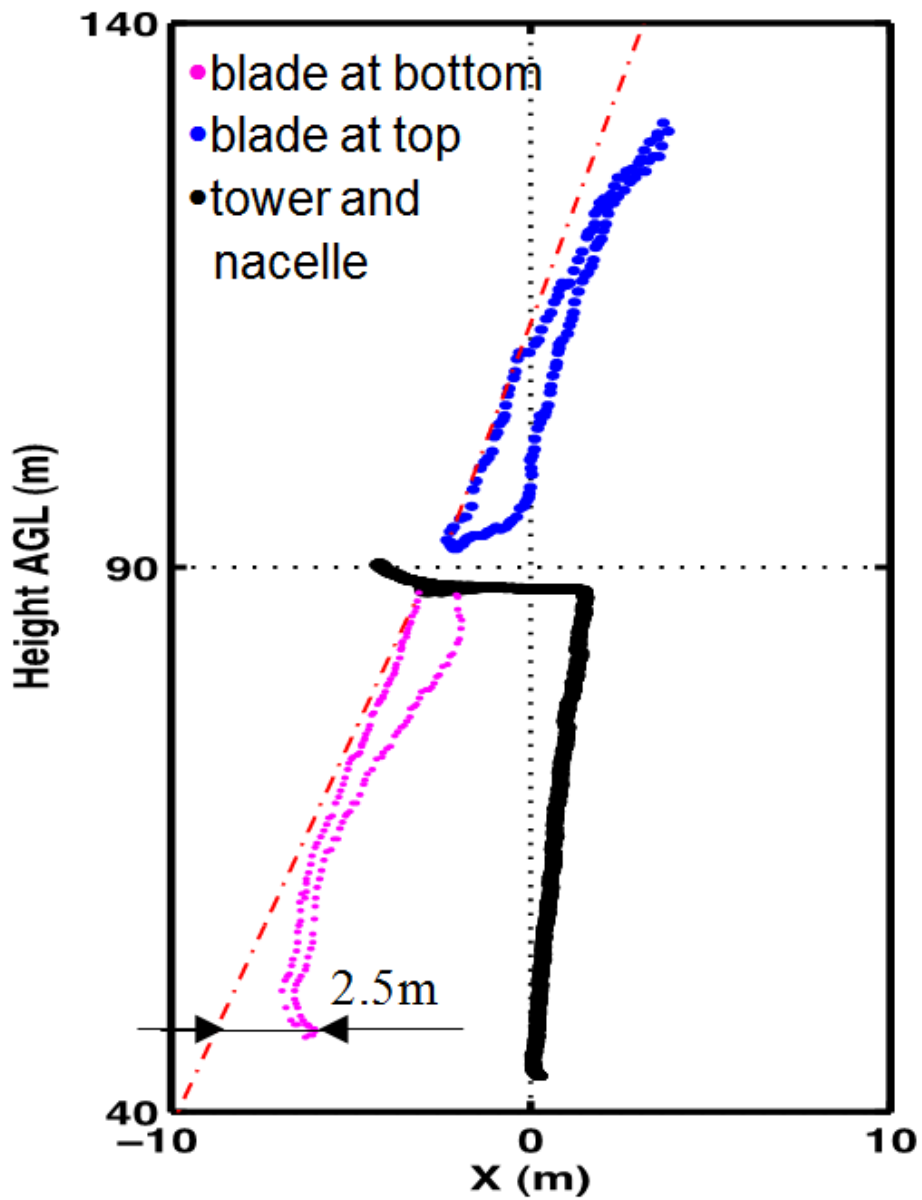
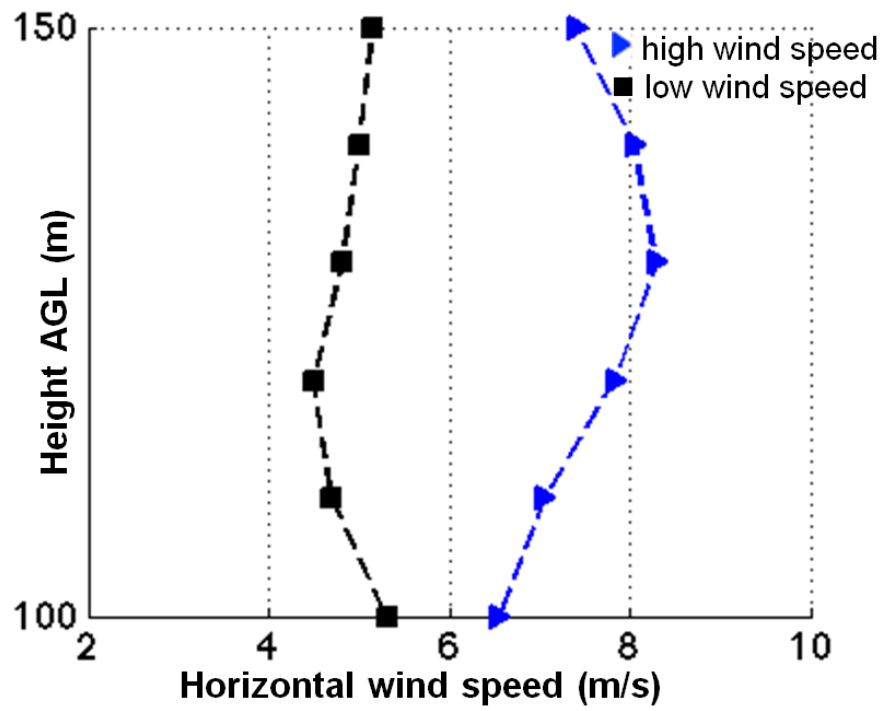
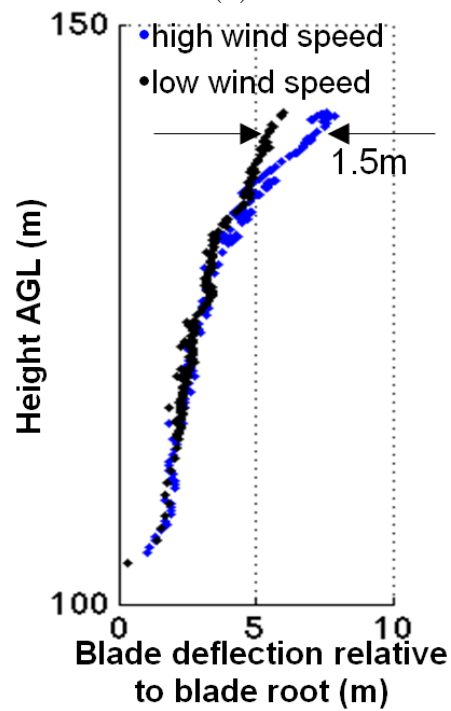


Figure 6.4: Measured geometries of tower, nacelle and blades of turbine 1 (3.0MW Vestas V90). Note that for the sake of clarity, the scale of the x-axis is expanded relative to the y-axis.



(a)



(b)

Figure 6.5: Simultaneous measurements of a) wind speed and b) blade deflections of the same turbine as in Fig. 6.4.

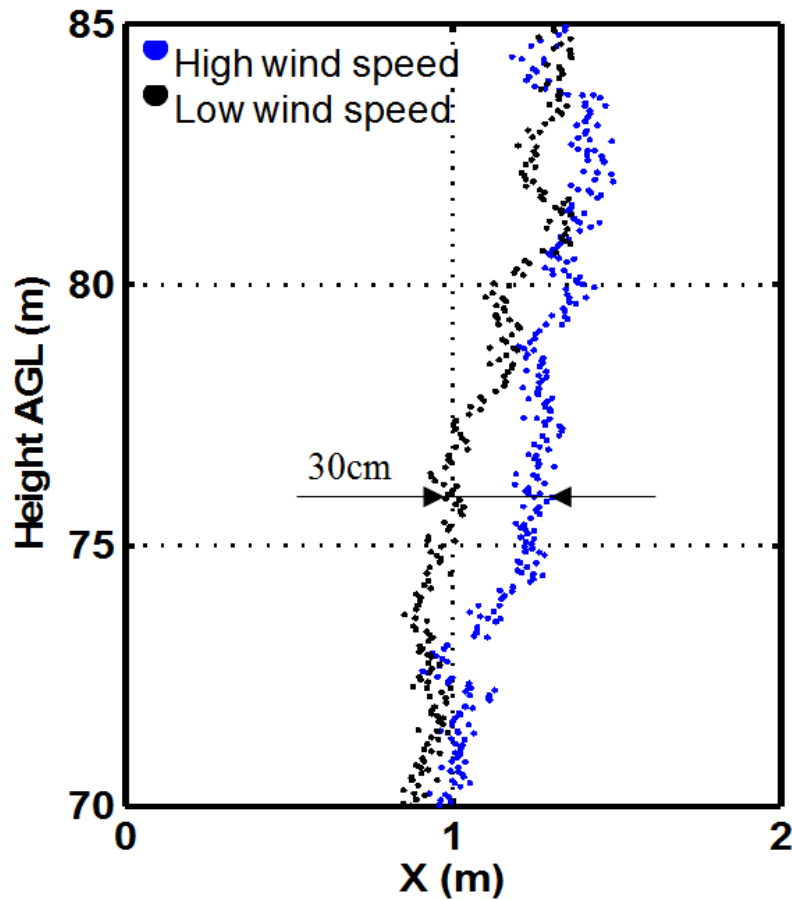


Figure 6.6: Measured deflections of the tower of the same turbine as in Fig. 6.4, in the wind conditions shown in Fig. 6.5a.

6.3 Damping ratio of tower during transition to cut-off of power

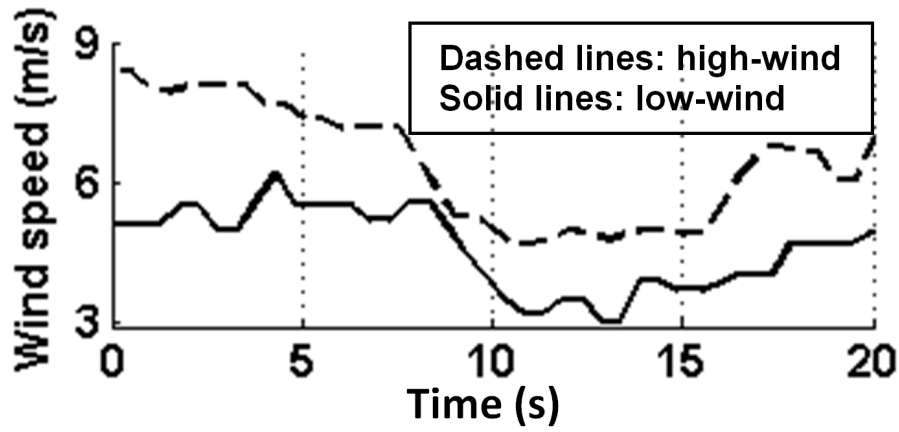
Figure 6.7 shows time histories of wind speed, turbine parameters and tower deflections during two transient power cut-off cases. These measurements are made on Turbine 11 in Juvent wind farm (Section 2.2.1). Case 1, referred to as the high-wind case, is shown by the dashed lines and Case 2, referred to as the low-wind case, is shown by solid lines. The turbine parameters are blade pitch, rotor torque and rotor speed. The hub height wind speed measured with the turbine's anemometer is shown in Fig. 6.7a. There is a 35% decrease in wind speed in both cases, that is a decrease from 8.5m/s to 5.5m/s in the high-wind case and from 5m/s to 3.2m/s in the low-wind case. A transient cut-off of power occurs due to this decrease in wind speed. Figure 6.7b shows the time histories of the blade pitch. It can be seen that in both high-wind and low-wind cases as the wind

speeds decrease, the blades are feathered. The ranges of blade pitching are 14.4° and 9° respectively in the high-wind and low-wind cases. The corresponding rotor torque, which is derived from the instantaneous generated power and rotor speed, is shown in Fig. 6.7c; a drive-train efficiency of 92% is used in the calculation of the rotor torque from generator power. From the time histories of the torque, three phases can be identified: normal operation; transition to power cut-off, and power cut-off. The normal operation lasts from 0s to 4.5s for the high-wind case and 0s to 2.8s for the low-wind case. The transition periods are 4.5s to 12s and 2.8s to 6.8s for the high-wind and low-wind case, respectively. Lastly, it can be seen that the transient cut-offs in power last for 2.1s (from time 12s to 14.1s) and 6.5s (from 6.8s to 13.3s) in the high-wind and low-wind case, respectively.

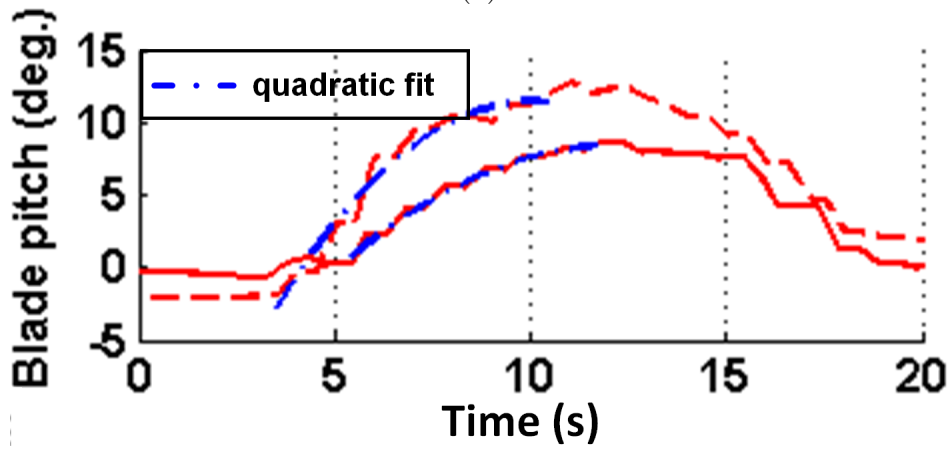
Figure 6.7d shows the rotor speed of the turbine. The tip-speed-ratio before the power cut-off is 8.3 for the high-wind case and 10.2 for the low-wind case, both of which are higher than the rated tip-speed-ratio of 5.4. Figure 6.7e shows the sideways tower deflections that are measured using the opto-mechanical platform. In the low wind case the tower deflections are 30cm with negligible oscillations, however in the high-wind case the maximum deflection is up to 80cm and oscillations with amplitudes of 21cm are observed. The horizontal black dashed lines in Fig. 6.7e indicate the equilibrium positions in both cases; the tower deflection from the equilibrium position is 60cm in the high-wind case and 28cm in the low-wind case. As observed in Fig. 6.7c, the rotor torque before the power cut-off is 0.40MNm in the high-wind case and 0.25MNm in the low-wind case. The oscillation amplitude of 21cm in the high-wind case is considerably smaller than the measured tower deflection from equilibrium of 60cm, before the transition to power cut-off. The power generation during the transition to power cut-off, as shown in Fig. 6.7c, and the corresponding torque on the tower head, account for the rapid decrease from 60cm to 21cm in the amplitude of the oscillation.

The red dash-dot line shows the predicted tower deflections from a free damped vibration of SDOF model. The prediction is very good (rms difference of 5cm) over the first seven seconds (time $t = 6 - 13s$) of oscillation. The prediction of the free damped vibration model over this interval is good because the tower's inertia, stiffness and damping dominate the forcing on the tower. The tower's damping is visible as the amplitude of the second oscillational peak (at time $t = 11s$) is smaller than the first oscillational peak (at time $t = 7s$). The tower damping ratio and natural frequency of tower are predicted to be 6.8% and 0.279Hz. Following the power cut-off at time $t = 12.5s$, the generator starts to operate and as the aerodynamically induced rotor torque and thrust now act on the tower, the free oscillation model is no longer valid.

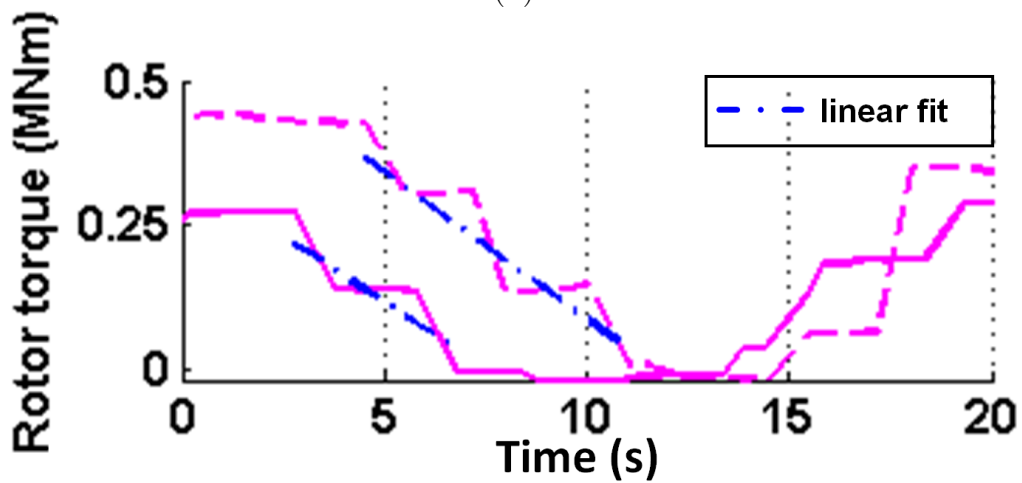
A polynomial fit to the blade pitch shows that the predicted pitching of the blade fits very well to a quadratic curve that is shown with the blue dash-dot line in Fig. 6.7b. Based on this fit, the maximum blade pitching rate in the high-wind case ($4.4^\circ/s$) is found to be twice the maximum blade pitching rate in the low-wind case ($2.2^\circ/s$). The blue



(a)



(b)



(c)

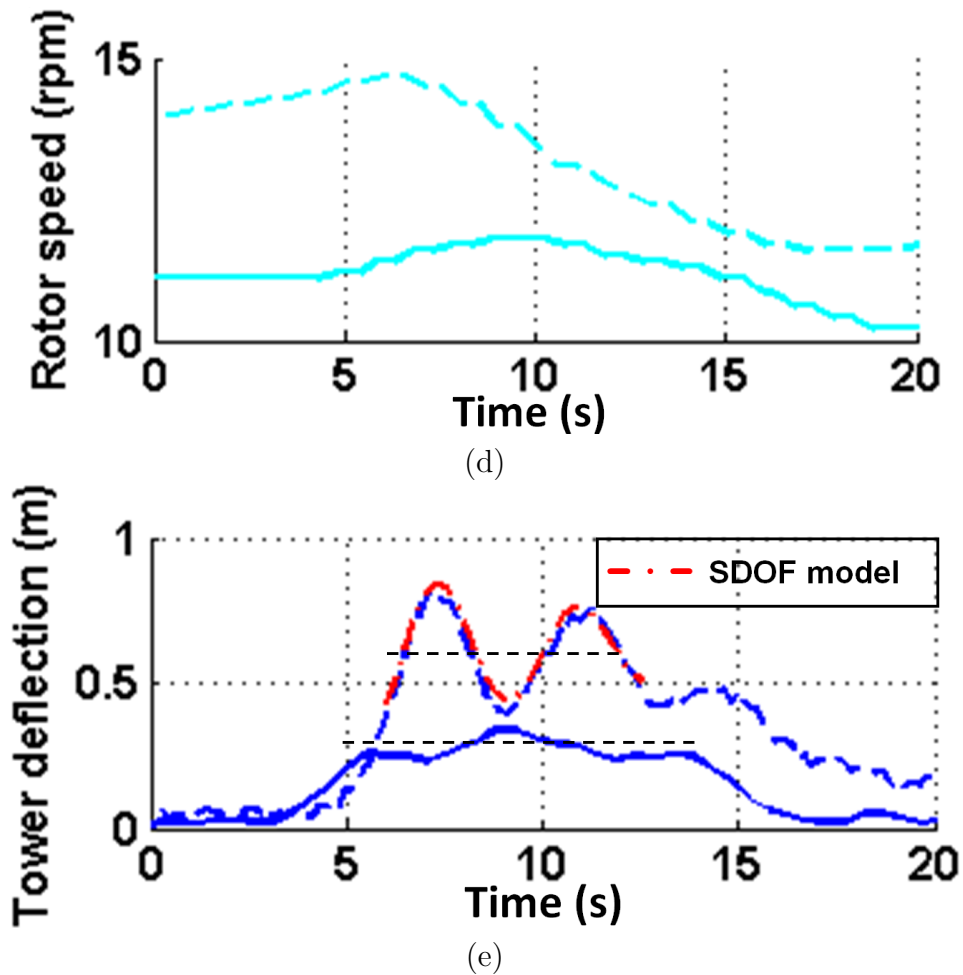


Figure 6.7: Time histories of: (a) hub height wind speed; (b) blade pitch angle (the blue dash-dot line is a quadratic fit); (c) generator torque (the blue dash-dot line is a linear fit); (d) rotor speed; and (e) tower tip deflection. The time histories are shown during transient power cut-off. Case 1, high-wind case, is shown with dashed lines. Case 2, low-wind case, is shown with solid lines. The red dash-dot line in Fig. 6.7e shows the predicted tower deflection from a free oscillation SDOF model.

Table 6.1: Comparison of turbine characteristics in the high-wind and low-wind cases.

	High wind	Low wind
Decrease in wind speed (%)	-35	-35
Amplitude of blade pitch (deg.)	14.9	9
Maximum blade pitching rate (deg./s)	4.4	2.2
Decrease in rotor torque (kNm/s)	-50	-46
Tower deflection from equilibrium (cm)	60	28
Amplitude of tower oscillations (cm)	21	negligible

dash-dot line in Fig. 6.7c is a linear fit to the rotor torque. Based on this linear fit, the rate of power reduction can be seen to occur at approximately the same rate for both the high-wind case ($-50kNm/s$) and the low-wind case ($-46kNm/s$). The imbalance between the aerodynamic and generator torques determines the rotational acceleration of the rotor; Fig. 6.7d shows that there is a twice as large rotational acceleration in the high-wind case ($-0.33rpm/s$) compared to the low-wind case ($-0.17rpm/s$). The larger imbalance accounts for the higher acceleration of the rotor in high-wind case. Table 6.1 summarises the characteristics of the two studied cases.

6.4 Tower deflections during normal operation

6.4.1 Power Spectrum Density (PSD) of tower deflection

Fig. 6.8 shows the PSD of the sideways deflections of the tower head during normal operation. The opto-mechanical measurement system is positioned $70m$ away from tower base of Turbine 11 and with an elevation angle of 52° of the laser in order to measure deflections at the tower head. The measurements during the time period when the rotor direction is perpendicular to the line-of-sight of the opto-mechanical platform are used in the data processing; as such the sideways deflections of tower head are measured. An 80-minute time series of tower head deflections is sampled at $500Hz$. The time series is divided into separate time windows and the PSD of tower head deflections is averaged over all time windows. The black dashed line shows a $-5/3$ slope; it can be seen that the PSD of tower deflections has the same slope as the PSD of turbulence, Fig. 6.3b, in the inertial sub-range of turbulence; in both PSD's the onset of this slope is the same. Two dominant peaks are visible in the PSD of tower deflections. The peak at $0.247Hz$ ($14.8rpm$) is related to the rotor rotation, and the peak at $0.273Hz$ is related to the first natural frequency of the tower's sideways bending. The range of rotor speeds, $0.150Hz - 0.248Hz$, is highlighted in green in the figure. The natural frequency is immediately above the range of rotor speeds and thus resonance of the tower's sideways bending is avoided during operation. The red

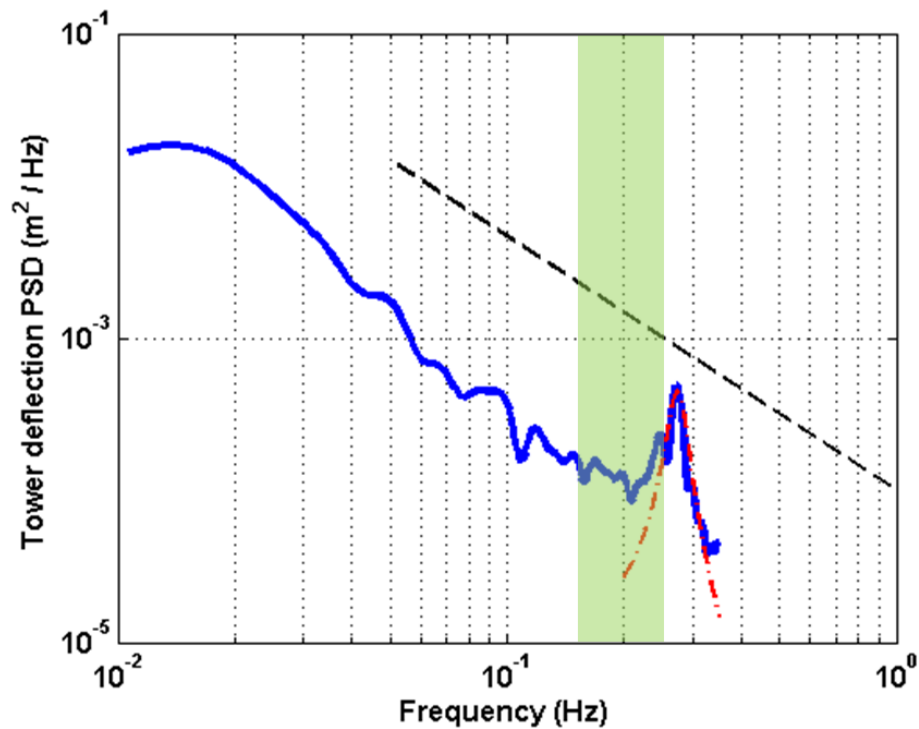


Figure 6.8: PSD of sideways tower deflections of tower head during normal operation. The black dashed line shows $-5/3$ slope corresponding to the inertial range of turbulence that is shown in Fig. 6.3. The red dash-dot line shows the response of a forced vibration SDOF model. The green highlighted area shows the range of rotor speeds.

dash-dot line is the frequency response derived from the forced vibration of SDOF model at the natural frequency of the tower that is used below to estimate the damping ratio of the tower during operation.

6.4.2 Impact of yaw misalignment on tower deflection

Fig. 6.9 shows the time histories of the nacelle direction, hub height wind direction and yaw misalignment that are measured over an 80-minute period. Following the convention used in literature [63,95], the yaw misalignment is given as the difference between the wind direction relative to North and the nacelle direction relative to North. The maximum yaw misalignment during the measurement period is 29° and the rms yaw misalignment is 7.9° . No sensitivity to the sign of yaw misalignment is observed, as the sign-averaged yaw misalignment is near zero, 0.4° . The observed yaw misalignment is of the same order as observed in [96]. The yawing of the wind turbine occurs at a rate of $0.4^\circ/s$. The averaging period in which the yaw actuator is triggered is a compromise between keeping the yaw misalignment small and minimizing the maintenance of the turbine's yaw system;

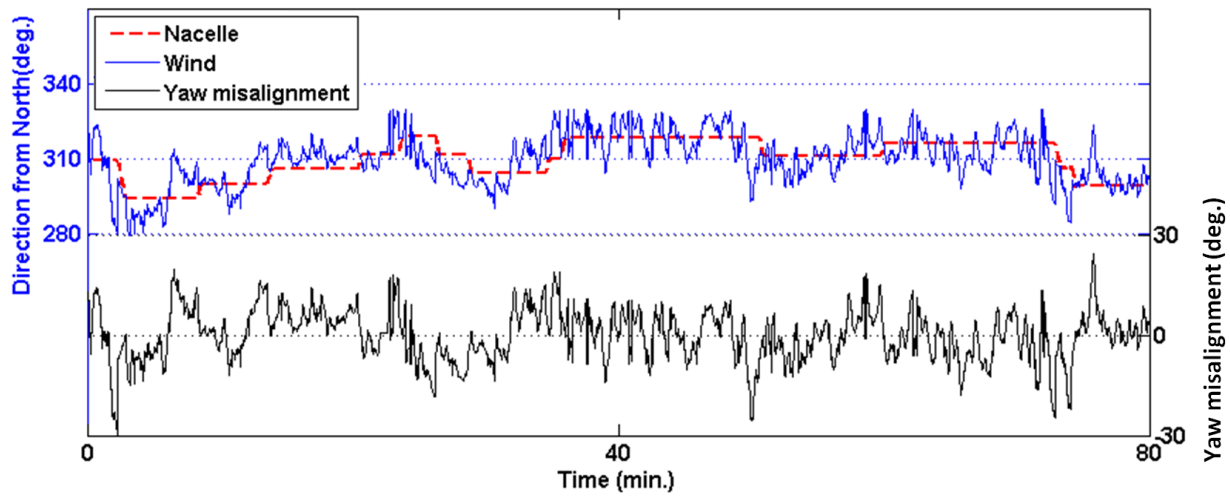


Figure 6.9: Time histories of nacelle direction, wind direction and yaw misalignment.

maintenance of a turbine's yaw system accounts for up to 13.3% of the total downtime of turbines [97].

Fig. 6.10a shows the amplitudes of the PSD of tower deflections at the first natural frequency as a function of yaw misalignment. The yaw misalignment is determined from 20s windows from $time = 36min$ to $time = 51min$ in the period that is shown in Fig. 6.9. Over this period the nacelle direction is 318.7° . For each window, the PSD of the tower deflections is calculated, and then the amplitude of the PSD at the first natural frequency is determined. In Fig. 6.10 the colour of the symbols corresponds to the measured hub height wind speed in the 20s windows. Larger tower deflections are observed for negative yaw misalignments, even though the wind speeds are of comparable magnitude for positive and negative yaw misalignments. There is negligible sensitivity of tower deflection to wind speed with positive yaw misalignment, whereas with negative yaw misalignment there are larger tower deflections at larger wind speeds. A link between yaw misalignment and structural loads has been addressed in other research [95,98] that solely uses computational methods. The monitoring of blade loads was suggested as an approach to detect yaw misalignment [98]. Also predictive models [95] show that below the rated wind speed, structural loads are reduced with positive yaw misalignment. To the author's knowledge, the present work is the first time that full-scale experiments verify the findings of the computational models. Fig. 6.10b shows the tower damping ratio determined over the same time windows as used in Fig. 6.10a. The damping ratio is derived from a forced vibration SDOF model, an example of which is shown by the red dash-dot line in Fig. 6.8. Unlike for tower deflections, no sensitivity of tower damping ratio to yaw misalignment and hub height wind speed is observed. The measured damping ratios range from 5.5% to 13.2%. Also shown with the red dashed line is the damping ratio during power cut-off; this

damping ratio is in the lower range of the damping ratios during operation. The larger aerodynamic damping during operation can account for the lower damping ratio during power cut-off.

6.4.3 Tower first harmonic of different wind turbines

Tower harmonics are one of the important modal parameters of a wind turbine's structure. The design convention is to avoid overlap of the tower's harmonics with the operational frequency range of turbine's rotor. Previously wind turbines of small size with high tower's harmonics were designed. The harmonics of such turbines are above the blade passage frequency (three times rotor frequency, $3P$) and hence resonance does not occur during the operation of the turbine. Such design methodology is called stiff design. Nevertheless, with the turbines growing in size and becoming less stiff, it is inevitable that the tower's first harmonic is designed below the blade passage frequency ($3P$) and above the rotor frequency (P); the so-called soft design of wind turbine's tower. For such turbines, resonance occurs during start-up of the turbine, when the blade passage frequency collides with the tower's first harmonic. An example of such behavior is observed in Fig. 5.7, at $time = 300s$, where high tower deflections are observed during start-up of the turbine. Soft design is a compromise between reducing structural deflection due to resonance and optimising the tower's mass, since designing the tower's first harmonic of multi-MW turbines to be above blade passage frequency ($3P$) requires designing massive turbine towers.

As another consequence of designing larger towers, the base diameter of wind turbine's tower increases above 4.3m, which is the limit for road transport [99]. Hence, for on-shore installation of wind turbines with large towers other solutions like hybrid towers are now considered. Such towers are made of concrete at low heights and steel at higher heights. The advantage of hybrid towers is that the large-diameter lower part of the towers is constructed at the site, which does not involve road-transport of large-sized items. The following results show how using hybrid towers influence first harmonic of towers.

The specifications of the turbines whose first tower's harmonic is measured in the present work are provided in Table 6.2. These turbines have hub heights ranging from 60m to 105m and are all designed according to the soft design methodology explained earlier. The rated power ranges from 2MW, for majority of the turbines, to 3.6MW, for the Siemens SWT3.6. As shown in the last column, the turbines have either steel towers or hybrid towers (steel and concrete). The first harmonic of the turbine's tower is measured using the opto-mechanical platform (Section 2.1.2). The first harmonic is the first peak above the rotor rotational frequency range in the PSD of tower tip deflection, as shown in Fig. 6.8. The first harmonic of the tower ranges from 0.22Hz to 0.52Hz, shown in Fig. 6.2. For turbines with steel tower, Turbines 1-6 in Fig. 6.11, there is a clear correlation between the hub height and tower's harmonic; that is designing taller towers results in lower harmonics.

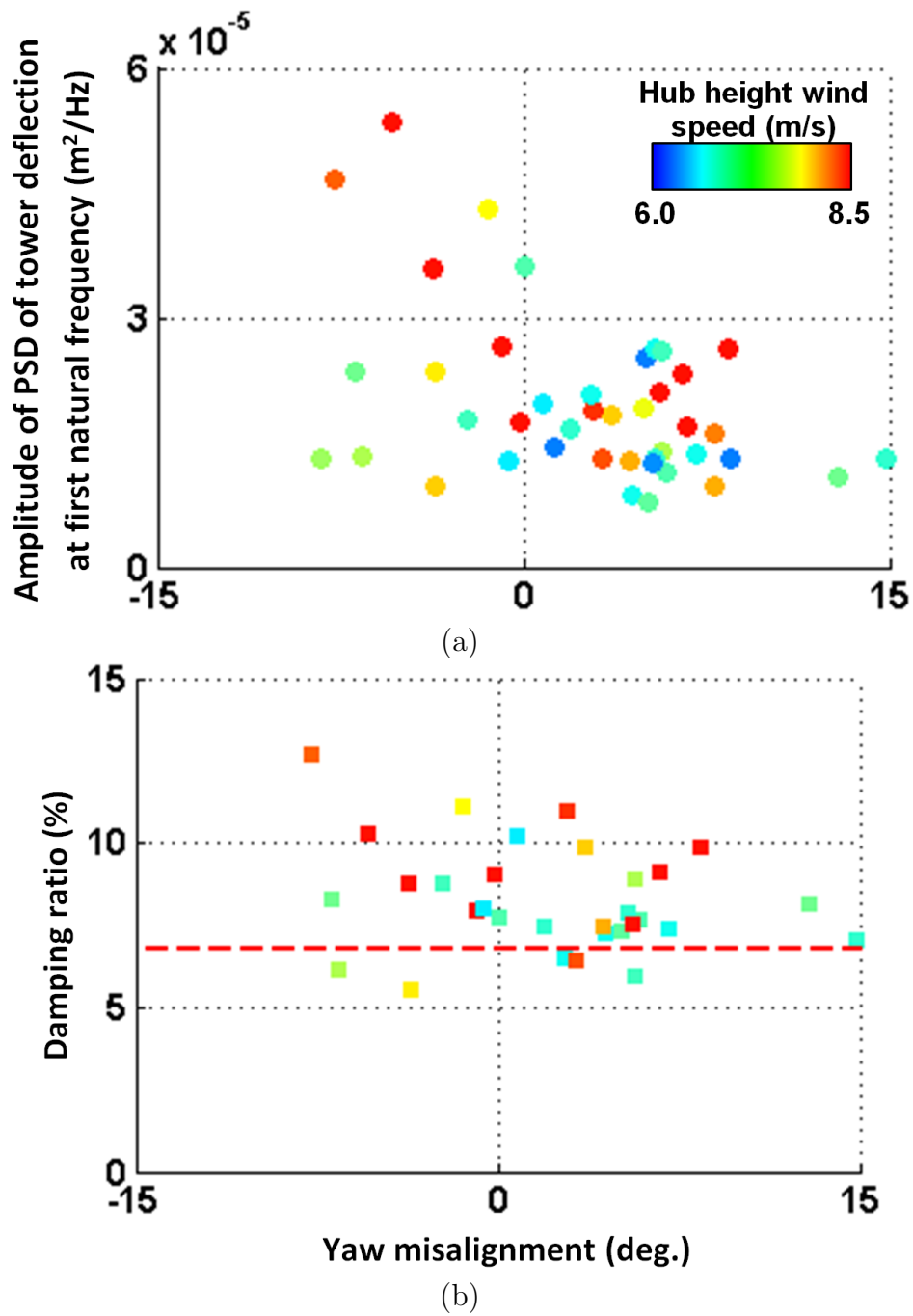


Figure 6.10: (a) Amplitude of tower deflections at the first natural frequency, and (b) damping ratio, as a function of yaw misalignment. The red dashed line in Fig. 6.10b shows the damping ratio during power cut-off.

Table 6.2: The turbines whose tower's first harmonic are shown in Fig. 6.11. Hybrid material is steel and concrete.

No.	Wind turbine	Rated power (MW)	Rotor diameter (m)	Hub height(m)	Tower material
1	Vestas V80	2	80	100	Steel
2	Vestas V90	3	90	105	Steel
3	Vestas V90	2	90	95	Steel
4	Siemens SWT3.6	3.6	107	93	Steel
5	Vestas V80	2	80	78	Steel
6	Vestas V80	2	80	60	Steel
7	Enercon E82	2	82	99	Hybrid
8	Enercon E70	2.3	71	85	Hybrid

Turbine 7 and 8 in Fig. 6.11 are of the hybrid type. The tower of Turbine 7, which is a 2MW Enercon E82, is made of concrete from base height to 74m (75% of total tower height) and steel from 74m to 99m (25% of total tower height). Turbine 1 (steel tower) and Turbine 7 (hybrid tower) have comparable hub heights. However it is observed that using concrete for the lower 75% of the tower of Turbine 7 results in approximately doubling the first harmonic of tower, as compared to Turbine 1. This observation shows that, in addition to solving the transport limitation for large-sized tower parts, using hybrid towers increases the first tower's harmonic, which makes it easier to avoid overlap of rotor frequency range and tower's first harmonic.

6.5 Concluding remarks

Positive rotor yaw misalignment can be used to alleviate loads on wind turbines during operation. Measurements showed that there is a 7.9° rms yaw misalignment between the nacelle and wind directions for a 2MW Vestas V90 turbine. It is shown that tower deflections are sensitive to yaw misalignments, as larger tower deflections are observed when the nacelle has negative yaw misalignment, compared to when the nacelle has positive yaw misalignment. To the author's knowledge, this is the first time that full-scale experiments verify the findings of computational models.

Measurements show that the damping ratio during a power cut-off event (6.8% for a 2MW Vestas V90) is in the lower range of the damping ratios during normal operation, 5.5% – 13.2%. Therefore load alleviation during transient power cut-off is of importance. Measurements show that during transition to power cut-off, power generation and the

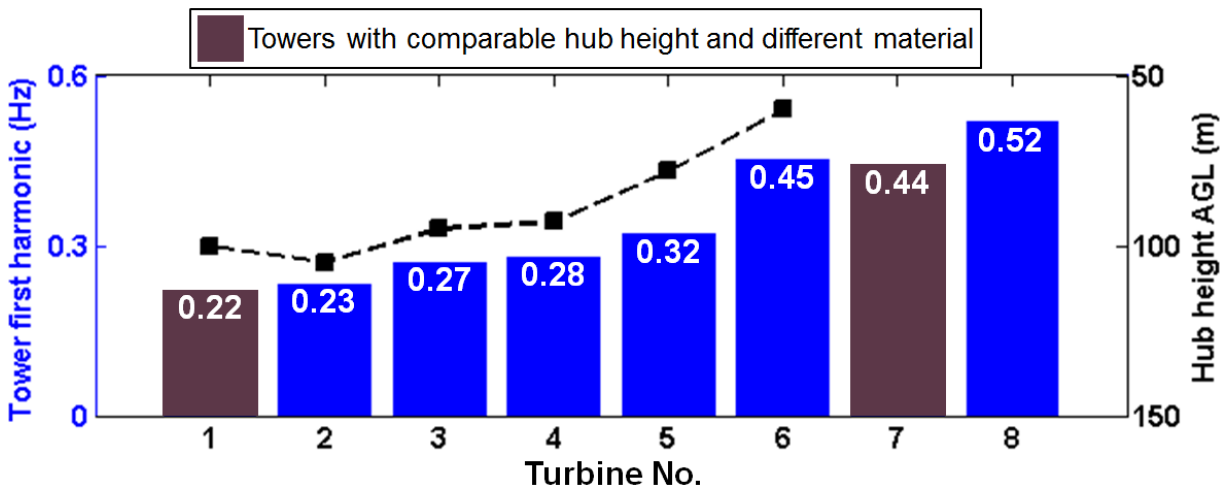


Figure 6.11: Tower's first harmonic for the turbines detailed in Table 6.2. Tower hub height is shown with the black dashed line. The right y-axis is shown in reverse direction.

corresponding torque on the tower head, account for the rapid decrease of oscillation amplitude from 60cm to 21cm during the first oscillational period.

Simultaneous measurements of the upstream turbulence, made with a scanning LiDAR system, show that due to the topography in complex terrain the turbulence intensity upstream of two turbines can vary up to 5%.

Chapter 7

Conclusions

7.1 Concluding remarks

In this thesis a mobile laboratory equipped with a 3D scanning LiDAR and an opto-mechanical platform for measuring structural deflections are integrated for field measurements in wind farms in flat and complex terrain. This novel approach is used to study the impact of environmental conditions on the performance of wind farms. The velocity recovery in wakes, power generation by wind turbines, structural loads and deflections of wind turbines are assessed in various environments. The experimental database is also used to assess the performance of CFD tools in predicting the flow field in the wind farm. The following are the specific findings of this study.

- Velocity recovery in the wake of a turbine operating in the undisturbed flow, single-wake, shows a fast recovery occurring in near-wake, from $1D$ to $3D$ downstream positions, followed by a slow recovery rate in far-wake, that is downstream of $3D$ position. Up to 72% of velocity recovery occurs in the near-wake. When the wake region is laterally exposed to the wake from upstream turbines, the so-called double-wake, velocity recovery occurs with slower rate. The fast recovery rate in the near-wake region of single-wake is not observed in the double-wake. In single-wake, velocity deficit reduces to 30% at $3D$ downstream position, whereas in double-wake, the same amount of reduction in velocity deficit occurs at $5D$ downstream position.
- CFD predictions of wind farm flow field are in satisfactory agreement with experimental observations. Comparisons of measured wind-farm-scale flow field with CFD predictions yield 6% rms difference upstream of turbines and 14% rms difference downstream of turbines. Excellent agreement with 3% rms difference between CFD and experiment was observed in the wake of a wind turbine operating in the undisturbed wind.

- Higher turbulence levels increase the fluctuations of the generated power at all wind speeds; where highest sensitivity is observed at wind speeds immediately below rated wind speed. Rough surface of canopies and complex terrain increases downstream turbulence intensity. Up to 15% higher turbulence intensity is observed downstream of forested fetch, as compared to unforested fetch. In complex terrain a local variation of 5% is observed due to different upstream terrain topology.
- Higher turbulence downstream of forest results in up to 4 times larger aeroelastic deflections on the tower of the turbine whose blades are feathered and 2.8 times larger deflections on the tower of turbine in normal operation. The higher turbulence levels and deflections downstream of forest is a potential reason for the observed higher maintenance requirements of wind turbine with forested fetch. An analysis of the maintenance log of the wind farm in forested terrain shows fault durations associated with the rotor, generator and hydraulics on the turbine in a forested fetch are 5.9, 2.1 and 2.4 times larger compared to the turbine in an unforested fetch.
- As regards the wind energy application, forest is a rough surface which causes modifications to atmospheric boundary layer and initiates velocity deficit and higher turbulence in the downstream wind flow field. A generalized semi-empirical model is developed to estimate impact of forested fetch on velocity deficit and power loss in every downstream position. The model predicts a velocity deficit of up to 8.5% at $5H_{forest}$ downstream position. The predictions of the model underestimate the velocity-equivalent power deficit of an actual wind turbine at $45H_{forest}$ downstream position by 4.1%. The power loss occurring due to sheared inflow and higher turbulence can account for the underestimation of the power deficit by the model. Observations show that the power loss of downstream turbine increases with the streamwise extent of forest for streamwise extents smaller than $100H_{forest}$, whereas no particular correlation was observed for forest extents longer than $100H_{forest}$.
- Analysis of long-term SCADA data of wind farms in forested and unforested terrain shows that forested fetch can cause power deficit of up to 30% for the downstream turbines. Turbines in forested area show up to 2 times higher power curve scatter. On the other hand, Power losses due to wakes are observed to be lower in forested terrain compared to unforested terrain. The smaller wake losses are attributed to higher mixing and faster recovery due to the elevated turbulence levels downstream of the forest. This hypothesis is verified by CFD simulations of wake recovery.
- Damping ratio of 6.8% in tower vibrations is measured during power cut-off of a 2MW Vestas V90, which is in the lower range of the damping ratios during normal operation, 5.5% – 13.2%. Therefore load alleviation during transient power cut-off is of importance. During transition to power cut-off, oscillational deflection of tower head is observed. The amplitude of the oscillational deflections decreases to one third in the first oscillation. Power generation and the attendant torque on the tower head

accounts for this rapid decrease during first oscillation.

- Positive rotor yaw misalignment can be used to alleviate loads on wind turbines during operation. Measurements showed that there is a 7.9° rms yaw misalignment between the nacelle and wind directions for a 2MW Vestas V90 turbine. It is shown that tower deflections are sensitive to yaw misalignments, as larger tower deflections are observed when the nacelle has negative yaw misalignment, compared to when nacelle has positive yaw misalignment.

7.2 Future work

The opto-mechanical platform can be used in detecting blade icing of wind turbines. It is estimated that 20% loss of power occurs due to blade icing. 25% of the global wind market is in the cold climate, where wind turbines' blades are prone to icing in the cold months of the year [100]. Also in Swiss largest wind farm, Juvent, blade icing is a major detrimental phenomenon. Manufacturing and tuning an efficient blade de-icing system requires a full-scale ice-detection instrument. As wind turbine manufacturers are developing and testing their first prototypes of blade de-icing systems, such usage of the opto-mechanical platform has the potential to attract industrial attentions as well.

WindRoverII is readily deployable in various measurement sites. This potential can be used to further investigate the impact of various topological features in a complex terrain on the upstream and downstream flow field. Full-scale experiments, and supplementary wind tunnel tests, can result in a semi-empirical model of complex terrain. Such models can be used to predict the impact of terrain on the annual energy yield of the new wind farms.

In addition to short-term measurements using windRoverII, the system can be modified to enable long-term LiDAR measurements. This involves enhancement of security measures and remote connectivity of the system to control and operate the sub-systems of windRoverII by a remote user. Long-term measurements detail seasonal impact of upstream conditions, such as forests, on the wind flow field. A design review of windRoverII in future can consider two separate areas for the crew and for the LiDAR and the generator.

Measurements with dual opto-mechanical platforms can provide simultaneous calculation of fore-aft and sideways deflections. This capability details the impact of forested fetch on the thrust force and torque moment on the rotor. Using dual opto-mechanical platforms also extends the possible wind direction range for ice-detection measurements mentioned earlier.

Experimental results show that in compact wind farms, the wind flow distribution around a wind turbine is not uniform. It was observed that such non-uniform flow distribution impacts the velocity recovery rate in the wake. The boundary conditions of the

Immersed Wind Turbine Model (IWTM) of the CFD tool MULTI3 can be modified to adjust to the circumferential and axial non-uniform distribution of velocity in such cases.

Bibliography

- [1] G. Koçer, *Full-scale wind turbine flow field measurements using an instrumented uninhabited aerial vehicle*. PhD thesis, ETH Zurich, 2012.
- [2] A. A. Townsend, “Self-preserving flow inside a turbulent boundary layer,” *Journal of Fluid Mechanics*, vol. 22, p. 773, aug 1965.
- [3] “Global Wind Statistics,” tech. rep., Global Wind Energy Council, 2014.
- [4] R. J. Barthelmie, S. T. Frandsen, M. N. Nielsen, S. C. Pryor, P.-E. Rethore, and H. E. Jørgensen, “Modelling and measurements of power losses and turbulence intensity in wind turbine wakes at Middelgrunden offshore wind farm,” *Wind Energy*, vol. 10, pp. 517–528, nov 2007.
- [5] B. Sanderse, “Aerodynamics of wind turbine wakes: Literature review,” *Energy research Centre of the Netherlands*, pp. 1–46, 2009.
- [6] S. Jafari, N. Chokani, and R. S. Abhari, “Simulation of Wake Interactions in Wind Farms Using an Immersed Wind Turbine Model,” *Journal of Turbomachinery*, vol. 136, p. 061018, nov 2013.
- [7] R. Lanzafame, S. Mauro, and M. Messina, “Wind turbine CFD modeling using a correlation-based transitional model,” *Renewable Energy*, vol. 52, pp. 31–39, 2013.
- [8] R. J. Stevens, J. Graham, and C. Meneveau, “A concurrent precursor inflow method for Large Eddy Simulations and applications to finite length wind farms.” 2014.
- [9] A. Singh and R. Giannoulakis, S., Chokani, N., Abhari, “Large-Area Identification of Wind Farms and Optimization of Turbine Layout,” in *European Wind Energy Conference EWEA 2013*, (Vienna, Austria), 2013.

-
- [10] J. S. González, A. G. Gonzalez Rodriguez, J. C. Mora, J. R. Santos, and M. B. Payan, "Optimization of wind farm turbines layout using an evolutive algorithm," *Renewable Energy*, vol. 35, no. 8, pp. 1671–1681, 2010.
- [11] Y. Eroglu and S. U. Seckiner, "Wind farm layout optimization using particle filtering approach," *Renewable Energy*, vol. 58, pp. 95–107, 2013.
- [12] B. Pérez, R. Mínguez, and R. Guanche, "Offshore wind farm layout optimization using mathematical programming techniques," *Renewable Energy*, vol. 53, pp. 389–399, 2013.
- [13] A. Singh, F. Wolff, N. Chokani, and R. S. Abhari, "Optimizing Synergy of Utility-Scale Wind and Pumped-Hydro Storage," in *ASME Turbo Expo 2013*, (Texas, USA), ASME, 2013.
- [14] Caithness Windfarm Information Forum, "<http://www.caithnesswindfarms.co.uk/AccidentStatistics>," 2015.
- [15] P. Jamieson and G. Hassan, *Innovation in wind turbine design*. Wiley, 2011.
- [16] Windpower Monthly, "10 big wind turbines," 2014.
- [17] M. Zendehbad, N. Chokani, and R. S. Abhari, "Impact of forested fetch on energy yield and maintenance of wind turbines," *Renewable Energy*, vol. 96, pp. 548–558, 2016.
- [18] W. Carswell, J. Johansson, F. Løvholt, S. Arwade, C. Madshus, D. DeGroot, and A. Myers, "Foundation damping and the dynamics of offshore wind turbine monopiles," *Renewable Energy*, vol. 80, pp. 724–736, 2015.
- [19] T. Ashuri, M. Zaaier, J. Martins, G. van Bussel, and G. van Kuik, "Multidisciplinary design optimization of offshore wind turbines for minimum levelized cost of energy," *Renewable Energy*, vol. 68, pp. 893–905, aug 2014.
- [20] L. P. Chamorro and F. Porté-Agel, "A Wind-Tunnel Investigation of Wind-Turbine Wakes: Boundary-Layer Turbulence Effects," *Boundary-Layer Meteorology*, vol. 132, pp. 129–149, jul 2009.
- [21] D. Medici and G. Goretti, "Wake Influence of V44 Wind Turbines on the Field Measurement of an 80m Mast in Italy," in *Wake Conference*, (Visby, Sweden), 2011.
- [22] W. Zhang, C. D. Markfort, and F. Porté-Agel, "Wind-Turbine Wakes in a Convective Boundary Layer: A Wind-Tunnel Study," *Boundary-Layer Meteorology*, vol. 146, pp. 161–179, feb 2013.

- [23] G. V. Iungo, Y.-T. Wu, F. Porté-Agel, G. V. Iungo, Y.-T. Wu, and F. Porté-Agel, "Field Measurements of Wind Turbine Wakes with Lidars," *Journal of Atmospheric and Oceanic Technology*, vol. 30, pp. 274–287, feb 2013.
- [24] S. Lang and E. McKeogh, "LIDAR and SODAR measurements of wind speed and direction in upland terrain for wind energy purposes," *Remote Sensing*, vol. 3, no. 9, pp. 1871–1901, 2011.
- [25] T. Mikkelsen, S. Knudsen, M. Sjöholm, N. Angelou, and A. Tegtmeier, "WindScanner.eu -a new Remote Sensing Research Infrastructure for On-and Offshore Wind Energy," in *International Conference on Wind Energy: Materials, Engineering and Policies WEMEP2012*, (Hyderabad, India), pp. KNL-3, 2012.
- [26] J. Mann, J.-P. Cariou, M. S. Courtney, R. Parmentier, T. Mikkelsen, R. Wagner, P. Lindelöw, M. Sjöholm, and K. Enevoldsen, "Comparison of 3D turbulence measurements using three staring wind lidars and a sonic anemometer," *IOP Conference Series: Earth and Environmental Science*, vol. 1, p. 012012, may 2008.
- [27] S. Drechsel, G. J. Mayr, M. Chong, M. Weissmann, A. Dörnbrack, R. Calhoun, S. Drechsel, G. J. Mayr, M. Chong, M. Weissmann, A. Dörnbrack, and R. Calhoun, "Three-Dimensional Wind Retrieval: Application of MUSCAT to Dual-Doppler Lidar," *Journal of Atmospheric and Oceanic Technology*, vol. 26, pp. 635–646, mar 2009.
- [28] B. D. Hirth, J. L. Schroeder, B. D. Hirth, and J. L. Schroeder, "Documenting Wind Speed and Power Deficits behind a Utility-Scale Wind Turbine," *Journal of Applied Meteorology and Climatology*, vol. 52, pp. 39–46, jan 2013.
- [29] K. Fredriksson, B. Galle, K. Nyström, and S. Svanberg, "Mobile lidar system for environmental probing," *Applied optics*, vol. 20, pp. 4181–9, dec 1981.
- [30] O. Uchino and I. Tabata, "Mobile lidar for simultaneous measurements of ozone, aerosols, and temperature in the stratosphere.," *Applied optics*, vol. 30, pp. 2005–12, may 1991.
- [31] P. Weibring, H. Edner, and S. Svanberg, "Versatile mobile lidar system for environmental monitoring.," *Applied optics*, vol. 42, pp. 3583–94, jun 2003.
- [32] N. Haala, M. Peter, J. Kremer, and G. Hunter, "Mobile LiDAR Mapping for 3D Point Cloud Collection in Urban Areas – a Performance Test," in *21st International Society for Photogrammetry and Remote Sensing Congress*, (Beijing, China), pp. 1119–1124, 2008.

-
- [33] R. H. Shaw and U. Schumann, "Large-eddy simulation of turbulent flow above and within a forest," *Boundary-Layer Meteorology*, vol. 61, pp. 47–64, oct 1992.
- [34] S. Dupont and Y. Brunet, "Coherent structures in canopy edge flow: a large-eddy simulation study," *Journal of Fluid Mechanics*, vol. 630, p. 93, jul 2009.
- [35] C. Frank and B. Ruck, "Numerical study of the airflow over forest clearings," *Forestry*, vol. 81, pp. 259–277, jul 2008.
- [36] Z. Ahmadi Zeleti, S. Aubrun, and J. Hämäläinen, "Porous Medium Modeling for Air Flow Through Forest - Comparison with Wind Tunnel Data," in *11th World Congress on Computational Mechanics*, (Barcelona), 2014.
- [37] Ylva Odemark and Antonio Segalini, "The effects of a model forest canopy on the outputs of a wind turbine model," *J. Phys.: Conf. Ser.*, vol. 555, p. 012079.
- [38] A. Segalini, J. H. M. Fransson, and P. H. Alfredsson, "Scaling Laws in Canopy Flows: A Wind-Tunnel Analysis," *Boundary-Layer Meteorology*, vol. 148, pp. 269–283, aug 2013.
- [39] H. S. Pedersen and W. Langreder, "Forest - added Turbulence: A parametric study on Turbulence intensity in and around forests," *J. Phys.: Conf. Ser.*, vol. 75, p. 012062, 2007.
- [40] E. Dellwik, F. Bingöl, and J. Mann, "Flow distortion at a dense forest edge," *Quarterly Journal of the Royal Meteorological Society*, vol. 140, pp. 676–686, jan 2014.
- [41] J. Mann and E. Dellwik, "Sudden distortion of turbulence at a forest edge," *Journal of Physics: Conference Series*, vol. 524, p. 012103, jun 2014.
- [42] D. Vickers and C. K. Thomas, "Some aspects of the turbulence kinetic energy and fluxes above and beneath a tall open pine forest canopy," *Agricultural and Forest Meteorology*, vol. 181, pp. 143–151, 2013.
- [43] J. Mann, E. Dellwik, F. Bingöl, and O. Rathmann, "Laser measurements of flow over a forest," *J. Phys.: Conf. Ser.*, vol. 75, p. 010257, 2007.
- [44] E. Dellwik, J. Mann, and F. Bingöl, "Flow tilt angles near forest edges – Part 2: Lidar anemometry," *Biogeosciences*, vol. 7, pp. 1759–1768, may 2010.
- [45] K. Traumner, A. Wieser, B. Ruck, C. Frank, L. Rohner, and C. Kottmeier, "The suitability of Doppler lidar for characterizing the wind field above forest edges," *Forestry*, vol. 85, pp. 399–412, jul 2012.

-
- [46] F. Kanani, K. Träumner, B. Ruck, and S. Raasch, “What determines the differences found in forest edge flow between physical models and atmospheric measurements? - An LES study,” vol. 23, no. 1, pp. 33–49, 2014.
- [47] A. Chougule, J. Mann, A. Segalini, and E. Dellwik, “Spectral tensor parameters for wind turbine load modeling from forested and agricultural landscapes,” *Wind Energy*, vol. 18, pp. 469–481, mar 2015.
- [48] D.-P. Molenaar, “Experimental Modal Analysis of a 750 kW Wind Turbine for Structural Model Validation,” in *ASME 2003 Wind Energy Symposium*, pp. 332–339, ASME, 2003.
- [49] D. T. Griffith, R. L. Mayes, and P. S. Hunter, “Excitation Methods for a 60 kW Vertical Axis Wind Turbine,” pp. 329–338, Springer New York, 2011.
- [50] R. Osgood, G. Bir, H. Mutha, B. Peeters, M. Luczak, and G. Sablon, “Full-scale modal wind turbine tests: comparing shaker excitation with wind excitation,” pp. 113–124, Springer New York, 2011.
- [51] M. H. Hansen, K. Thomsen, P. Fuglsang, and T. Knudsen, “Two methods for estimating aeroelastic damping of operational wind turbine modes from experiments,” *Wind Energy*, vol. 9, pp. 179–191, jan 2006.
- [52] G. H. James, T. G. Carne, and P. S. Veers, “Damping Measurements Using Operational Data,” *Journal of Solar Energy Engineering*, vol. 118, no. 3, p. 190, 1996.
- [53] M. Ozbek and D. Rixen, “Operational Modal Analysis of a 2.5MW Wind Turbine Using Optical Measurement Techniques and Strain Gauges,” *Wind Energy*, vol. 16, pp. 367–381, apr 2013.
- [54] M. Ozbek, D. J. Rixen, and T. W. Verbruggen, “Remote monitoring of wind turbine dynamics by laser interferometry: Phase1,” in *Proceedings of the IMAC-XXVII*, (Florida, USA), 2009.
- [55] M. Ozbek, D. J. Rixen, O. Erne, and G. Sanow, “Feasibility of monitoring large wind turbines using photogrammetry,” *Energy*, vol. 35, no. 12, pp. 4802–4811, 2010.
- [56] A. Jain, G. Schildbach, L. Fagiano, and M. Morari, “On the design and tuning of linear model predictive control for wind turbines,” *Renewable Energy*, vol. 80, pp. 664–673, 2015.
- [57] E. A. Bossanyi, “Individual Blade Pitch Control for Load Reduction,” *Wind Energy*, vol. 6, pp. 119–128, apr 2003.

-
- [58] E. A. Bossanyi, "Wind Turbine Control for Load Reduction," *Wind Energy*, vol. 6, pp. 229–244, jul 2003.
- [59] M. Zhang, B. Tan, and J. Xu, "Parameter study of sizing and placement of deformable trailing edge flap on blade fatigue load reduction," *Renewable Energy*, vol. 77, pp. 217–226, 2015.
- [60] S. J. Johnson, J. P. Baker, C. P. van Dam, and D. Berg, "An overview of active load control techniques for wind turbines with an emphasis on microtabs," *Wind Energy*, vol. 13, pp. 239–253, mar 2010.
- [61] X. Lachenal, S. Daynes, and P. M. Weaver, "Review of morphing concepts and materials for wind turbine blade applications," *Wind Energy*, vol. 16, pp. 283–307, mar 2013.
- [62] M. Harris, D. J. Bryce, A. S. Coffey, D. A. Smith, J. Birkemeyer, and U. Knopf, "Advance measurement of gusts by laser anemometry," *Journal of Wind Engineering and Industrial Aerodynamics*, vol. 95, no. 12, pp. 1637–1647, 2007.
- [63] C. Kress, N. Chokani, and R. Abhari, "Downwind wind turbine yaw stability and performance," *Renewable Energy*, vol. 83, pp. 1157–1165, 2015.
- [64] J.-W. Lee, J.-H. Han, H.-K. Shin, and H.-J. Bang, "Active load control of wind turbine blade section with trailing edge flap: Wind tunnel testing," *Journal of Intelligent Material Systems and Structures*, vol. 25, pp. 2246–2255, dec 2014.
- [65] M. Bastankhah and F. Porté-Agel, "A wind-tunnel investigation of wind-turbine wakes in yawed conditions," *Journal of Physics: Conference Series*, vol. 625, no. 1, p. 012014, 2015.
- [66] IEC61400-1, "Wind turbines – Part I: Design Requirements," 2005.
- [67] M. Mansour, T. Schmid, N. Chokani, and R. Abhari, "Power Curve Assessment of a 2MW Wind Turbine Located in Complex Terrain," in *European Wind Energy Conference EWEA2014*, (Barcelona, Spain), 2014.
- [68] K. Ettl, M. Mansour, B. Subramanian, D. Costa, N. Chokani, and R. S. Abhari, "Near-Wake Measurements in an Offshore Reference Field Using a Kite-Borne Aerodynamic-Probe-System," in *European Wind Energy Association Annual Event 2013*, (Vienna, Austria), 2013.
- [69] H. A. Panofsky and J. A. J. A. Dutton, *Atmospheric turbulence : models and methods for engineering applications*. Wiley, 1984.

- [70] A. Crespo and J. Hernandez, "Turbulence characteristics in wind-turbine wakes," *Journal of Wind Engineering and Industrial Aerodynamics*, vol. 61, no. 1, pp. 71–85, 1996.
- [71] J. Cleijne, "Results of Sexbierum Wind Farm: single wake measurements," tech. rep., TNO Milieu Energie en Procesinnovatie, Apeldoorn, the Netherlands, 1993.
- [72] R. Gómez-Elvira, A. Crespo, E. Migoya, F. Manuel, and J. Hernández, "Anisotropy of turbulence in wind turbine wakes," *Journal of Wind Engineering and Industrial Aerodynamics*, vol. 93, no. 10, pp. 797–814, 2005.
- [73] T. Arakawa and K. Yamamoto, "Frequencies and Damping Ratios of a High Rise Building Based on Microtremor Measurement," in *13th World Conference on Earthquake Engineering*, (Vancouver, Canada), 2004.
- [74] A. Kammerer and R. S. Abhari, "Experimental Study on Impeller Blade Vibration During Resonance—Part II: Blade Damping," *Journal of Engineering for Gas Turbines and Power*, vol. 131, no. 2, p. 022509, 2009.
- [75] M. Novak and L. El Hifnawy, "Damping of structures due to soil-structure interaction," *Journal of Wind Engineering and Industrial Aerodynamics*, vol. 11, no. 1, pp. 295–306, 1983.
- [76] T. Behr, A. I. Kalfas, and R. S. Abhari, "A probabilistic uncertainty evaluation method for turbomachinery probe measurements," in *Symposium on Measuring Techniques in Turbomachinery. Transonic and Supersonic Flow in Cascades and Turbo-machines*, (Thessaloniki, Greece), 2006.
- [77] S. Jafari, *Efficient Simulation of Wind and Wake Flows in Wind Farms Using a Preconditioned Multistage Solver*. PhD thesis, ETH Zurich, 2014.
- [78] C. Kress, *Downwind Wind Turbine Performance, Loading and Design Considerations*. PhD thesis, ETH Zurich, 2016.
- [79] G. Kocer, M. Mansour, N. Chokani, R. Abhari, and M. Mueller, "Full-Scale Wind Turbine Near-Wake Measurements Using an Instrumented Uninhabited Aerial Vehicle," *Journal of Solar Energy Engineering*, vol. 133, no. 4, p. 041011, 2011.
- [80] M. Mansour, G. Kocer, C. Lenherr, N. Chokani, and R. S. Abhari, "Seven-Sensor Fast-Response Probe for Full-Scale Wind Turbine Flowfield Measurements," *Journal of Engineering for Gas Turbines and Power*, vol. 133, no. 8, p. 081601, 2011.

-
- [81] C. T. Loraux and E. Brühwiler, “Realistic examination of the fatigue life of a wind turbine tower using data from long term monitoring,” in *IABSE Conference*, (Geneva, Switzerland), 2015.
- [82] C. Tsalicoglou, S. Jafari, N. Chokani, and R. S. Abhari, “RANS Computations of MEXICO Rotor in Uniform and Yawed Inflow,” *Journal of Engineering for Gas Turbines and Power*, vol. 136, p. 011202, oct 2013.
- [83] P. A. Fleming, P. M. O. Gebraad, S. Lee, J. W. van Wingerden, K. Johnson, M. Churchfield, J. Michalakes, P. Spalart, and P. Moriarty, “Evaluating techniques for redirecting turbine wakes using SOWFA,” *Renewable Energy*, vol. 70, no. June, pp. 211–218, 2014.
- [84] C. Kress, S. Barber, N. Chokani, and R. S. Abhari, “Improved Modeling of Wakes: Experimental Study and Experimentally- Anchored Model; EWEA Offshore Conference,” in *EWEA Offshore Conference*, (Amsterdam, Netherlands), 2011.
- [85] GWEC, “Global Wind Report 2015 | Gwec,” tech. rep., Global Wind Energy Council, 2016.
- [86] R. S. Abhari, N. Chokani, A. Gawlikowska, A. Ioannou, A. Singh, B. Subramanian, J. Vinklers, and M. Zendehbad, “Systematic Planning for Development of Wind Energy in Lubelskie, Poland,” Tech. Rep. July, ETH Zurich, 2014.
- [87] Forestry Agency, “Annual Report on Forest and Forestry in Japan,” tech. rep., Ministry of Agriculture, Forestry and Fisheries, Tokyo, Japan, 2014.
- [88] E. Dimitrova, J. Vinklers, N. Chokani, and R. S. Abhari, “Integrated Biomass Assessment and Optimized Power Generation,” *Energy Technology*, vol. 3, pp. 265–278, mar 2015.
- [89] LP DAAC courtesy of the U.S. Geological Survey, “LP DAAC :: NASA Land Data Products and Services.”
- [90] R. B. Stull, ed., *An Introduction to Boundary Layer Meteorology*. Dordrecht: Springer Netherlands, 1988.
- [91] M. Zendehbad, N. Chokani, and R. S. Abhari, “Experimental Study of Aero-Mechanical Damping of Full-Scale Wind Turbines,” in *Proceedings of ASME Turbo Expo 2014*, (Dusseldorf, Germany), pp. 1–12, 2014.
- [92] S. Wharton and J. Lundquist, “Atmospheric stability impacts on power curves of tall wind turbines—an analysis of a west coast north american wind farm,” *Lawrence Livermore National Laboratory*, p. 73, 2010.

-
- [93] B. Ernst, Y. Wan, and B. Kirby, "Short-Term Power Fluctuation of Wind Turbines: Analyzing Data from the German 250-MW Measurement Program from the Ancillary Services Viewpoint," in *Windpower '99 Conference*, (Burlington, Vermont), 1999.
- [94] B. Hodge, K. Orwig, and M. Milligan, "Examining Information Entropy Approaches as Wind Power Forecasting Performance Metrics," in *12 th International Conference on Probabilistic Methods Applied to Power Systems*, (Istanbul, Turkey), 2012.
- [95] K. A. Kragh and M. H. Hansen, "Load alleviation of wind turbines by yaw misalignment," *Wind Energy*, vol. 17, pp. 971–982, jul 2014.
- [96] T. Mikkelsen, N. Angelou, K. Hansen, M. Sjöholm, M. Harris, C. Slinger, P. Hadley, R. Scullion, G. Ellis, and G. Vives, "A spinner-integrated wind lidar for enhanced wind turbine control," *Wind Energy*, vol. 16, pp. 625–643, may 2013.
- [97] J. Ribrant and L. M. Bertling, "Survey of Failures in Wind Power Systems With Focus on Swedish Wind Power Plants During 1997–2005," *IEEE Transactions on Energy Conversion*, vol. 22, pp. 167–173, mar 2007.
- [98] C. Bottasso and C. Riboldi, "Estimation of wind misalignment and vertical shear from blade loads," *Renewable Energy*, vol. 62, pp. 293–302, 2014.
- [99] J. Cotrell, T. Stehly, J. Johnson, J. O. Roberts, Z. Parker, G. Scott, and D. Heimiller, "Analysis of Transportation and Logistics Challenges Affecting the Deployment of Larger Wind Turbines: Summary of Results," tech. rep., National Renewable Energy Laboratory, 2014.
- [100] Windpower Monthly, "Vestas reveals de-icing system," 2013.

A. Nomenclature

Letters and symbols

C_{sc}	scaling coefficient
C_{tr}	turbulent coefficient
D	rotor diameter
F	disturbance function above forest
f	frequency
G	disturbance function downstream of forest
H	transfer function
H_{hub}	hub height
h	height
h_0	reference height
H_{forest}	tree height
k	spring coefficient
L_0	height of undisturbed zone
P	rotor frequency
t	time
TI	turbulence intensity
U	wind speed
U_0	reference wind speed
u', v', w'	wind speed fluctuations in principal, lateral and vertical direction
u_{ref}	reference wind speed
$U_{undisturbed}$	undisturbed wind speed
x, y, z	coordinates in streamwise, lateral and vertical direction
$X(\omega)$	forcing function
$Y(\omega)$	response function
z_0, z_1	roughness length of rough and smooth surface
α	power law exponent
γ	heading angle
κ	Karman constant
ζ	damping ratio
θ	beam elevation
θ_0	phase angle

ν_0	friction velocity
φ	beam azimuth
ω	frequency
ω_n	natural frequency

Abbreviations

2D	two dimensional
3D	three dimensional
AEY	annual energy yield
AGL	above ground level
CFD	computational fluid dynamics
DA	degree of anisotropy
GPS	global positioning system
IMU	inertial measurement unit
IWTM	immersed wind turbine model
LAI	leaf area index
LEC	Laboratory for Energy Conversion
LiDAR	light detection and ranging
LOS	line-of-sight
NACA	National Advisory Committee for Aeronautics
NREL	National Renewable Energy Laboratory
PPI	plan position indicator
PSD	power spectrum density
RANS	Reynolds-averaged Navier-Stokes
RMS	root mean square
SCADA	supervisory control and data acquisition
SDOF	single degree of freedom
SODAR	sound detecting and ranging
STFT	short-time Fourier transform
TI	turbulence intensity
TKE	turbulent kinetic energy
VAD	velocity azimuth display

B. List of publications

a) Journal publication:

- **Zendeabad, M.**, Chokani, N., Abhari, R.S., 2016, "Volumetric Three-Dimensional Wind Measurement Using a Single Mobile-Based LiDAR," *Journal of Solar Energy Engineering*, **138**, p.011003.
- **Zendeabad, M.**, Chokani, N., Abhari, R.S., 2016, "Impact of Forested Fetch on Energy Yield and Maintenance of Wind Turbines," *Renewable Energy*, **96**, pp. 548-558.
- Kazda, J., **Zendeabad, M.**, Jafari, S., Chokani, N., Abhari, R.S., 2016, "Mitigating Adverse Wake Effects in a Wind Farm Using Non-optimum Operational Conditions," *Journal of Wind Engineering and Industrial Aerodynamics*, **154**, pp. 76-83.
- **Zendeabad, M.**, Kazda, J., Chokani, N., Abhari, R.S., 2015, "Impact of Turbulence-Elevated Wind Flow on Wind Power Extraction," *International Journal of Gas Turbine, Propulsion and Power Systems (JGPP)*, *In press*. Also presented in *Proceedings of IGTC2015*, Tokyo, Japan.

b) Publication recently submitted:

- **Zendeabad, M.**, Chokani, N., Abhari, R.S., "Measurements of Tower Deflection on Full-Scale Wind Turbine Using Opto-Mechanical Platform", *Journal of Wind Engineering and Industrial Aerodynamics*, under review.

c) Conference proceedings:

- **Zendeabad, M.**, Chokani, N., Abhari, R.S., 2016, "Wind-Farm-Scale Measurements Using Mobile-Based LiDAR," *WindEurope Summit 2016*, Hamburg, Germany.
- **Zendeabad, M.**, Chokani, N., Abhari, R.S., 2015, "Multi-Scale Measurements in Wind Farm in Complex and Flat Terrain," *Proceedings of ASME Turbo Expo 2015*, Montreal, Canada.
- **Zendeabad, M.**, Chokani, N., Abhari, R.S., 2015, "Mobile LiDAR Mapping of Utility-Scale Wind Farms," *Proceedings of DEWEK2015*, Bremen, Germany.

- **Zendehbad, M.**, Chokani, N., Abhari, R.S., 2014, "Experimental Study of Aero-mechanical Damping of Full-Scale Wind Turbines," *Proceedings of ASME Turbo Expo 2014*, Düsseldorf, Germany.
- **Zendehbad, M.**, Chokani, N., Abhari, R.S., 2014, "Large Area Measurements of Wind Speed Using a Mobile-Based LiDAR," *Proceedings of EWEA2014*, Barcelona, Spain.

C. Curriculum Vitae

Personal data

- **Name:** Mohsen Zendeabad
- **Birth:** May 1st 1987, Shiraz, Iran

Education

- PhD, Laboratory for Energy Conversion, Institute of Energy Technology, Swiss Federal Institute of Technology (ETH), Zurich, Switzerland. August 2011-December 2016.
- M.Sc., Mechanical Engineering Department, Sharif University of Technology, Tehran, Iran. September 2009-July 2011.
- B.Sc., Mechanical Engineering Department, Sharif University of Technology, Tehran, Iran. September 2005-September 2009.

Professional experience

- Coordinator of Master studies at Laboratory for Energy Conversion, ETH Zurich, 2015-2016.
- Organized 8th PhD Seminar on Wind Energy in Europe, ETH Zurich, 2012.
- Teaching assistance for three courses: Wind Energy, ThermodynamicsIII, Turbocharger practical training (Head assistant for block course ThermodynamicsIII, receives yearly 300 applicants), ETH Zurich, 2011-2016.